ISSN 1451 - 9372 (Print) ISSN 2217 - 7434 (Online) APRIL-JUNE 2026
Vol. 32, Number 2, 87-173

Chemical Industry & Chemical Engineering Quarterly

The AChE Journal for Chemical Engineering, Biochemical Engineering, Chemical Technology, New Materials, Renewable Energy and Chemistry

www.ache.org.rs/ciceq

The activities of the Association of Chemical Engineers of Serbia are supported by:

MINISTRY OF SCIENCE, TECHNOLOGICAL DEVELOPMENT AND INNOVATION OF REPUBLIC OF SERBIA

Faculty of Technology and Metallurgy, University of Belgrade

Faculty of Science, University of Novi Sad

Institute for Technology of Nuclear and Other Mineral Raw Materials, Bekgrade

Faculty of Technology, University of Novi Sad

Institute of Chemistry, Technology and Metallurgy, University of Belgrade

Faculty of Technical Sciences University of Novi Sad

Faculty of Technology, University of Niš, Leskovac

Faculty of Technical Sciences, University of Priština, Kosovska Mitrovica

IMS Institute, Belgrade

DCP HEMIGAL
Leskovac

Elixir Prahovo

Journal of the
Association of Chemical Engineers of
Serbia, Belgrade, Serbia

Chemical Industry & Chemical Engineering Quarterly

Journal of the
Association of Chemical Engineers of
Serbia, Belgrade, Serbia

Chemical Industry & Chemical Engineering Quarterly

Vol. 32 Belgrade, April-June 2026 No. 2

Chemical Industry & Chemical Engineering Quarterly (ISSN 1451-9372) is published quarterly by the Association of Chemical Engineers of Serbia, Kneza Miloša 9/I, 11000 Belgrade, Serbia

Editor:
Vlada B. Veljković
veljkovic@yahoo.com

Editorial Office:
Kneza Miloša 9/I, 11000 Belgrade, Serbia
Phone/Fax: +381 (0)11 3240 018
E-mail: shi@ache.org.rs
www.ache.org.rs

For publisher:
Ivana T. Drvenica

Secretary of the Editorial Office:
Slavica Desnica

Marketing and advertising:
AChE Marketing Office
Kneza Miloša 9/I, 11000 Belgrade, Serbia
Phone/Fax: +381 (0)11 3240 018

Publication of this Journal is supported by the Ministry of Education, Science and Technological Development of the Republic of Serbia

Subscription and advertisements make payable to the account of the Association of Chemical Engineers of Serbia, Belgrade, No. 205-2172-71, Komercijalna banka a.d., Beograd

Technical Editor:
Ana V. Veličković

Journal Manager:
Aleksandar B. Dekanski

Printed by:
Faculty of Technology and Metallurgy, Research and Development Centre of Printing Technology, Karnegijeva 4, P.O. Box 3503, 11120 Belgrade, Serbia

Abstracting/Indexing:
Articles published in this Journal are indexed in *Thompson Reuters* products: *Science Citation Index - Expanded*™ - access *via Web of Science*®, part of *ISI Web of Knowledge*℠

CONTENTS

Chemical Industry & Chemical Engineering Quarterly

Available online at
Association of the Chemical Engineers of Serbia AChE
www.ache.org.rs/CICEQ

Chem. Ind. Chem. Eng. Q. 32 (2) 87–97 (2026) CI&CEQ

MAYRA MARTINELLI COSTA

EDUARDA CAROLINE DUARTE AMATTE COELHO

SILVIA FERNANDA MOYA

RAPHAEL SOEIRO SUPPINO

Laboratory of Catalytic Process Engineering and Biorefineries, Department of Process Engineering, School of Chemical Engineering, Universidade Estadual de Campinas (UNICAMP)

INVESTIGATING THE ACIDITY EFFECT OF NIOBIA AS A CATALYTIC SUPPORT FOR FURFURAL CONVERSION

Highlights

- First work in the literature with Ni/Nb_2O_5 as a catalyst for furfural hydrogenation.
- A niobium-based Ni catalyst is an interesting addition to the Brazilian biorefinery portfolio.
- Advantages in catalyst constitution, as Ni is an accessible and inexpensive metal.
- A catalyst predominantly selective to furfuryl alcohol is viable to downstream operations.
- An alternative production process of difurfuryl ether useful to the food industry.

Abstract

As niobia (Nb_2O_5) is an accessible acid support in Brazil, the objective of this work was to evaluate the effect of acidity in Ni/Nb_2O_5 catalysts for the hydrogenation of furfural in the liquid phase. Catalysts with 5, 10, and 15 wt% Ni content were prepared by wet impregnation, activated under H_2 flow, and tested in furfural hydrogenation at 150 °Cand 5 MPa of H_2. N_2 physisorption results suggest pore blocking on the support as the amount of Ni increased. The larger crystallites identified by XRD for 15% Ni/Nb_2O_5 probably favored pore blocking, and the atomic composition in EDS versus XPS indicates a lower metallic dispersion for this solid. TPR and XPS results suggest all Ni catalysts are primarily constituted of reduced Ni species, while TPD-NH_3 confirms that the acidity of the support was passed on to the catalysts. The 15 wt% Ni solid led to a slight decrease in activity, which can be related to its lower dispersion. Catalysts proved to be promising in terms of selectivity to furfuryl alcohol, which remained between 60 and 80% throughout the reaction. Also, the acid sites-derived difurfuryl ether was produced with all catalysts and can be an interesting addition to the biorefineries portfolio.

Keywords: Hydrogenation, biorefinery, metallic loading, nickel, niobium oxide, difurfuryl ether.

SCIENTIFIC PAPER
UDC 66.094.25:669.295:544:60

INTRODUCTION

Considering that fossil resources currently dominate the global supply of energy, chemicals, and materials, greener and renewable alternatives need to be explored. Among many available options, biomass stands out as a readily available source of both fuels and chemicals [1]. Hence the concept of biorefinery arises, as an industry where a cost-effective conversion of biomass yields bioproducts and bioenergy simultaneously, with the aid of optimization strategies related to waste valorization and sustainability [2-4].

Correspondence: M. Martinelli Costa, Laboratory of Catalytic Process Engineering and Biorefineries, Department of Process Engineering, School of Chemical Engineering, Universidade Estadual de Campinas (UNICAMP);
Email: mayramartinellicosta@gmail.com
Paper received: 19 October, 2024
Paper revised: 30 January, 2025
Paper accepted: 2 June, 2025

https://doi.org/10.2298/CICEQ241019013C

There is much potential in the hemicellulosic fraction of biomass. The five-carbon sugar xylose can be obtained from the acid hydrolysis of xylans (hemicellulose constituent) and be further isomerized and dehydrated to form furfural, an essential building block. This is the standard process for furfural production, as the fossil alternative is not economically viable [3,5,6]. Furfural is widely used as a selective organic solvent and has applications in the transportation, pharmaceutical, and agrochemical industries. This product has more than 80 derivatives, including tetrahydrofurfuryl alcohol, 2-methylfuran, and furan, but about 65% of its production is directed toward obtaining furfuryl alcohol [6-10].

The hydrogenation of the aldehyde group in furfural produces furfuryl alcohol, primarily used to produce furan resins, which promotes chemical, thermal, and mechanical stability, as well as resistance to corrosion and solvent act-

ion. However, the industrial process in the gas phase uses a copper-chromite catalyst, an environmentally hazardous solid. Thus, new alternatives have been tested, especially involving supported metal catalysts [6,10,11]. In addition, recent studies have tested the performance of Ni as an active catalyst for furfural conversion in the presence of H_2. The Ni-based catalysts show promising results in terms of activity, with expressive selectivity for hydrogenation, hydrodeoxygenation, decarbonylation, and ring-opening products [12,13]. Figure S1 presents the most common furfural conversion routes and reunites the most important information about furfural and furfuryl alcohol.

Considering the support nature, factors related to availability, sustainability, physicochemical properties, and innovation have been considered. Niobium pentoxide, also known as niobia (Nb_2O_5), can provide high specific surface area and porosity [14], parameters required for catalysis. Moreover, Nb is widely available in Brazil, responsible for about 88% of global niobium production [15]. Nb-based solids such as niobia, niobic acid ($Nb_2O_5.nH_2O$), and niobium phosphate ($NbOPO_4$) are well-established acid catalysts [16], used primarily in reactions that require Brönsted and Lewis acid sites, such as dehydration [17–19]. The catalytic activity of Nb_2O_5 depends on its degree of hydration and the crystalline phase in which the solid is found since it presents polymorphism. For calcination temperatures between 100 and 500 °C, the simultaneous presence of Brönsted and Lewis acid sites can be observed [20], contributing to the acidity of the solid.

Given the above, this research aims to evaluate the acidity effect of Nb_2O_5 as a catalytic support for furfural hydrogenation in the liquid phase. It is noteworthy that the use of niobia in this reaction system still has not been largely explored in the literature, hence evaluating a low-cost catalyst such as Ni/Nb_2O_5 for possible application in biorefinery processes constitutes the main contribution of this work.

EXPERIMENTAL

Catalyst preparation

Catalysts comprising Ni supported on Nb_2O_5 ($Nb_2O_5.nH_2O$, supplied by the Brazilian Metallurgy and Mining Company, CBMM) were synthesized by wet impregnation, following the method described by Suppino *et al.* [21,22]. Nickel chloride, $NiCl_2$ (Sigma Aldrich, 98% purity), was chosen as the metal precursor. Ni loading was tested as 5, 10, and 15 wt% in an attempt to boost the performance of this non-noble metal and investigate the influence of this parameter.

Niobia was synthesized via calcination of niobic acid with synthetic air (80 mL/min) at 400 °C for 4 hours. The wet impregnation was performed by slowly adding the water-diluted precursor to a suspension containing the support. The suspension was heated to 80 °C, and its pH was adjusted to 7 by the addition of NH_4OH (0.5 mol/L) to be above the point of zero charge of the support (~pH 4), obtained via potentiometric titration and in accordance to Kosmulski [23]. After pH adjustment and filtration, solids were washed with deionized water until chlorine was no longer identified in the $AgNO_3$ test. The reduction was accomplished under 60 mL/min H_2 flow, at 400 °C, for 3 hours. To minimize metal oxidation, catalysts were kept under an Ar atmosphere to form a protective layer of inert gas above the materials' surface [21,22].

Support and catalysts characterization

The solids were characterized by N_2 physisorption using models BET and BJH, to obtain information about their textural properties. The analyses were performed at -196 °C in a Tristar Micromeritics equipment (model ASAP 2010). Samples were previously pretreated under vacuum at 200 °C for 12 hours. In all BET graphs, the coefficient of determination was $R^2 > 0,999$, which indicates an adequate adjustment of the model.

The elemental composition of the solids was semi-quantitatively evaluated by scanning electronic microscopy coupled with spectrometric X-ray analysis (SEM/EDS). The analyses were performed in a LEO Electron microscope (model LEO 440i). For SEM, the conditions applied were an electrical current of 100 pA and 20 kV, with 25 mm focus (magnification 1000x). Meanwhile, EDS was based on elemental mapping, with a 70 eV system resolution, using the ZAF method with 4 to 5 interactions.

The crystalline phases of catalysts were investigated with X-ray diffraction (XRD). The analyses were carried out in a Phillips Analytical X-Ray equipment (model X'Pert-MPD). The applied conditions were: 2θ from 20° to 80°, 0.02° step, 40 kV voltage, 40 mA current, 0.04°/s scanning, and 0.5 s/step. It is possible to estimate the mean crystallite size (s) using the Scherrer Equation. For spherical crystallites, the characteristic constant K is often 0.9 [24].

X-ray photoelectron spectroscopy (XPS) was applied to analyze the surface composition and the oxidation states of the active phase, using a spherical analyzer VSWHA-100 with an aluminum anode (Al Kα, hv = 1486.6 eV). The pressure achieved was lower than 2.10^{-12} MPa. To correct the binding energies, line C 1s with a binding energy of 284.6 eV was considered for reference.

The profile corresponding to the degree of reduction of previously reduced catalysts was studied with temperature-programmed reduction (TPR) in a Micromeritics AutoChem 2910 equipment. In TPR, solids were heated under 60 mL/min flow of a 10% H_2/Ar mixture, with a heating rate of 10 °C/min, from 25 °C to 600 °C. The total time of analysis was around 60 min. The degree of reduction was estimated by a ratio between the values of actual and nominal H_2 consumption, subtracted from 1 (100%).

Temperature-programmed desorption using NH_3 as a basic probe molecule (TPD-NH_3) was also performed in a Micromeritics AutoChem 2910 equipment containing a TCD detector, to study the acidity of the solids. Pretreatment was accomplished with 25 mL/min He flow at 300 °C (10 °C/min). Saturation was conducted under 25 mL/min NH_3 flow (30% NH_3 and 70% He) for 30 minutes at 50 °C. Samples were flushed with He also for 30 minutes at 50 °C to remove the physisorbed NH_3. Finally, samples were heated to 500 °C (10 °C/min) and this temperature was kept for 20 minutes. The total time of analysis was around 65 minutes.

Catalytic tests

All chemical reagents used in catalytic tests were supplied by Sigma Aldrich, with purity higher than 98%. Catalysts were externally reduced under H_2 flow before reactions, as described in the Experimental section.

Catalytic tests were carried out in a slurry Parr reactor of 300 mL capacity initially filled with 300 mg of Ni catalyst, 38.9 g of 2-propanol, chosen as the solvent, and 2.1 g of heptane, used as an internal standard for chromatographic quantification. The reactor was hermetically closed, purged with N_2 three times, and subsequently pressurized to 5 MPa of H_2 with agitation adjusted to 1000 rpm. When a reaction temperature of 150 °Cwas reached, 8.7 g of furfural was added directly to the reactor through an ampoule, to obtain a substrate concentration of 1.5 mol/L.

Reactants and products were quantified in an HP-5890 series II gas chromatograph equipped with a flame ionization detector (FID). A calibration curve was constructed with the internal standard. The injection in triplicate suggests a standard deviation below 5%. An OV-5 capillary column was used, with 5% diphenyl and 95% dimethylpolysiloxane stationary phase. Samples collected at the end of the reaction (5 hours) were also submitted to gas chromatography coupled with mass spectrometry (GC-MS) using a Perkin Elmer equipment (GC: AutoSystem XL and MS: TurboMass). Similar analytical conditions were applied, with an NST-5 capillary column.

The conversion was calculated as moles of furfural reacted divided by moles of furfural at the beginning of the reaction. Selectivity was calculated as the mole percentage of a specific product relative to all identified liquid products.

RESULTS AND DISCUSSION

Characterization results

Table 1 presents the results of metal content, specific surface area, mean pore diameter, and crystalline domain size. There is an agreement between the nominal metal loading of the solids and the results given by the EDS analysis. No signs of residual chlorine were identified. Additionally, the SEM images in Figure S2 show no modifications related to morphology after metallic impregnation.

The isotherms obtained by N_2 physisorption are present in Figure S3. The support and Ni catalysts possess type IV(a) isotherms which correspond to mesoporous solids [25]. The Nb_2O_5 support has a specific surface area of 126 m^2/g, which agrees with previously reported values for Nb_2O_5 calcined at 400 °C [26,27]. The impregnation of Ni on the surface of niobia did not affect the total pore volume; however, there was a slight but gradual decrease in the specific surface area of the catalysts, if compared to the support (up to 30% for 15%/Nb_2O_5). Also, an increase in the mean pore diameter of supported catalysts was noticed with the increase in Ni loading. These findings suggest the occurrence of a partial pore blockage on the support, more significant as the amount of impregnated Ni increased.

Figure 1 contains the XRD diffractograms for the calcined support, as well as for the Ni-reduced catalysts. The XRD results indicate the presence of a predominantly non-crystalline structure for the support. Otherwise, it is observed some crystallinity degree by the Ni metallic phase for the three catalysts. Peaks corresponding to metallic Ni (JCPDS 01-070-1849) were identified, leading to the conclusion that at least some degree of reduction was achieved at 400 °C and pure H_2 gas. As shown in Table 1, the solid containing 15 wt% Ni has the largest mean Ni crystallite size (32 nm). Therefore, the larger crystallites likely favored pore blocking.

As for the TPR results, values of peak temperature and degree of reduction are reported in Table 2, while the H_2 consumption profiles for previously reduced catalysts are present in Figure 2. It is essential to highlight that the TPR was performed to evaluate the efficiency of the reduction method and how much of the metallic phase would remain on the surface after catalysts were exposed to the atmosphere. The profile corresponding to the support is also shown, which is proved irreducible under the conditions applied.

The H_2 consumption peaks identified in TPR at a temperature range of 150-200 °C are probably due to the oxidation of Ni in the form of Ni(II), which is typical for non-noble catalysts exposed to atmospheric conditions [28]. Surface reoxidation in this temperature range has been reported elsewhere [29,30]. Considering this hypothesis, all Ni catalysts present a degree of reduction higher than 95%, which confirms that the reduction was appropriate and effective and that the atmospheric exposure led to significant oxidation for none of the catalysts.

As for the XPS results, Table 3 shows the binding energies of the peaks found in each spectrum and the probable surface composition of the catalysts. To verify that the metallic active phase for hydrogenation is indeed on the surface, there is also a comparison between the Ni/Nb atomic ratios measured through XPS and EDS. Figure 3 presents the XPS spectra for the 5, 10, and 15 wt% Ni catalysts.

Peaks around 852 eV and 855 eV were commonly observed for Ni catalysts. The binding energy of 852 eV corresponds to Ni(0) while the peak in 855 eV can be attributed to Ni(II) [31], which has also been reported for other Ni catalysts reduced by H_2 flow at 400 °C [30]. Therefore, the TPR and XPS results suggest that all three Ni catalysts are primarily constituted of reduced Ni species, with a partially oxidized surface of a few atomic layers depth.

Another possible analysis of the surface properties can be accomplished by comparing the atomic composition using the ratio Ni/Nb, which indicates an enrichment of Ni over the surface when compared with the bulk composition for all catalysts. However, the difference between the ratios is less pronounced for the 15 wt% Ni solid. This solid presented an increase of 78% in its mean crystallite size, compared to 10% Ni/Nb_2O_5, therefore it is expected that the metal dispersion on the surface has been compromised.

Table 4 shows the TPD-NH_3 results, while Figure 4 displays the profiles obtained in the analyses for the support and catalysts. The support presents a total acidy of 676 μmol NH_3/g, primarily including weak and medium-

strength acid sites [32]. This TPD profile is consistent with previous studies with calcined Nb_2O_5, also provided by CBMM [17,33]. The acidity values tend to drop with the increase of calcination temperature, once the crystalline transition causes suppression of acid sites [20]. Therefore, the acidity values found for niobia calcined at 300 °C [33], 400 °C (this work), and 500 °C [17] decrease with calcination temperature, as expected.

Table 1. Ni loading obtained by EDS, textural features obtained by N_2 physisorption, and mean Ni crystallite size obtained by XRD using the Scherrer Equation.

Material	% Ni (w/w)	Specific surface area (m^2/g)	Mean pore diameter (nm)	Ni (111) mean crystallite size (nm)
Nb_2O_5	---	126	5.7	---
5% Ni/Nb_2O_5	5	111	6.7	17
10% Ni/Nb_2O_5	10	104	7.0	18
15% Ni/Nb_2O_5	14	89	7.5	32

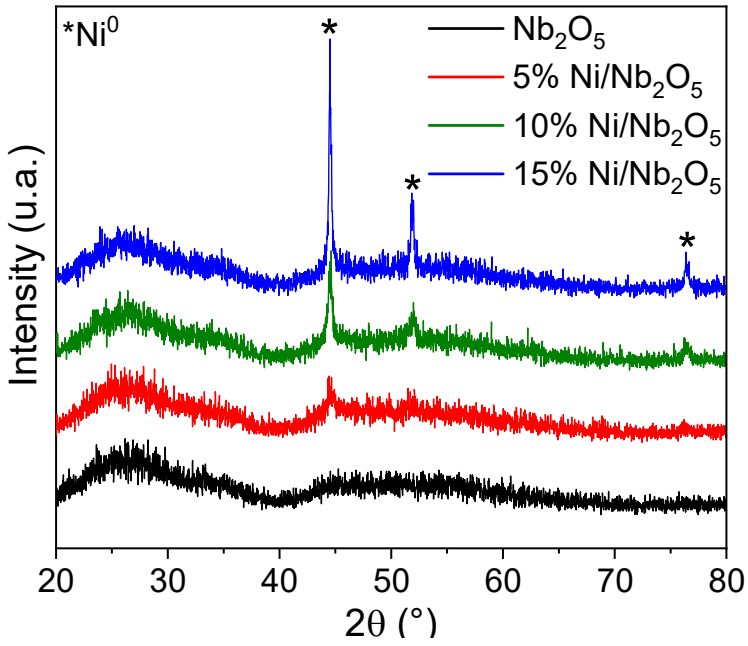

Figure 1. XRD diffractograms for Nb_2O_5 and catalysts containing 5, 10, and 15% Ni/Nb_2O_5.

Table 2. Peak temperature and degree of reduction obtained by TPR.

Material	Peak temperature (°C)	Degree of reduction (%)
Nb_2O_5	---	---
5% Ni/Nb_2O_5	170	95
10% Ni/Nb_2O_5	161	95
15% Ni/Nb_2O_5	157	98

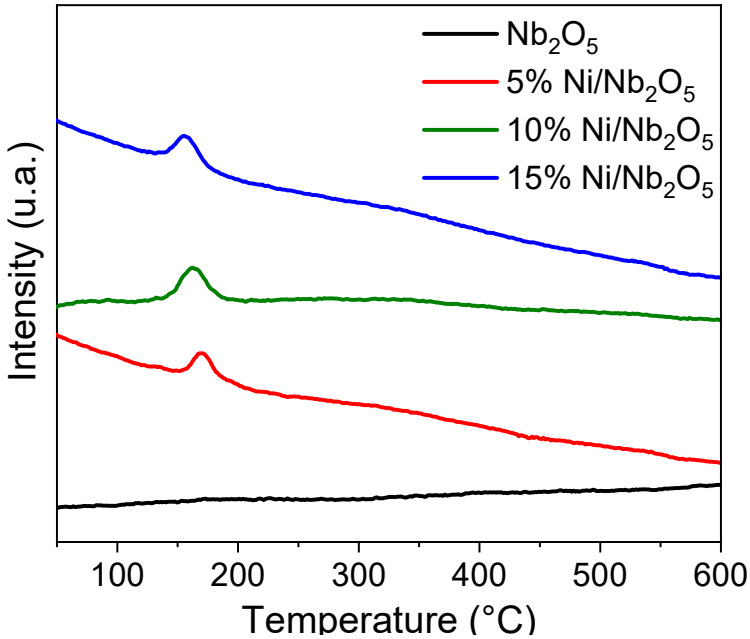

Figure 2. TPR profiles for Nb_2O_5 and previously reduced 5, 10, and 15% Ni/Nb_2O_5 catalysts.

Table 3. Surface composition obtained by XPS and comparison of the Ni/Nb atomic ratio in XPS and EDS.

Material	Binding Energy (eV)	Probable species on the surface	Ni/Nb atomic ratio in XPS	Ni/Nb atomic ratio in EDS
5% Ni/Nb_2O_5	852.2 855.1 860.7	Ni(0) Ni(II) satellite peak	0.23	0.13
10% Ni/Nb_2O_5	852.3 855.3 860.6	Ni(0) Ni(II) satellite peak	0.93	0.31
15% Ni/Nb_2O_5	852.3 855.3 860.7	Ni(0) Ni(II) satellite peak	0.50	0.41

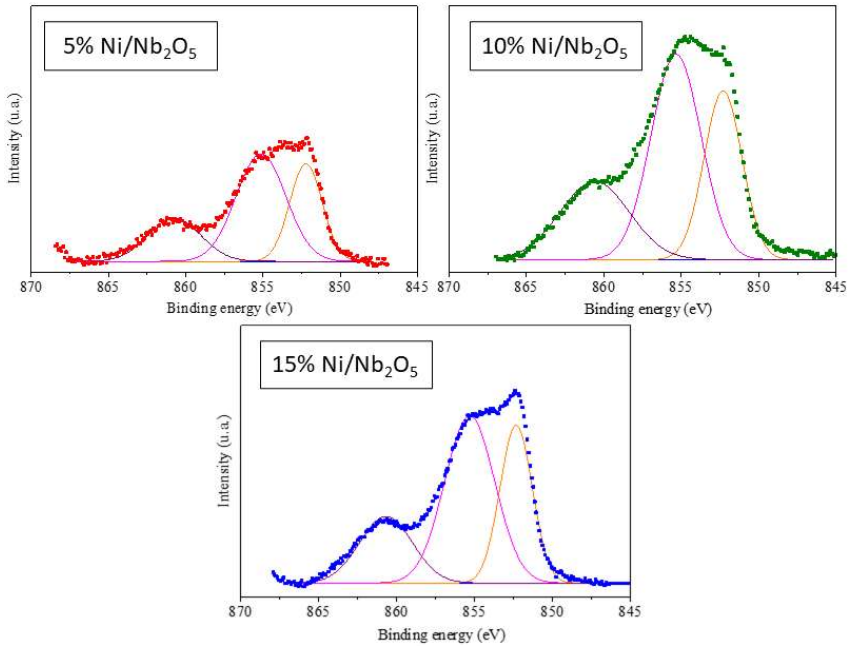

Figure 3. XPS spectra for 5, 10, and 15% Ni/Nb_2O_5.

Table 4. Total acidity and acid site density obtained by TPD-NH_3.

Material	Total acidity ($\mu mol_{NH3}/g$)	Acid sites density ($\mu mol_{NH3}/m^2$)
Nb_2O_5	676	5.4
5% Ni/Nb_2O_5	619	5.6
10% Ni/Nb_2O_5	673	6.5
15% Ni/Nb_2O_5	593	6.7

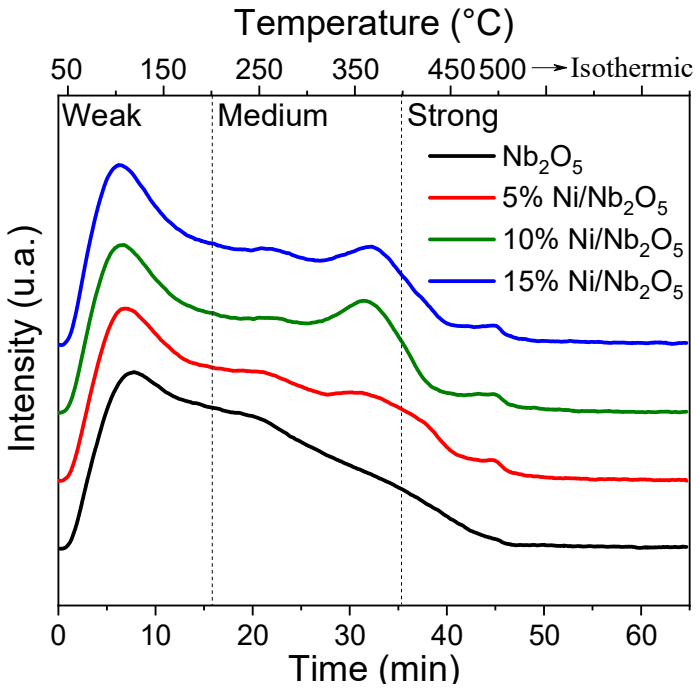

Figure 4. TPD-NH_3 profiles for Nb_2O_5 and catalysts containing 5, 10, and 15% Ni/Nb_2O_5.

In terms of total acidity, there has been little change between the support and the Ni catalysts, with a maximum decrease of 12%. As observed in Table 1, the specific surface area of the catalysts was gradually reduced as the Ni loading increased, resulting in an increase in acid site density with the increment in metal content. A peak near 400 °C, observed for all Ni-supported catalysts, reflects differences in their acidity compared to the support.

According to Guo and Zaera [34], oxygen species originating from partially oxidized surfaces can act as Lewis acid sites for NH_3 adsorption. As discussed earlier in this work, the presence of partially oxidized Ni over the surface was detected for all catalysts.

The TPD-NH_3 results display similarities in acidity for all evaluated materials, which suggests that metallic impregnation, calcination, and reduction thermal treatments did not significantly alter the natural acidity of the support. Therefore, the presence of acidity in the metal-supported catalysts makes them bifunctional, capable of promoting not only hydrogenation to furfuryl alcohol but also other reactions that take place in acid sites [35].

Reaction results

Before discussing the results obtained with Ni as the active phase, it is important to mention that a control reaction was performed using only the calcined support (Nb_2O_5) as a catalyst. After 5h, less than 5% conversion was obtained, with traces of furfuryl alcohol identified. Thus, the support could not hydrogenate furfural on its own, and a metallic active phase is needed in this case. Moreover, the presence of acid sites in niobia might have led to the transformation of furfuryl alcohol to difurfuryl ether, as traces of this last compound were found. This result is an illustration of the acidic characteristic of the support, as it seems to be active for this dehydration reaction.

Another important detail is that, in the reactions of this research, the solvent 2-propanol did not act as an H_2 donor in a Meerwein-Ponndorf-Verley mechanism (MPV), as observed by Li *et al.* [36]. Typical products of 2-propanol decomposition, such as acetone and isopropyl ethers, were not identified in the chromatograms, so the H_2 consumed in the reactions came exclusively from the high-pressure atmosphere created in the reactor.

Figure 5 presents the furfural conversion profile, while Figure 6 presents selectivity to furfuryl alcohol and difurfuryl ether throughout the reactions, with 5, 10, and 15 wt% Ni catalysts. A similar performance was observed with all three solids, with a gradual increase of furfural conversion over time achieving 39, 47, and 41% after 5 h for 5, 10, and

15% Ni/Nb_2O_5, respectively. Despite containing a greater amount of impregnated Ni, which is the active phase responsible for hydrogenation, 15% Ni/Nb_2O_5 presented a slight decrease in catalytic activity. This behavior can be related to a lower metallic dispersion in this catalyst, as suggested by the largest mean crystallite size, 32 nm (XRD result, Table 1), and also by the value encountered for Ni/Nb atomic ratio (XPS result, Table 3), which can lead to a decrease of potential active sites on the surface.

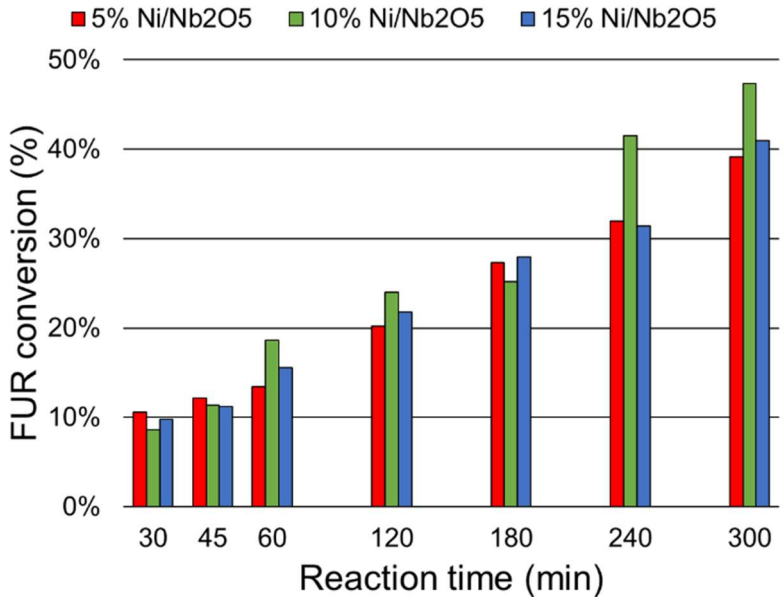

Figure 5. Conversion of furfural measured throughout the reactions catalyzed by 5, 10, and 15% Ni/Nb_2O_5. Reaction conditions: 5 MPa of H_2, 150 °C, agitation speed of 1000 rpm, 300 mg of catalyst.

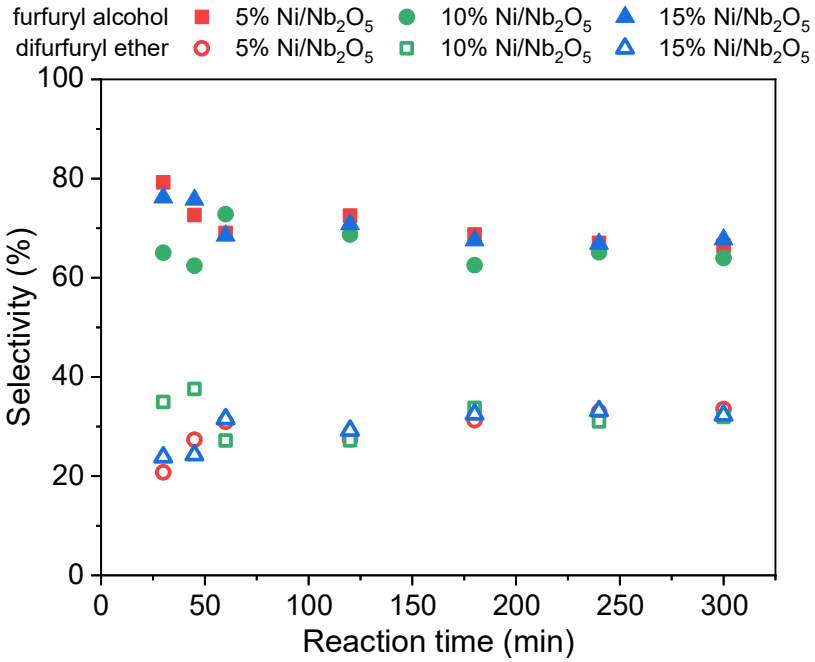

Figure 6. Selectivity to furfuryl alcohol and difurfuryl ether measured throughout the reactions catalyzed by 5, 10, and 15% Ni/Nb_2O_5. Reaction conditions: 5 MPa of H_2, 150 °C, agitation speed of 1000 rpm, 300 mg of catalyst.

Despite the loss in activity with the increase of Ni loading, it is vital to highlight the selectivity tendency that all three solids have presented. Figure 6 shows that the selectivity to furfuryl alcohol remains roughly between 60% and 80% throughout the reaction time for all Ni catalysts. Although these catalysts can be considered bifunctional, as they retained the acidity of the support, the main reaction product was furfuryl alcohol.

The selectivity results are of great interest, as furfural in the presence of H_2 can originate other products, as seen in Figure S1. Table S1 presents Ni catalysts used in furfural hydrogenation to furfuryl alcohol previously reported in the

literature. These catalysts were tested in liquid batch reactions, in experimental conditions similar to this work (synthesis, activation, reaction).

Among all previous applications of Ni in furfural conversion, only 18 were selected according to the criteria previously described, which proves that it is hard to obtain high selectivity to furfuryl alcohol with Ni as the active phase. Even so, Ni/Nb_2O_5 catalysts in this research presents selectivity to furfuryl alcohol comparable to the best results reported in the literature.

Considering this work was exploratory - an introduction of a new catalyst in a selected reaction system – there was no attempt to optimize the catalytic activity. In turn, since the potential of Ni/Nb_2O_5 to produce furfuryl alcohol has been proven, it is now possible to optimize reaction parameters in future research.

The GC-MS analyses were carried out to identify by-products possibly correlated to the nature of the support. The results suggest the presence of difurfuryl ether, with selectivity values of 20–40% throughout the reaction. In the presence of bifunctional catalyst Ni/Nb_2O_5, furfural was firstly hydrogenated to furfuryl alcohol in metallic sites, followed by etherification in acid sites, as also reported elsewhere [37–39]. Difurfuryl ether is widely applied in the food industry as a flavoring agent, and its most common synthesis route is a two-step process of bromination followed by etherification, which is known as environmentally hazardous, so new alternative processes need to be explored [40].

A catalyst recycling test was performed to assess catalyst reusability, and a new set of reactions was carried out with the 10 wt% Ni catalyst, in the same conditions. This catalyst was chosen for the reusability tests due to the higher results in converting furfural on the fresh test (47%). On its second use, a conversion of 42% was obtained, practically repeating the performance of the fresh catalyst. However, in the third cycle, the activity dropped considerably (17%). It is noteworthy that the catalyst was not submitted to any sort of treatment before its reuse, which could restore most of its activity. A more future study, regarding the deactivation mechanism and potential regeneration is required to fully assess these results. Nevertheless, the catalyst was able to maintain the same selectivity profile in all three reactions, with nearly no loss in the production of furfuryl alcohol and difurfuryl ether. The results can be found in Figure S4 (conversion) and Figure S5 (selectivity).

To investigate whether selectivity would be maintained for a long time, catalyst 10% Ni/Nb_2O_5 was tested in a 10-hour reaction. Apparently, this is a system with steady selectivity, regardless of the time frame or catalytic cycle. It is worth mentioning that the conversion profile resembles a second-degree polynomial and tends to stabilize around ten hours, at approximately 55% furfural conversion. Nevertheless, doubling the reaction time has only increased furfural conversion in ca. 5%, which could not be a feasible aspect considering a future industrial application of this catalyst. Modifications in catalytic synthesis or reaction conditions should be performed to achieve higher conversions and this is a topic for future research. The results are presented in Figure S6 (conversion) and Figure S7 (selectivity).

In summary, the Ni/Nb_2O_5 studied in this work was found to be predominantly selective to furfuryl alcohol, currently the most important furfural derivative. As selectivity is a crucial parameter to the viability of a production process, especially in terms of downstream operations, this reaction system has the potential to be integrated into biorefineries. There are also many advantages in terms of catalyst constitution, as a simple synthesis and activation procedure is proposed, and Ni is an accessible and inexpensive metal. Also, the use of niobia as catalytic support for furfural hydrogenation is still incipient, and this work is the first report with Ni-supported catalysts in this reaction. As niobium is a strategic asset for Brazil, a niobium-based Ni catalyst could be an interesting addition to the Brazilian biorefinery portfolio. Furthermore, the findings of this work provide an alternative production process of difurfuryl ether that can also benefit the food industry.

CONCLUSION

The present work was conceived from the question: what would be the influence of niobia as support in Ni catalysts for the hydrogenation of furfural? From there, a series of developments emerged. However, it is believed that the central question has been answered: Ni/Nb_2O_5 catalysts are capable of hydrogenating furfural to furfuryl alcohol, with the direct influence of metallic loading, whereas the acidity of the support also plays a crucial role in the reaction, as difurfuryl ether was found in the reaction medium.

The results obtained can be considered promising. In the reaction conditions applied in this work, catalysts were able to maintain a high and steady selectivity to furfuryl alcohol for at least ten hours. However, the increase of Ni loading from 10 to 15 wt% did not lead to a higher catalyst activity, probably due to an impaired dispersion of Ni on the surface. All in all, a steady selectivity is ideal for industrial processes, and due to its high availability in Brazil, expanding the knowledge about niobium applications can lead to significant economic and technological advances for our country.

ACKNOWLEDGMENTS

The authors would like to thank the “Brazilian Metallurgy and Mining Company” (CBMM) for the supply of niobic acid ($Nb_2O_5.nH_2O$). The authors also thank the “National Council for Scientific and Technological Development” (CNPq) for the financial support: Universal Call MCTIC/CNPq 28/2018 process no. 431272/2018-2, and research scholarships were granted to Ms. Costa (130783/2019-6) and Ms. Coelho (116878/2019-3). This study was financed in part by “Coordenação de Aperfeiçoamento de Pessoal de Nível Superior - Brasil” (CAPES) - Finance Code 001. Also, the present work was conducted within the scope of grant #2015/20630-4, São Paulo Research Foundation (FAPESP).

REFERENCES

[1] I. Ahmed, M.A. Zia, H. Afzal, S. Ahmed, M. Ahmad, Z. Akram, F. Sher, H.M.N. Iqbal, Sustainability (Switzerland) 13 (2021) 1-32. https://doi.org/10.3390/su13084200.

[2] S.S. Hassan, G.A. Williams, A.K. Jaiswal, Renewable Sustainable Energy Rev. 101 (2019) 590-599. https://doi.org/10.1016/j.rser.2018.11.041.

[3] B. Kumar, P. Verma, Fuel 288 (2021) 119622. https://doi.org/10.1016/j.fuel.2020.119622.

[4] E. Scopel, C.A. Rezende, Ind. Crops. Prod. 163 (2021) 113336. https://doi.org/10.1016/j.indcrop.2021.113336.

[5] C.B.T.L. Lee, T.Y. Wu, Renewable Sustainable Energy Rev. 137 (2021) 110172. https://doi.org/10.1016/j.rser.2020.110172.

[6] R. Mariscal, P. Maireles-Torres, M. Ojeda, I. Sádaba, M. López Granados, Energy Environ. Sci. 9 (2016) 1144-1189. https://doi.org/10.1039/C5EE02666K.

[7] M. Ghashghaee, S. Shirvani, V. Farzaneh, S. Sadjadi, Braz. J. Chem. Eng. 35 (2018) 669-678. https://doi.org/10.1590/0104-6632.20180352s20160703.

[8] J.F.L. Silva, M.A. Selicani, T.L. Junqueira, B.C. Klein, S. Vaz Júnior, A. Bonomi, Braz. J. Chem. Eng. 34 (2017) 623-634. https://doi.org/10.1590/0104-6632.20170343s20150643.

[9] M.L. Testa, M.L. Tummino, Catalysts 11 (2021) 1-27. https://doi.org/10.3390/catal11010125.

[10] K. Yan, G. Wu, T. Lafleur, C. Jarvis, Renewable Sustainable Energy Rev. 38 (2014) 663-676. https://doi.org/10.1016/J.RSER.2014.07.003.

[11] P. Khemthong, C. Yimsukanan, T. Narkkun, A. Srifa, T. Witoon, S. Pongchaiphol, S. Kiatphuengporn, K. Faungnawakij, Biomass Bioenergy 148 (2021) 106033. https://doi.org/10.1016/j.biombioe.2021.106033.

[12] H. Tian, G. Gao, Q. Xu, Z. Gao, S. Zhang, G. Hu, L. Xu, X. Hu, Mol. Catal. 510 (2021) 111697. https://doi.org/10.1016/j.mcat.2021.111697.

[13] Z. Zhang, K. Sun, Y. Ma, Q. Liu, Q. Li, S. Zhang, Y. Wang, Q. Liu, D. Dong, X. Hu, Catal. Sci. Technol. 9 (2019) 4510-4514. https://doi.org/10.1039/c9cy00985j.

[14] A. Florentino, P. Cartraud, P. Magnoux, M. Guisnet, Appl. Catal., A 89 (1992) 143-153. https://doi.org/10.1016/0926-860X(92)80229-6.

[15] U.S. Geological Survey, Mineral Commodity Summaries, Virginia (2019). https://doi.org/10.3133/70202434.

[16] S. Kang, R. Miao, J. Guo, J. Fu, Catal. Today 374 (2021) 61-76. https://doi.org/10.1016/j.cattod.2020.10.029.

[17] L.F. de Lima, J.L.M. Lima, D.S.S. Jorqueira, R. Landers, S.F. Moya, R.S. Suppino, React. Kinet., Mech. Catal. 132 (2021) 73-92. https://doi.org/10.1007/s11144-021-01931-y.

[18] K. Skrodczky, M.M. Antunes, X. Han, S. Santangelo, G. Scholz, A.A. Valente, N. Pinna, P.A. Russo, Commun. Chem. 2 (2019) 1-11. https://doi.org/10.1038/s42004-019-0231-3.

[19] J.L. Vieira, G. Paul, G.D. Iga, N.M. Cabral, J.M.C. Bueno, C. Bisio, J.M.R. Gallo, Appl. Catal., A 617 (2021) 118099. https://doi.org/10.1016/j.apcata.2021.118099.

[20] T. Iizuka, K. Ogasawara, K. Tanabe, Bull. Chem. Soc. Jpn. 56 (1983) 2927-2931. https://doi.org/10.1246/bcsj.56.2927.

[21] R.S. Suppino, R. Landers, A.J.G. Cobo, Appl. Catal., A 452 (2013) 9-16. https://doi.org/10.1016/j.apcata.2012.11.034.

[22] R.S. Suppino, R. Landers, A.J.G. Cobo, Appl. Catal., A 525 (2016) 41-49. https://doi.org/10.1016/j.apcata.2016.06.038.

[23] M. Kosmulski, Adv. Colloid Interface Sci. 238 (2016) 1-61. https://doi.org/10.1016/j.cis.2016.10.005.

[24] G. Ertl, H. Knözinger, F. Schüth, Handbook of heterogeneous catalysis, Wiley-VCH, Weinheim (2008).

[25] M. Thommes, K. Kaneko, A.V. Neimark, J.P. Olivier, F. Rodriguez-Reinoso, J. Rouquerol, K.S.W. Sing, Pure Appl. Chem. 87 (2015) 1051-1069. https://doi.org/10.1515/pac-2014-1117.

[26] R. Brayner, F. Bozon-Verduraz, Phys. Chem. Chem. Phys. 5 (2003) 1457-1466. https://doi.org/10.1039/b210055j.

[27] K.M.A. Santos, E.M. Albuquerque, L.E.P. Borges, M.A. Fraga, Mol. Catal. 458 (2018) 198-205. https://doi.org/10.1016/j.mcat.2017.12.010

[28] F. Huber, Z. Yu, S. Lögdberg, M. Rønning, D. Chen, H. Venvik, A. Holmen, Catal. Lett. 110 (2006) 211-220. https://doi.org/10.1007/s10562-006-0111-1.

[29] R.S. Suppino, R. Landers, A.J.G. Cobo, React. Kinet. Mech. Catal. 114 (2015) 295-309. https://doi.org/10.1007/s11144-014-0790-3.

[30] S. Jantarang, E.C. Lovell, T.H. Tan, J. Scott, R. Amal, Prog. Nat. Sci.: Mater. Int. 28 (2018) 168-177. https://doi.org/10.1016/j.pnsc.2018.02.004.

[31] National Institute of Standards and Technology, NIST X-ray Photoelectron Spectroscopy Database, NIST Standard Reference Database Number 20 (2012). https://doi.org/10.18434/T4T88K

[32] P. Berteau, B. Delmon, Catal. Today 5 (1989) 121-137. https://doi.org/10.1016/0920-5861(89)80020-3.

[33] V.M. Benitez, S.P. de Lima, M. do Carmo Rangel, D. Ruiz, P. Reyes, C.L. Pieck, Catal. Today 289 (2017) 53-61. https://doi.org/10.1016/j.cattod.2016.10.004.

[34] H. Guo, F. Zaera, Surf. Sci. 524 (2003) 1-14. https://doi.org/10.1016/S0039-6028(02)02486-X.

[35] A.M. Robinson, J.E. Hensley, J.W. Medlin, ACS Catal. 6 (2016) 5026-5043. https://doi.org/10.1021/acscatal.6b00923.

[36] F. Li, W. Zhu, S. Jiang, Y. Wang, H. Song, C. Li, Int. J. Hydrogen Energy 45 (2019) 1981-1990. https://doi.org/10.1016/j.ijhydene.2019.11.139.

[37] A. Aldureid, F. Medina, G.S. Patience, D. Montané, Catalysts 12 (2022) 390. https://doi.org/10.3390/catal12040390.

[38] M.A. Jackson, M.G. White, R.T. Haasch, S.C. Peterson, J.A. Blackburn, Mol. Catal. 445 (2018) 124-132. https://doi.org/10.1016/j.mcat.2017.11.023.
[39] Á. O'Driscoll, J.J. Leahy, T. Curtin, Catal. Today 279 (2017) 194-201. https://doi.org/10.1016/j.cattod.2016.06.013.
[40] S. Yang, Y. Hao, J. Wang, H. Wang, Y. Zheng, H. Tian, Sci. Rep. 7 (2017) 12954. https://doi.org/10.1038/s41598-017-13472-3.

MAYRA MARTINELLI COSTA

EDUARDA CAROLINE DUARTE AMATTE COELHO

SILVIA FERNANDA MOYA

RAPHAEL SOEIRO SUPPINO

Laboratory of Catalytic Process Engineering and Biorefineries, Department of Process Engineering, School of Chemical Engineering, Universidade Estadual de Campinas (UNICAMP)

NAUČNI RAD

ISTRAŽIVANJE EFEKTA KISELOSTI NIOBIJUM-PENTAOKSIDA KAO NOSAČA KATALITIZATORA KONVERZIJU FURFURALA

Pošto je niobijum-pentaoksid (Nb_2O_5) pristupačan kiseli nosač u Brazilu, cilj ovog rada je bio da se proceni efekat kiselosti Ni/Nb_2O_5 katalizatora za hidrogenaciju furfurala u tečnoj fazi. Katalizatori sa 5, 10 i 15% Ni su pripremljeni vlažnom impregnacijom, aktivirani u struji H_2 i testirani u hidrogenaciji furfurala na 150 °C i 5 MPa H_2. Rezultati fizisorpcije N_2 ukazuju na blokiranje pora na nosaču sa povećanjem količine Ni. Veći kristaliti identifikovani XRD-om za 15% Ni/Nb_2O_5 verovatno su favorizovali blokiranje pora, a atomski sastav određen EDS-om u odnosu na sastav određen XPS-om ukazuje na manju disperziju metala za ovu čvrstu supstancu. Rezultati TPR i XPS ukazuju na to da su svi Ni katalizatori prvenstveno sastavljeni od redukovanih Ni vrsta, dok TPD-NH_3 potvrđuje da je kiselost nosača preneta na katalizatore. Čvrsta supstanca Ni sa 15% dovela je do blagog smanjenja aktivnosti, što se može povezati sa njenom manjom disperzijom. Katalizatori su se pokazali obećavajućim u selektivnosti prema furfuril-alkoholu, koji je ostao između 60 i 80% tokom cele reakcije. Takođe, difurfuril-etar dobijen iz kiselih mesta je proizveden sa svim katalizatorima i može biti zanimljiv dodatak portfoliju biorafinerija.

Ključne reči: Hidrogenacija, biorafinerija, metalno punjenje, nikl, niobijum oksid, difurfuril etar.

CI&CEQ
Chemical Industry & Chemical Engineering Quarterly

Available online at
Association of the Chemical Engineers of Serbia AChE
www.ache.org.rs/CICEQ

Chem. Ind. Chem. Eng. Q. 32 (2) 99–109 (2026) CI&CEQ

RAJASEKAR CHOCKLINGAM[1]

RAMESHKUMAR RAMASAMY[2]

BARATHIRAJA RAJENDRAN[3]

[1]Department of Mechatronics Engineering, Akshaya College of Engineering and Technology, Tamil Nadu, India

[2]Department of Mechanical Engineering, Builders Engineering College,Tamil Nadu, India

[3]Department of Mechanical Engineering, Mahakavi Bharathiyar College of Engineering & Technology, Tamil Nadu, India

SCIENTIFIC PAPER

UDC 536.24:665.36:621.3

THE IMPACT OF HEAT STORAGE MATERIAL INTEGRATION IN AN EVACUATED TUBE COLLECTOR

Highlights

- The ETC system with heat storage materials outperformed the system without TESM.
- The ETC system with engine oil had the highest outlet temperature.
- Rice bran wax demonstrated higher thermal efficiency compared to other heat storage materials.

Abstract

This experimental research assessed the impacts of sensible and latent heat materials such as SAE 20W/40 (used engine oil, UEO), candelilla wax (CLW), and rice bran wax (RBW) in an ETSAH (Evacuated Tube Solar Air Heater). Four distinct arrangements were studied: one without a thermal energy storage material (TESM), one with a sensible heat material (SHM), and two with latent heat materials (LHM), to enable comparative analysis. The maximum outlet temperature of air for ETC filled with UEO was 108 °C, for CLW 115 °C, and RBW 133 °C - all measured at 13:00. However, without filling the TESM in the ETC, the outlet temperature was only 70 °C. The maximum temperature difference of the air in the RBW material-filled ETSAH system was 94 °C, whereas, without TESM, the temperature was only 31 °C at 13:00. The maximum efficiency of the ETSAH system was achieved when using RBW as a PCM rather than both CLW and UEO-filled TESM. Moreover, the efficiency of the system increases around 1.7-1.8 times when the velocity of air increases from 1.5 to 2.5 m/s.

Keywords: Evacuated tube collector; latent heat; sensible heat; thermal storage material; rice bran wax; candelilla wax.

INTRODUCTION

The demand for traditional energy resources is now incredibly high, as non-renewable energy sources are continually exhausted every day. The development of technology like renewable energy sources is essential in the future to keep global energy supplies steady. Non-conventional energy sources, such as solar, play a pivotal role in energy production, as non-renewable energy sources are constantly declining. Solar energy is an optimistic and plentiful option. In many applications, solar energy is both environmentally sustainable and energy-saving. Solar energy can be used very effectively to generate hot air to substitute electric heaters for industrial and space heating applications, electricity generation, refrigeration and air conditioning, and drying of food products [1-4].

Solar heat energy, owing to its clean nature and abundant availability, has been preferred over other promising renewable energy sources [5-7]. Solar energy is an intermittent resource of energy. However, it mainly depends on environmental conditions and is also a time-dependent supply source. The simplest and most commonly accepted approach is to convert solar energy into a potential heat resource [8-10].

In any method for harvesting solar heat energy, the solar collector is a primary device of such a system. The solar power is collected by the solar collector and is converted into heat, and the heat energy is transferred into the heat-gaining fluid, like air or water that commonly flows through the system. Indeed, solar heating is an ancient technique; nevertheless, progressive technologies have emerged consistently to enhance solar absorption and output temperature. According to Tyagi *et al.* [11],

Correspondence: R. Chockalingam, Department of Mechatronics Engineering, Akshaya College of Engineering and Technology, Tamil Nadu, India.
Email: rajasekarmech006@gmail.com
Paper received: 24 October, 2024
Paper revised: 22 May, 2025
Paper accepted: 5 June, 2025

https://doi.org/10.2298/CICEQ241024014R

thermal energy systems are a key element in the energy harvesting approaches as well as pronounced techniques, especially in solar energy-storing systems.

Heat energy coming from the sun is collected by various types of solar collectors, like flat plate collectors (FPC), evacuated tube collectors (ETC), and concentrating detectors, with FPC often used for low-temperature needs. Moreover, the ETC works at higher fluid outlet temperatures, which is required; however, it has a high cost and a longer payback period compared to FPC [12]. Evacuated tubes have had heated water for years, but not air in commercial settings. Across the globe, people utilize one-ended glass evacuated tubes for their enhanced efficiency. ETC, rather than FPC, achieved the high temperature of the outlet air under the same atmospheric conditions [13,14].

In general, the potential heat source can be reserved in the form of sensible heat, latent heat, or chemical energy [9,15]. Latent heat storage (LHS) systems using phase-change materials (PCMs) are preferred methods because they can store more energy and keep heat at stable temperatures during the melting process [16–18]. Phase change materials can be classified as organic, artificial, and eutectic. Organic PCMs include paraffin waxes and fatty acids that are biologically stable, do not corrode, and work at high temperatures. However, their heat conduction properties are not good, and they can catch fire easily. Inorganic PCMs, such as salt hydrates and some metals, have the capability of holding more latent heat and transferring heat more efficiently than biological PCMs. But these PCMs have problems like supercooling, phase separation, and corrosion, though, and usually need stabilizers or sealing methods to fix. Eutectic PCMs are mixes that melt and harden at a single, clear temperature. Organic and inorganic materials, or organic and inorganic materials, can be mixed as per the requirement. This gives the freezing point that is required. Eutectics are good because they have a sharp phase change temperature and can be designed in a lot of different ways, but they can be more expensive and may not be stable over long periods of thermal cycles. Different types of PCM are picked based on the application's temperature needs and limitations [24,25]. Low thermal conductivity is a problem that PCMs often have. Several enhancement methods are used to get around this problem. Additives with high conductivity are often used. These can be metal nanoparticles (like Al, Cu, and Ag) or carbon-based materials such as graphene, carbon nanotubes, and expanded graphite. These additives make electrical paths inside the PCM, which speeds up the flow of heat. Adding metal foams or structures with fins to the PCM is another way to make it easier for heat to move through. The methods of microencapsulation and nanoencapsulation also help to improve thermal conductivity while keeping the structure stable. Moreover, form-stable hybrid PCMs are created by adding PCMs to porous, heat-conducting materials like metal oxides or graphite. These methods not only improve the flow of heat but also make PCMs more reliable and stable over time in real-world situations. In addition to changes in composition, adding thermally conductive materials and changing the geometry or shape of the inserts are very important for making PCMs better at conducting heat. To improve the effective heat transfer area and speed up thermal response, metallic inserts made of copper, aluminum, or stainless steel are often built into the PCM. These inserts can be in the form of pins, rods, fins, wires, or mesh structures [26–30].

If the SAH system integrated with PCM is used enormous heat can be stored rather than sensible heat storage (SHS) system. Advanced PCMs are applied extensively in LHS systems and solid-liquid PCM materials for storing thermal energy resources approximately 5 to 14 folds more than SHS systems [19–22]. So, it is a desirable choice if the supply and demand of heat energy resources are inconsistent and is ideal for solar air heating systems due to excellent thermal efficiency behavior [11,21].

Tyagi *et al.* [11] experimentally analyzed the ETC-type solar air heater (SAH) integrated with and without SHM and PCM. The efficiencies of heat storage medium are substantially higher in comparison to that without energy storage materials and also the efficiencies of PCM are remarkably greater than that of SHM and without arrangements. Similarly, an ETC-type SAH was experimentally investigated by Kumar *et al.* [10], who analyzed the system performance by varying the inlet air flow rates as well as with and without the assistance of reflectors. The results indicated that the highest outlet temperature and peak differential air temperature of 97.4 °C and 74.4 °C were obtained at an airflow of 6.70 kg/h. Khadraoui *et al.* [6] examined the SAH integrated with and without PCM. It is reported that the efficiency of the SAH integrated with PCM achieved 33% whereas without energy storage arrangement reached only 17%. Similarly, Jain *et al.* [23] claim that the LHS material performs better than SHS materials in which the myristic acid was utilized as PCM.

According to the comprehensive literature review, many studies have been conducted on SAHs integrated with both sensible and LHS materials. However, no experimental study has yet investigated an evacuated tube SAH (ETSAH) integrated with thermal energy storage materials (TESMs) such as candelilla wax (CLW), rice bran wax (RBW), and used engine oil (UEO) of SAE 20W/40. Keeping this gap in mind, the present investigation aims to examine the thermal performance—specifically the outlet temperature, temperature difference of the working fluid, and system efficiency during both sunshine and post-sunset periods under Indian climatic conditions. Additionally, the study evaluates the effect of varying air flow rates in an SAH integrated with a thermal energy storage unit compared to a system without TESMs. Furthermore, the use of thermally active organic materials like waxes and UEO in the evacuated tube, along with the thermal interaction between the heat transfer fluid and the storage medium, inherently contributes to enhancing the effective thermal conductivity (k) of the system, thereby improving the overall heat transfer performance.

MATERIAL AND METHODS

MATERIALS

Four experimental studies have been carried out: one without any TESMs, one with sensible heat storage material (SHSM), and two with LHS materials (LHSMs). An ETC acts as an SAH in these experiments, and a total of four frames have been designed, with each frame having five tubes. The copper pipe, 10 mm in diameter, is placed inside the evacuated tube through a U-bend to move air freely inside the tube. One inlet manifold, which was made of PVC and has a diameter of 150 mm, was used to supply the working fluid into all setups with the help of one blower. The inlet manifold and inlet of the copper tube of each setup were connected by four different lengths of plastic hoses (1000 mm, 1500 mm, 2000 mm, and 2500 mm). The description of the ETC details and SHSM are illustrated in Table 1.

Table 1 Details about the SAH Collector and SHSMs

Specification of Collector Tubes	Values
Total length	1800 mm
Inner length	1760 mm
Coating length	1720 mm
Inner diameter	44 mm
Outer diameter	58 mm
Properties of UEO (SAE 20W- 40)	
Kinematic viscosity @ 100 °C, cst	12.5-14.5
Flash point coc, °C, min	198
Pour point C, max	-19
Viscosity index	102
Copper strip corrosion 3 h @ 100 _C (ASTM), max	1.0
Neutralization number mg koh/g, max	5.8
250 °C	5.6
280 °C	5.4
300 °C	5.2

The ETC frame does not contain any heat storage materials. The second arrangement of the ETC frame contains 11 liters (2.2 liters each) of UEO (SAE-20W/40), and it acts as a SHSM. The third and fourth setups are filled with bio-phase change materials (PCMs), including 10 kg of RBW and 10 kg of CLW, which are LHSMs.

EXPERIMENT SET-UP

For four arrangements and three different flow rates experiments were carried out on ETC with and without TESM. A total of 20 ETC tubes were used in this analysis, of which 5 were filled with RBW, 5 with CLW, 5 with UEO and another 5 empty tubes, all placed in series. Fig. 1 (a, b & c) shows the full illustration of a dual-wall type evacuated tube made of glass, inside which the TES is kept.

One frame contains five tubes of ETC, which are used to absorb the radiated heat from the sun. The absorption takes place as heat absorption coating is applied on the surface of the tube. The frame is set at an angle of 400 from the ground to absorb sun radiation. In this process, two types of PCMs are used to absorb the thermal energy as explained above, and their properties are listed in Table 2.

Table 2 Details about LHSMs

Properties of RBX wax	Values
Melting point	76.05 °C
Specific heat	2.11 kJ/kg °C
Latent heat of fusion	190.6 kJ/kg
Thermal conductivity	0.219 (solid) (W/m K)
Density at 70 °C	0.821 kg/m^3
Properties of CLX wax	
Melting point	66.6 ^{0}C
Specific heat	1.98 kJ/kg °C
Latent heat of fusion	129.7 kJ/kg
Thermal conductivity	0.198 (solid) (W/m K)
Density at 70 °C	0.784 kg/m^3

In this setup, the heated air temperature was measured by 17 thermocouples (RTD PT100): one was placed in the inlet of the system, to measure the inlet air temperature, four were placed in the exit condition and 12 were placed inside the 3-collector tubes (TESM) for each frame (1, 3 and 5). The copper tubes were connected in series, i.e., the outlet of the first tube was connected with the inlet of the second tube, and the rest of the tubes were connected similarly. The hot wire anemometer, used to measure the velocity of the air, was placed between the inlet of the manifold, ETC frames. The pressurized air was circulated into the system by using an air blower while solar intensity was measured every half an hour using a solar power meter.

MEASURING DEVICES AND INSTRUMENTS

An RTD PT100 temperature sensor, together with a digital temperature indicator, was employed to precisely measure the temperature range, which varies from 0 °C to 200 °C with an accuracy of ± 0.5 °C and a resolution of 0.10 °C. The fluid velocity was monitored using a digital hot wire anemometer (Lutron AM-4204), whose measuring accuracy (±5% + 1 d) and resolution are ± 0.1 m/s. The solar power during daylight hours was measured using a solar power meter (Model – CEM DT 1307), and the device offered an accuracy of ±10 W/m² and a resolution of 1 W/m². The phase change material properties were determined by Differential Scanning Calorimeter-DSC 6000 (PerkinElmer). DSC test results for the PCM in conditions between 0 °C and 100 °C for the heating interval and 5 °C/min for the heating rate were given in Fig. 2. Thermal conductivity and specific heat of latent heat materials were determined by the Thermal Properties

Analyser (Model-KD2 Pro), with a range from 0.02 to 2.00 W/m·K, and accuracy is ±5% from 0.2 to 2 W/m.K ± 0.01 W/m·K from 0.02 to 0.2 W/m·K.

EXPERIMENTAL PROCEDURE

In this system, the Sensible and Bio-PCMs were placed inside the ETC device without adding any TESM, and the ETC was heated by radiation from solar energy. Heat storage materials were used to prevent fluctuations in outlet air temperature due to atmospheric variations. The TESM absorbed and stored the heat energy, transferring some of it to the heat-carrying fluid. The stored energy of sensible and latent heat was utilized when the sunshine was low or at night. To confirm the repeatability of the analysis, three studies were conducted for every test on different days of the same month. A centrifugal blower sucked atmospheric air, an anemometer measured it, and a gate valve was used for controlling it. The specified forced air acted as a heat-carrying fluid, and it passed through the hollow copper tube in the ETSAH of all four arrangements at the same time. The temperature of the inlet air was measured before it entered the first tube, as mentioned in the experimental setup procedure. The three different airflow velocities of 1.5, 2.0, and 2.5 m/s were carried out, and their impacts were analyzed. The experimental data was collected from the system over a few days in April 2024 by varying the air velocity. The temperature deviations of the working fluid and the efficiency of ETSAH with and without TESM were evaluated during the period.

UNCERTAINTY ANALYSIS

Errors in the investigations would arise from measuring instruments, weather conditions specified space conditions, inspection, and records due to uncertainties. In the present experimental investigations, the uncertainties involved in the measurement of temperature, velocity of air, and solar intensity were measured through the appropriate instruments; they are listed in Table 2. The computed value M is a function of several independent parameters x_1, x_2, x_3 ...x_n:

The total uncertainty in the assessment of M is computed from the method suggested by Senthil [8]:

$$\delta M = \left[\left(\frac{\partial M}{\partial x_1} \delta x_1 \right) + \left(\frac{\partial M}{\partial x_2} \delta x_2 \right)^2 \cdots\cdots\cdots \left(\frac{\partial M}{\partial x_n} \delta x_n \right)^2 \right]^{\frac{1}{2}} \quad (1)$$

Let δM be the uncertainty in the result of δx_1, δx_2, δx_3... δx_n. The uncertainties in the estimation of the estimation of the overall ETSAH system were 2.8% to 5.2%.

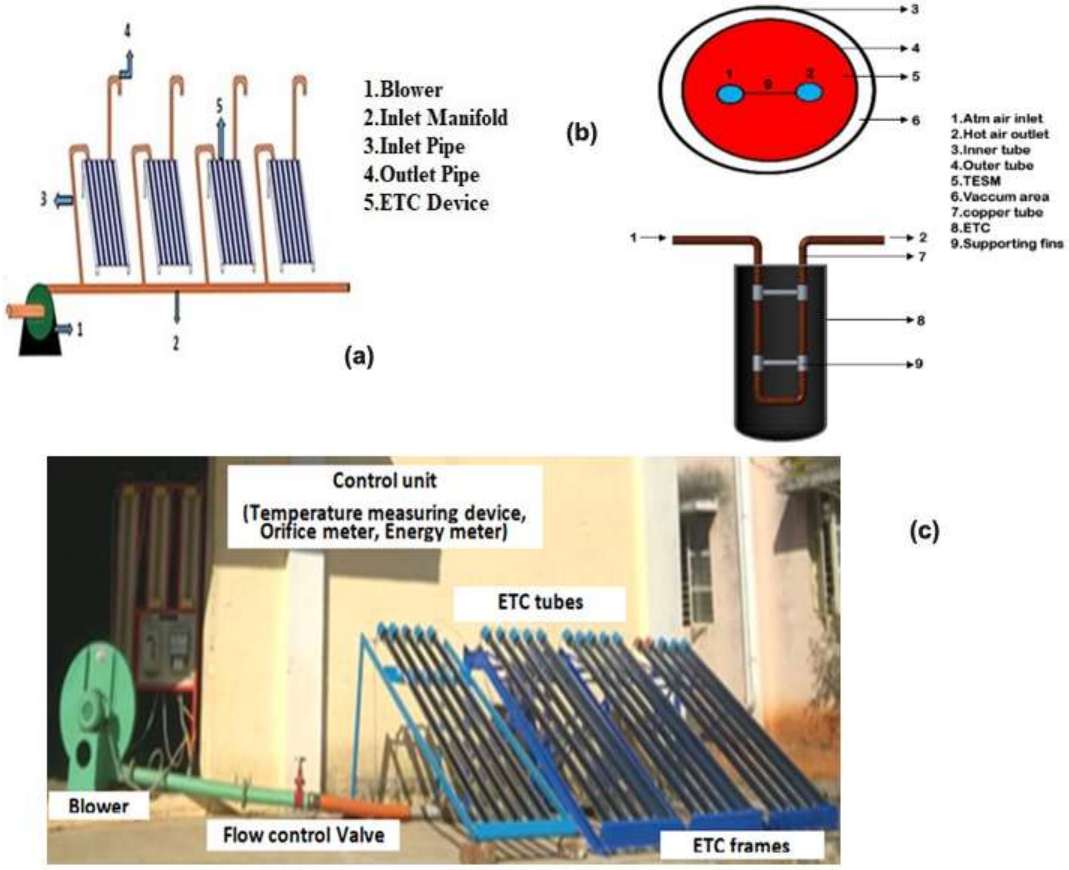

Figure 1 Experimental setup: (a) schematic diagram (b) front view and top view of the ETC, and (c) photographic view.

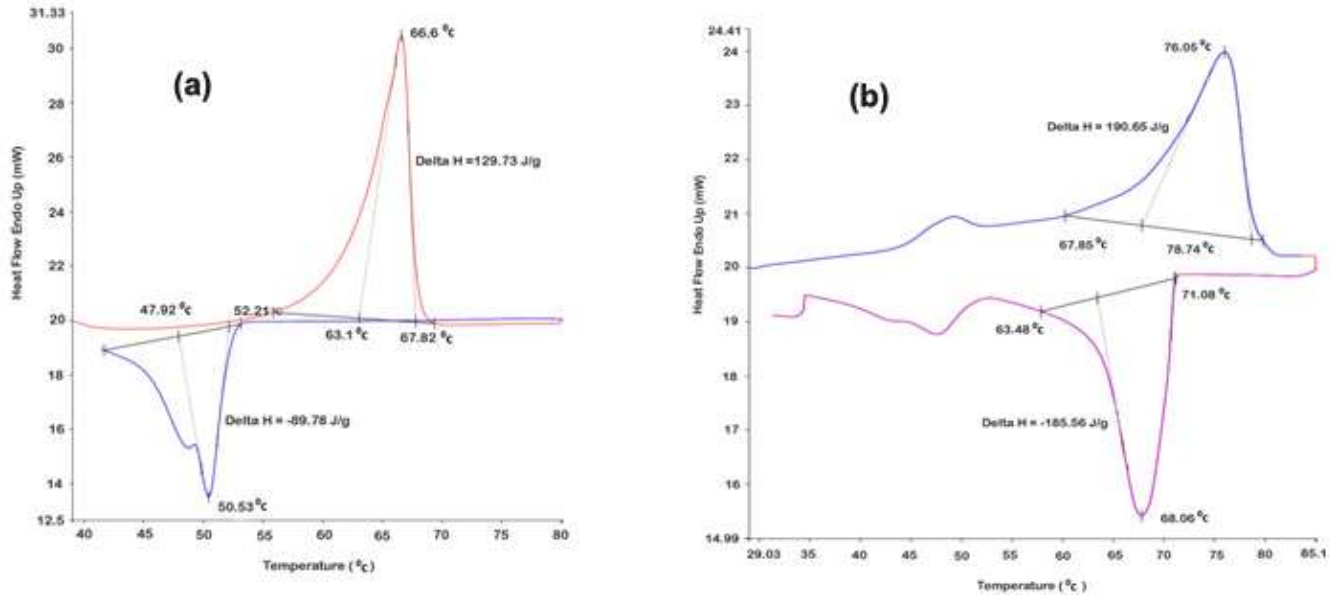

Figure 2 DSC graph of the LHMs: (a) CLW and (b) RBW.

ENERGY ANALYSIS

Energy analysis is an essential component in evaluating the performance and efficiency of any thermal system. Based on the first law of thermodynamics, it involves quantifying the energy input, transformation, and output. In solar thermal systems, energy analysis focuses on the conversion of incident solar radiation into usable thermal energy. This process is influenced by factors such as the intensity and wavelength range of the solar radiation. The efficiency of this conversion depends on how effectively the system captures and utilizes the available energy. For an ETC, the incident radiation energy is represented and analyzed as follows [11,14].

$$Q_c = A_p \cdot S.I \qquad (2)$$

Useful energy earned from the collector may be expressed in the following way [10,11]:

$$Q_u = \alpha \cdot \tau \cdot S.I \cdot A_p \qquad (3)$$

The useful energy transmitted into the ETC is harvested by the heat-carrying fluid (air) and computed with the help of the following energy equation:

$$Q_f = m_a \cdot C_p \cdot \Delta T \qquad (4)$$

The efficiency of the ETSAH system is described as the ratio between the heat energy acquired by the heat-carrying fluid to heat energy strike on ETC and is expressed as follows [11]:

$$\eta_c = Q_f / Q_c = m_a \cdot C_p \cdot \Delta T / A_p \cdot S.I \qquad (5)$$

RESULTS AND DISCUSSION

In this research work, the effect of the three different air velocities flowing through the ETSAH system, with and without TESM, is studied. During April 2024, the tests were performed under almost similar conditions on different days when the sky was almost clear. During the test-conducted days, the air temperature varied from 26 to 36 °C. The tests were conducted between 10:00 and 21:00, and data was collected every half an hour. Three different studies were analyzed, such as (i) ETSAH at a low air velocity, (ii) ETSAH at a medium air velocity, and (iii) ETSAH at a high air velocity.

Performance analysis of the ETSAH system at an airflow velocity of 1.5 m/s

The measurements were taken initially before the ETSAH system was exposed to solar radiation and also after exposure to solar radiation. The impact of a low airflow velocity (1.5 m/s) of the thermal energy-carrying fluid on the ETSAH system, both with and without TESM, is depicted in Fig. 3(a) and (b). These graphs illustrate the variations in inlet and outlet air temperatures, the temperature difference, and the solar radiation over time. The peak solar radiation recorded was 1004 W/m² at 13:00 as well as the solar intensity values of approximately 810-830 W/m² and an inlet air temperature of around 31 °C was consistently observed at 9:00, as shown in Figure 3(a) and also referenced in Figure 3(b).

Shortly after midday, the maximum solar irradiance began to decline. In the ETSAH system, the outlet air temperature and the air temperature difference strongly depend on both the incident solar radiation and the air velocity. Due to the high solar absorption capacity of the ETC and the relatively low air velocity (1.5 m/s), the residence time of air inside the collector is longer, allowing greater heat transfer to the fluid. Consequently, the outlet temperature increased substantially above ambient levels.

Based on the experimental results, the outlet air temperatures observed at 9:00 a.m. were approximately 43 °C, 49 °C, 51 °C, and 56 °C for the cases with no TESM, UEO, CLW, and RBW, respectively. Furthermore, after 16:00, as solar intensity declined, the temperature difference also started to decrease. From the experimental results, without any TESM in the ETC, the maximum inlet and outlet air temperatures reached 37 °C and 66 °C at

13:00. However, when filled with TESMs, the maximum outlet air temperatures increased to 95 °C (UEO), 104 °C (CLW), and 119 °C (RBW) respectively at the same time. This enhancement is attributed to the thermal energy storage capability of the TESMs, especially the LHS in CLW and RBW, which allows for the storage of solar heat during peak radiation and its release during lower radiation periods.

In ETCs filled with sensible heat material UEO, the maximum differential temperature achieved was 58 °C, while those filled with latent heat materials (CLW and RBW) achieved 67 °C and 82 °C respectively. In contrast, the system without TESM only achieved a 29 °C temperature difference. These results demonstrate that latent heat materials offer superior thermal buffering, maintaining higher outlet temperatures even as solar intensity fluctuates, due to their phase change properties, which absorb and release heat at nearly constant temperatures.

Figure 3(b) presents the system's efficiency variation over time. At an airflow velocity of 1.5 m/s, the efficiency of the system increased slightly up to 13:30. This is because the temperature difference between inlet and outlet air, which drives thermal energy gain, was increasing more significantly than the decline in solar irradiance. From 13:30 to 16:00, the efficiency remained relatively constant as both temperature differential and solar radiation balanced out. However, between 16:00 and 17:00, the efficiency increased sharply, despite decreasing solar intensity. The outlet air temperature is higher for collectors with TESMs, particularly with RBW and CLW compared to that without TESM due to the high thermal conductivity, high latent heat properties, and gradual thermal discharge behavior of the phase change materials, which prolong heat retention and enhance outlet temperatures during both low and moderate radiation periods [31,32].

The maximum system efficiency recorded at 17:30 was 9.8% without TESM, 36.7% with UEO, 42% with CLW, and 54.6% with RBW. This confirms that RBW, due to its higher latent heat capacity and effective phase transition temperature, is more effective at storing and releasing heat, thereby maintaining system output during declining solar periods. The higher thermal conductivity and better heat transfer characteristics of RBW also contribute to this superior performance. In summary, the experimental findings confirm that system efficiency is directly proportional to the temperature differential of the heat transfer fluid and inversely proportional to instantaneous solar intensity—a trend also reported in earlier studies on ETSAH systems at various mass flow rates [5,11,14].

Performances analysis of the ETSAH system at an airflow velocity of 2.0 m/s

The effect of a moderate airflow velocity (2.0 m/s) of the heat-carrying fluid in the ETSAH system, both with and without TESMs, is shown in Fig. 4(a) and (b). The graphs illustrate variations in inlet and outlet air temperatures, the corresponding temperature differences, and solar radiation over time. The maximum solar radiation was recorded at 1010 W/m² at 13:00. As expected, the solar intensity began to decline in the early afternoon due to the natural daily solar cycle.

Given the high absorptivity of the ETC and the increased velocity of the air stream (2.0 m/s), the outlet air temperature rose significantly above the ambient temperature. This is because the higher velocity enhances the convective heat transfer coefficient, promoting more effective energy exchange between the heated ETC surface and the passing air. Although higher velocities reduce the residence time of air within the tubes, the increased turbulence leads to improved heat pickup from the collector surface.

From the experimental data, without any TESM, the maximum inlet and outlet air temperatures were 39 °C and 66.5 °C respectively at 13:00. In contrast, the ETSAH filled with TESMs reached maximum outlet temperatures of 103 °C (UEO), 113 °C (CLW), and 130 °C (RBW), as shown in Fig. 4(a). This substantial improvement is attributed to the thermal buffering effect of TESMs, particularly those with LHS (CLW and RBW), which can absorb excess solar energy during peak irradiance and release it gradually over time.

The maximum differential air temperatures achieved were: 27.5 °C without TESM, 64 °C with UEO (sensible heat storage), 74 °C with CLW, and 91 °C with RBW. These results reinforce the superior performance of latent heat TESMs, as they provide higher energy density storage and a near-isothermal heat absorption/release process, which stabilizes and extends heat delivery to the working fluid. Additionally, the increase in airflow velocity from 1.5 to 2.0 m/s contributed to a rise in outlet temperature and air temperature difference. This improvement is due to the enhancement of the heat transfer rate at higher mass flow rates. Although higher velocity can reduce air residence time, the effect is compensated by the increased mass flow rate and convective heat exchange due to a thinner thermal boundary layer.

Figure 4(b) displays the system efficiency and solar radiation intensity over time at the 2.0 m/s inlet velocity. Initially, system efficiency increased slightly up to 13:00, as the temperature difference dominated over changes in solar input. From 13:30 to 16:00, the efficiency trend remained relatively flat. However, after 16:00, the system efficiency surged significantly. This is because TESMs, especially phase change materials (PCMs), released previously stored heat during the declining solar phase, decoupling the system's thermal output from immediate solar input.

The maximum system efficiencies recorded at 17:30 were: 12.3% without TESM, 49.2% with UEO, 57.8% with CLW, and 71.5% with RBW. The RBW-based Bio-PCM clearly outperformed other TESMs due to its higher latent heat, optimized melting point, and better thermal conductivity, allowing for more efficient charging and discharging cycles. Moreover, increasing the airflow velocity from 1.5 to 2.0 m/s led to an approximate 1.25 to 1.45 times increase in system efficiency across all TESM configurations. This emphasizes the importance of flow rate

optimization in enhancing thermal and exergy efficiency in SAHs. These findings align with prior studies on ETSAH systems operating at various airflow velocities, where researchers observed a strong correlation between higher airflow rates and improved thermal performance [3,6,17].

Performances analysis of the ETSAH system at an airflow velocity of 2.5 m/s

The effect of a high velocity (2.5 m/s) of the heat-carrying fluid in the ETSAH system with and without TESMs is illustrated in Fig. 5(a) and 5(b). These curves demonstrate the variations in inlet and outlet air temperatures, the corresponding temperature differentials, and solar radiation intensity over time. The peak solar radiation was observed to be 1020 W/m² at 12:30 p.m., followed by a gradual decline in intensity as the afternoon progressed, consistent with the daily solar cycle.

Due to the excellent solar absorption capability of the ETC surface and the elevated velocity of the airflow, the outlet air temperature significantly exceeded the ambient temperature. Increased airflow enhances the forced convective heat transfer mechanism, which not only improves the heat transfer coefficient but also promotes efficient heat exchange between the inner collector surface and the moving air. While faster airflow reduces the air's residence time inside the tubes, the improvement in turbulence and flow mixing compensates for this, resulting in a higher rate of thermal energy transfer.

From the experimental results: Without any TESM, the maximum inlet and outlet air temperatures were 39 °C and 70 °C, respectively, at 13:00. With TESMs, the maximum outlet temperatures at the same time were 108 °C (Engine Oil), 115 °C (CLW), and 133 °C (RBW), as shown in Fig. 5(a). Among the TESMs, RBW exhibited the highest outlet air temperature due to its high latent heat capacity and better thermal conductivity, which facilitated greater energy storage and release.

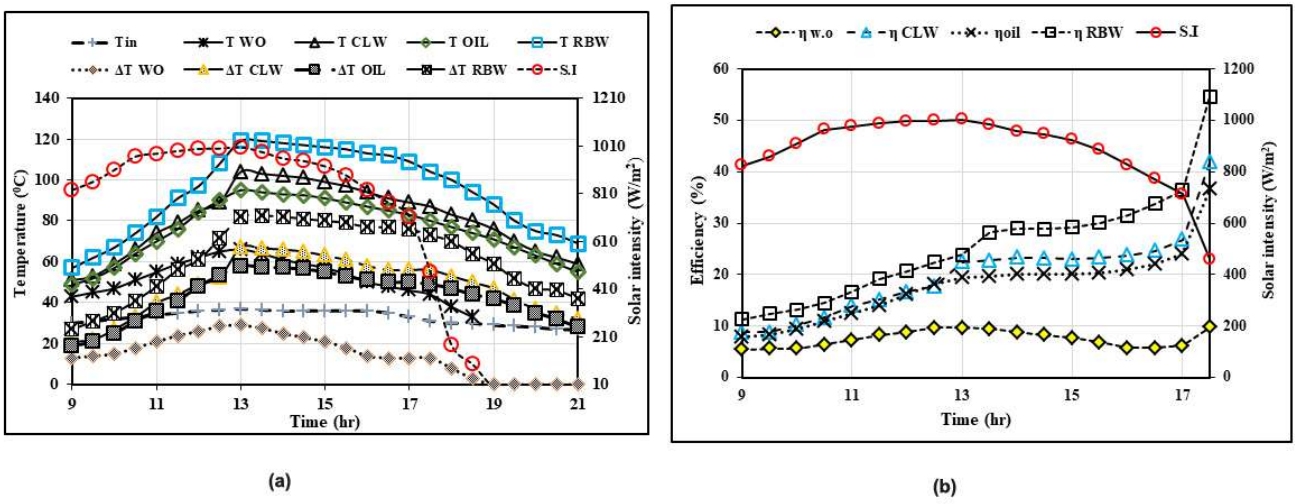

Figure 3 Variation of ETC system parameters at an air velocity of 15 m/s: (a) different temperatures and solar intensity vs time and (b) efficiency and solar intensity vs time.

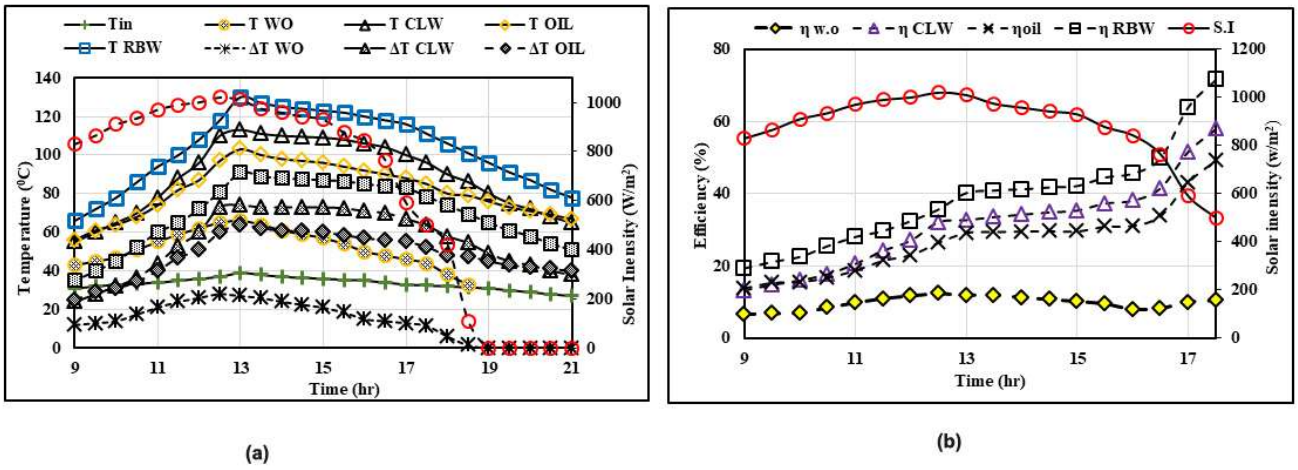

Figure 4 Variation of ETC system parameters at an air velocity of 20 m/s: (a) different temperatures and solar intensity vs time and (b)

efficiency and solar intensity vs time.

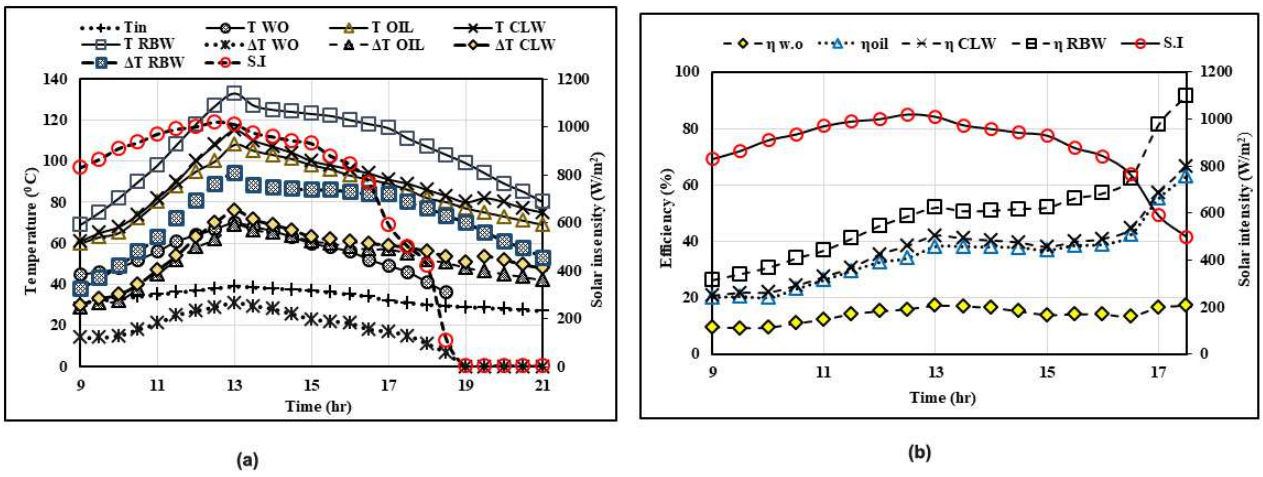

Figure 5 Variation of ETC system parameters at an air velocity of 25 m/s: (a) different temperatures and solar intensity vs time and (b) efficiency and solar intensity vs time.

The maximum differential air temperatures achieved were: 31 °C without TESM, 76 °C with CLW, and 94 °C with RBW.

These results emphasize the superior thermal regulation and heat retention capabilities of PCMs, particularly RBW. The phase change process in RBW enables it to store more thermal energy during periods of high solar intensity and release it steadily even when solar radiation declines. This study clearly shows that increasing the airflow velocity from 1.5 to 2.5 m/s significantly elevates the outlet air temperature and temperature difference. This enhancement is because of the increased convective heat transfer at higher velocities, as described by Newton's law of cooling.

Figure 5(b) displays the system efficiency and solar radiation intensity over time at an inlet velocity of 2.5 m/s. In all cases, system efficiency showed a slight increase up to 13:00 due to the dominance of temperature rise over the decreasing solar input. From 13:00 to 16:00, the efficiency curve remained relatively stable. After 16:00, efficiency increased sharply, attributed to the discharge of previously stored thermal energy by the TESMs, particularly the PCMs, during the period of reduced solar input.

The maximum system efficiencies at 17:30 were recorded as: 17.2% without TESM, 63.0% with UEO 66.4% with CLW, and 91.6% with RBW. The system integrated with RBW-PCM consistently achieved the highest efficiency, showcasing the material's capability to utilize both sensible and latent heat modes effectively. Compared to the system without TESM, the efficiency improvements ranged from 67% to 75% when increasing airflow velocity from 1.5 m/s to 2.5 m/s. Similar results have been reported in earlier research works that experimentally analyzed ETC-based SAHs under varying airflow rates [11,14], validating the observed trends in thermal performance and efficiency.

Finally, an overall comparison of Figs. 3 to 5 confirms that as the inlet air velocity increases, the thermal efficiency, temperature difference, and outlet air temperature also rise across all cases. This is primarily due to the forced convection heat transfer, which becomes increasingly dominant at higher velocities. Moreover, ETSAH systems integrated with TESMs significantly outperform those without, with RBW standing out as the most effective Bio-PCM due to its favorable thermal storage characteristics and discharge behavior, especially under variable solar radiation conditions.

CONCLUSIONS

1. The experiments conducted have led to the following conclusions:
2. The thermal efficiency of the system, temperature difference, and outlet temperatures of air were increased when the velocity of the heat-carrying fluid (air) increased from 1.5 to 2.5 m/s.
3. The efficiency of ETC-SAH using RBW as a TESM is positively influenced than UEO and CLW and also the efficiency of SAH with all TESMs is observed that be significantly superior to without TESM.
4. The highest air temperature difference of 76 °C and 91 °C was attained at a higher flow of air velocity of 2.5 m/s when CLW and RBW were used in the ETSAH, whereas without any TESM in the ETC, only 31 °C was achieved.
5. The peak efficiency of the system was observed as 91.6% and 17.2% for the ETSAH filled with RBW-PCM and without any TESM, respectively, at a higher flow of heat-carrying fluid velocity of 2.5 m/s.
6. The extreme outlet temperature of the air was attained at a flow velocity of 2.5 m/s, as 66.5 °C, 108 °C, 115 °C, and 133 °C without any TESM, filled with UEO CLW, and RBW respectively.

List of Abbreiations

CLW: Candelilla Wax
DSC: Differential scanning calorimeter
Q_c: Energy incident on the collector tube, W
Q_f: Energy absorbed by air, W

ETC: Evacuated Tube Collector
ETSAH: Evacuated Tube Solar Air Heater
HTF: Heat Transfer Fluid
T_{in}: Inlet temperature of the air at ETC system, °C
S.I: Intensity of solar radiation, W/m^2
LHSM Latent Heat Storage Material
m_a: mass flow rate of air, kg/sT_{out}: The outlet temperature of the air at ETC system , °C
PCM: Phase Change Materials
A_p: Projected area of evacuated tube solar air collector tube exposed to the sunlight, m^2
RBW: Rice Bran Wax
SHSM: Sensible Heat Storage Material
SAE: Society of Automotive Engineering
SAH: Solar Air Heater
C_{pa}: Specific heat of air, J/kg·K
ΔT: Temperature difference, °C
ΔT_{CLW}: Temperature difference with candelilla wax, °C
ΔT_{RBW}: Temperature difference with rice bran wax, °C
ΔT_{oil}: Temperature difference with used engine oil, °C
ΔT_{wo}: Temperature difference without use of thermal energy storage materials, °C
T_{CLW}: Outlet air temperature with candelilla wax, °C
T_{RBW}: Outlet air temperature with rice bran wax, °C
T_{oil}: Outlet air temperature with used engine oil, °C
T_{wo}: Outlet air temperature without the use of thermal energy storage materials, °C
TESM: Thermal Energy Storage Materials
UEO: Used engine oil
Q_u: Useful energy gained from the collector, W
20W/40 : Operating range at cold temperatures/ operating range at a high temperature

List of Symbols

α: Absorptance of the inner surface of the evacuated tube collector
τ : Transmittance of the collector tube
η_c: Evacuated tube solar air heater efficiency
η_{CLW}: Thermal efficiency with candelilla wax
η_{RBW}: Thermal Efficiency with rice bran wax
η_{oil}: Thermal efficiency with used engine oil
$\eta_{w.o}$: Thermal efficiency without the use of thermal energy storage materials

ACKNOWLEDGMENTS

The corresponding author wishes to the deepest gratitude to TEQIP-III, New Delhi, and also express the sincere thanks to the Department of Mechanical Engineering, Government College of Engineering, Bargur, Krishnagiri, and Tamilnadu.

REFERENCES

[1] M. Abuşka, S. Şevik, A. Kayapunar, Appl. Therm. Eng. 148 (2019) 684-693. https://doi.org/10.1016/j.applthermaleng.2018.11.056
[2] M. Chaabane, H. Mhiri, P. Bournot, Energy Convers. Manag. 78 (2014) 897-903. https://doi.org/10.1016/j.enconman.2013.07.089.
[3] K. Chopra, A.K. Pathak, V.V. Tyagi, A.K. Pandey, S. Anand, A. Sari, Energy Convers. Manag. 203 (2020) 112205. https://doi.org/10.1016/j.enconman.2019.112205.
[4] R. Barathiraja, P. Thirumal, G. Saraswathy, I. Rahamathullah, Chem. Ind. Chem. Eng. Q. 28(3), (2022) 169-178. https://doi.org/10.2298/CICEQ201120028B.
[5] S.Y. Kee, Y. Munusamy, K.S. Ong, Appl. Therm. Eng. 131 (2018) 455-471. https://doi.org/10.1016/j.applthermaleng.2017.12.032
[6] A.E. Khadraoui, S. Bouadila, S. Kooli, A. Guizani, A. Farhat, Appl. Therm. Eng. 107, (2016) 1057-1064. https://doi.org/10.1016/j.applthermaleng.2016.07.004.
[7] M.M.A. Khan, N.I. Ibrahim, I.M. Mahbubul, H.M. Ali, R. Saidur, F.A. Al-Sulaiman, Sol. Energy. 166 (2018) 334-350. https://doi.org/10.1016/j.solener.2018.03.014.
[8] R. Senthil, Energy Sources, Part A. 44(1) (2019) 2374-2384. https://doi.org/10.1080/15567036.2019.1649751.
[9] A. Kumar, S. Kumar, U. Nagar, A. Yadav, J. Sol. Energy. 1 (2013) 524715. https://doi.org/10.1155/2013/524715.
[10] S. Kumar, A. Kumar, A. Yadav, Int. J. Sustain. Eng. 8 (2014), 280-293. https://doi.org/10.1080/19397038.2013.878001.
[11] V.V. Tyagi, A.K. Pandey, S.C. Kaushik, S.K. Tyagi, J. Therm. Anal. Calorim. 107 (2012) 1345-1352. https://doi.org/10.1007/s10973-011-1617-3.
[12] M. Leckner, R. Zmeureanu, Appl. Energy. 88 (2011) 232-241. https://doi.org/10.1016/j.apenergy.2010.07.031.
[13] P. Manoj Kumar, K. Mylsamy, P.T. Saravanakumar, Energy Sources, Part A. 42 (2020), 2420-2433. https://doi.org/10.1080/15567036.2019.1607942.
[14] S. Nain, A. Parinam, S. Kajal, Int. J. Ambient Energy. 39 (2017), 143-146. https://doi.org/10.1080/01430750.2016.1269677.
[15] N.L. Panwar, S.C. Kaushik, S. Kothari, S., Renewable Sustainable Energy Rev. 15 (2011) 1513-1524. https://doi.org/10.1016/j.rser.2010.11.037.
[16] S. Riffat, B. Mempouo, W. Fang, Int. J. Ambient Energy. 36 (2013) 102-115. https://doi.org/10.1080/01430750.2013.823106.
[17] Sari, A. Karlı, C. Alkan, A. Karaipekli, Energy Sources, Part A. 35 (2013). 1813-1819. https://doi.org/10.1080/15567036.2010.531507.
[18] S.B. Sasikumar, H. Santhanam, M.M. Noor, M. Devasenan, H.M. Ali, Energy Sources, Part A. (2020)1-13. https://doi.org/10.1080/15567036.2020.1829201.
[19] D. Singh, P. Mall, Energy Sources, Part A. (2020) 1-18. https://doi.org/10.1080/15567036.2020.1810825.
[20] Yaswanthkumar, V.P. Chandramohan, J. Therm. Anal. Calorim. 136 (2019) 331-343. https://doi.org/10.1007/s10973-018-7756-z.
[21] L. Liu, R. Wang, Y. Wang, W. Li, J. Sun, Y. Guo, C. Zhao, Energy Convers. Manag. 275 (2023) 116464. https://doi.org/10.1016/j.enconman.2022.116464.
[22] R.I. Rubel, M.W. Akram, M.M. Alam, A. Nusrat, R. Ahammad, M.A. Al-Bari, Arabian J. Sci. Eng. 49

(2024) 14533-14551. https://doi.org/10.1007/s13369-024-09519-z.
[23] S. Jain, S.K. Dubey, K.R. Kumar, D. Rakshit, (2021) 167-215. https://doi.org/10.1007/978-981-33-6456-1_9.
[24] N. Ning, C. Sun, Z.J. Ma, S. Guo, S. Jiang, J. Zhang, D. Hou, C. Wang, J. Energy Storage. 114 (2025) 115814. https://doi.org/10.1016/j.est.2025.115814.
[25] F.L. Rashid, M.A. Al-Obaidi, N.S. Dhaidan, A.K. Hussein, B. Ali, M.B.B. Hamida, O.Younis, J. Energy Storage. 73 (2023) 109219. https://doi.org/10.1016/j.est.2023.109219.
[26] N.S. Dhaidan, M.S.M. Al-Jethelah, 12th IIR Conference Orford , Canada. May 21-23 (2018) 240-47. https://doi.org /10.18462/iir.pcm.2018.0033.
[27] F.L. Rashid, N.S. Dhaidan, A.J. Mahdi, S.A. Kadhim, K.A. Hammoodi, M.A. Al-Obaidi, H.I. Mohammed, S. Ahmad, S. Salahshour, E.B. Agyekum, Int. Commun. Heat Mass Transf. 162, (2025) 108573. https://doi.org/10.1016/j.icheatmasstransfer.2024.108573.
[28] A.M. Ahangar, A. Rahmani, M. Maleki, R. Ahmadi, S.H. Razavi, Sol. Energy Mater. Sol. Cells. 277 (2024) 113084. https://doi.org/10.1016/j.solmat.2024.113084.
[29] F.L. Rashid, N.S. Dhaidan, A.J. Mahdi, H.N. Azziz, R. Parveen, H. Togun, R.Z. Homod, Int. Commun. Heat Mass Transf. 159 (2024) 108096. https://doi.org/10.1016/j.icheatmasstransfer.2024.108096.
[30] NematpourKeshteli, M. Iasiello, G. Langella, N. Bianco, Therm. Sci. Eng. Prog. 52 (2024) 102690. https://doi.org/10.1016/j.tsep.2024.102690.
[31] S. Ganapathiraman, P. Manickam, J. Energy Storage. 84 (2024) 110929. https://doi.org/10.1016/j.est.2024.110929.
[32] Uniyal, Y.K. Prajapati, D. Kumar, Appl. Energy. 377 (2025) 124501. https://doi.org/10.1016/j.apenergy.2024.124501.

RAJASEKAR CHOCKLINGAM[1]

RAMESHKUMAR RAMASAMY[2]

BARATHIRAJA RAJENDRAN[3]

[1]Department of Mechatronics Engineering, Akshaya College of Engineering and Technology, Tamil Nadu, India

[2]Department of Mechanical Engineering, Builders Engineering College, Tamil Nadu, India

[3]Department of Mechanical Engineering, Mahakavi Bharathiyar College of Engineering & Technology, Tamil Nadu, India

NAUČNI RAD

UTICAJ INTEGRACIJE MATERIJALA ZASKLADIŠTENJE TOPLOTE U CEVASTOM VAKUUMSKOM PRIJEMNIKU

Cilj ovog eksperimentalnog istraživanja je procena uticaja materijala za skladištenje osetne i latentne toplote, kao što su SAE 20W/40 (korišćeno motorno ulje), kandelila vosak i vosak pirinčanih mekinja, na performanse solarnog vakuumskog cevastog grejača vazduha (ETSAH). Proučavana su četiri različita rasporeda: jedan bez materijala za skladištenje toplotne energije, jedan sa materijalom za skladištenje osetne toplote i dva sa materijalima za za skladištenje latentne toplote, kako bi se omogućila uporedna analiza. Maksimalna izlazna temperatura vazduha za cevasti vakuumski prijemnik napunjen korišćenim motornim uljem, kandelila voskom ili voskom pirinčanih mekinja bila je 108 °C, 115 °C i 133 °C, redom (sve mereno u 13,00 časova). Međutim, izlazna temperatura u sistemu bez punjenja bila je samo 70 °C. Maksimalna temperaturna razlika vazduha u ETSAH sistemu napunjenom kandelila voskom bila je 94°C, dok je, za sistem bez punjenja ona bila samo 31°C u 13,00 časova. Maksimalna efikasnost ETSAH sistema postignuta je korišćenjem kandelila vosak. Štaviše, efikasnost sistema se povećava oko 1,7- 1,8 puta kada se brzina vazduha poveća sa 1,5 na 2,5 m/s.

Ključne reči: Cevasti vakuumski prijemnik, latentna toplota, osetna toplota; materijal za skladištenje toplote; vosak pirinčanih mekinja; kandelila vosak.

CI&CEQ
Chemical Industry & Chemical Engineering Quarterly

Available online at
Association of the Chemical Engineers of Serbia AChE
www.ache.org.rs/CICEQ

Chem. Ind. Chem. Eng. Q. 32 (2) 111–122 (2026) CI&CEQ

SRINIVASAN KASINATHAN NARENDRANATHAN[1]

KARTHIKEYAN SUBRAMANIAN[2]

PURUSHOTHAMAN PANNEERSELVAM[1]

SRINIVASAN TIRUPATHI[2]

[1] Department of Mechanical Engineering, Agni College of Technology, Tamil Nadu, India.

[2] Department of Mechatronics Engineering, Agni College of Technology, Tamil Nadu, India.

SCIENTIFIC PAPER

UDC 662.756.3:661.722:667.63:621

ANALYZING THE EFFICACY AND EXHAUSTS OF PUNNAI BIODIESEL-ETHANOL BLENDS IN NANOCOATED CI ENGINES

HIGHLIGHTS

- The performance of a nanocoated CI engine is tested using ethanol, punnai oil, and diesel.
- PB-ethanol mixtures reduced NOx, CO, smoke opacity, and nanocoating improved engine efficacy.
- The best performance-to-emissions ratio was Punnai biodiesel/ethanol.
- Punnai biodiesel-ethanol mixes show promise as sustainable fuels.
- An alternative production process of difurfuryl ether useful to the food industry.

Abstract

This study experimentally investigates the performance, emission, and combustion characteristics of a nano-coated compression ignition (CI) engine fueled by Punnai biodiesel blends with varying proportions of ethanol. The nano-coating was applied to the engine's cylinder liner and piston crown to enhance heat transfer and reduce friction. The biodiesel blends were prepared by mixing Punnai oil with diesel fuel in various ratios (B20, and B30). Ethanol was added to each blend at 5% and 15% concentrations. This research desires to improve the operational efficiency of an engine that runs on diesel, through the utilisation of a piston coated with a thermal barrier, specifically tailored for punnai methyl ester blends. Thermal barrier coatings widely prioritise zirconia due to its exceptional thermal insulation properties. B20E15 has a brake thermal efficiency that exceeds that of diesel by around 3%. Similarly, B20E05 and B20E15 demonstrate fuel consumption reductions of approximately 3.8% and 16.3%, respectively. On average, the B20 blends exhibited a reduction in CO and HC emissions are 5% and 9%. A comparative analysis clearly demonstrated that nanocoated CI engines enhance performance and diminish emissions without any major modifications.

Keywords: Punnai biodiesel, ethanol, nano-coating, diesel engine, efficacy, exhausts.

INTRODUCTION

Globally, fuel demand has increased day by day due to logistic infrastructure expansion, fast-growing transport, and high-speed transit [1]. Developing countries rely heavily on fossil fuels as their major mode of transportation. Because of rapid population growth and industrialization, 60% of energy growth will come from fossil fuels. By 2040, it will provide 80% of the world's energy [2]. Although India ranks twenty-first in crude oil production, it holds the third position in terms of crude oil consumption. There exists a substantial disparity between the demand for and production of oil. The observed disparities in crude oil inventory indicate India's significant dependence on imported crude oil [3]. The price of crude oil and growing exhaust gas emissions are the two main things to take into account while utilising diesel as a fuel in an internal combustion engine (ICE) [4]. Transient urban divisions and emissions at the road level present a significant environmental hazard and adversely affect human health. Prolonged exposure can result in the development of lung cancer, asthma, cardiorespiratory disorders, hypersensitivity, and hypertension in humans [5]. The environmental deterioration and significant increase in the usage of fossil fuels underscore the potential of biodiesel as a viable alternative to diesel [6]. This study highlights fuel conversion efficiency and alternatives to diesel. Biodiesel might serve as a feasible fuel for diesel engines owing to its

Correspondence: S.K. Narendranathan, Department of Mechanical Engineering, Agni College of Technology, Chennai-600130. Tamil Nadu, India.
Email: sknarengopi@gmail.com
Paper received: 9 October, 2024
Paper revised: 16 April, 2025
Paper accepted: 9 June, 2025

https://doi.org/10.2298/CICEQ241009015S

lubricating properties and accessibility. This alternative fuel produces more NO_x emissions and possesses a lower calorific value, higher viscosity, and more density compared to diesel. Madhuca indica, Simmondsia chinensis, Calophyllum inophyllum, algae, animal fats, and discarded cooking oils can be utilised to produce biodiesel [7]. Biodiesel has grown in popularity due to its non-toxicity. They have sulphur, oxygen, and a higher cetane number than fossil diesel. Usually, biodiesel emits less than diesel. Biodiesel's lubricity helps engine parts move. One can produce biodiesel using various methods. The process includes first, second, and third-generation feedstock [8].

Traditionally, second-generation biofuels were made from wood residual waste, agricultural waste, and energy crops. Negative or neutral carbon emissions from second-generation biofuels. The seasonal dependence on raw materials is the second-generation fuel's biggest drawback [9]. In this study of biodiesel production, raw Punnai oil from the kernel of the Punnai tree (*Calophyllum inophyllum*) is accessible in considerable amounts. Punnai biodiesel yields more oil and heats better than Pongamia, Neem, and Jatropha in Africa and Asia [10]. In addition to the aforementioned benefits, there are notable drawbacks. Use biodiesel exclusively in diesel engines. Biodiesel has consistently shown higher BSFC and NO_x emissions compared to fossil fuel while exhibiting lower BTE and ITE emissions [11]. This study examines the impact of incorporating ethanol into biodiesel-diesel mixtures on the efficiency and exhaust emissions of a CI engine and the results indicate that the incorporation of biodiesel marginally influences engine power at low and medium velocities while enhancing power by around 6% at high velocities. The addition of ethanol greatly improves engine power, with a 16% boost at 1700 rpm and a 13% boost at 2500 rpm for 2.5% and 5% ethanol blends, respectively [12]. The investigation was done on a single-cylinder, four-stroke diesel engine at constant speed under varying loads. These test results optimize the engine load and palm biodiesel/ethanol ratios in diesel-biodiesel-ethanol ternary blends. The research showed that when 11.06% palm biodiesel was used, the best levels of brake thermal efficiency (BTE), nitrogen oxide (NO_x), carbon monoxide (CO), and unburnt hydrocarbon (UHC) emissions were at 43.4% of capacity. These levels were 12.57%, 436.2 ppm, 0.03 vol.%, and 79.2 ppm [13]. This study is to assess the effects of nanoparticles in diesel fuel. Different techniques for enhancing engine performance are studied. Nanoparticles are crucial in the advancement of biofuels, from feedstock preparation to chemical reactions. In contrast to blends devoid of alcohol or those with alcohol, whether including nanoparticles or not, the incorporation of nanoparticles into biodiesel-diesel blends decreases brake-specific fuel consumption by 18% to 20%. Furthermore, nanoparticles exhibit exceptional heat conductivity, enhancing braking performance by 2% to 5% and optimizing combustion [14].

Further study is being conducted on internal combustion engines to mitigate expenditure on fuel and maintenance, as well as minimising fuel utilisation. The utilisation of sophisticated ceramic technologies has facilitated the implementation of structural modifications as a means to enhance engine efficiency. These coatings were initially observed in gas turbines and aviation engines [14]. In this research, the coatings of ceramics might boost the performance of an engine and lower exhaust by reducing the rejection of heat from the cylinder to the cooling system. Utilize the maximum feasible amount of fuel energy. Convert into usable mechanical power. Cover the combustion chamber of an engine to get those results. Newer ceramic materials, which conduct less heat, may increase cylinder temperature and pressure [15]. The nanoparticles have unique physical and chemical properties, including the ability to catalyze reactions, conduct heat, have a higher surface-to-volume ratio, and be more stable because they are so small and move in a Brownian motion. Nanoparticles greatly improve the performance and emissions of current compression ignition (CI) engines by making the combustion process better and breaking up the fuel droplets into small particles. [16]. this research shows that an IC engine with a Nano powder-based thermal barrier coating reduces fuel consumption and increases thermal efficiency. This work reported that the thermal barrier-coated engines increase performance and reduce emissions like HC and CO. NOx emissions increased with combustion temperature [17]. The combustion factors impact output power, pollutants, fuel utilisation, the vibration of an engine, and sound. The pressure as well as the temperature of air that has been compressed has an impact on the combustion delay. During compression, the cooling and heat-absorbing systems absorb heat. Barrier-coated thermal reduced heat loss can boost engine power. The engine is resistant to high temperatures and has minimal heat conduction. Compounds covering the combustion spaces [18]. Thermal barriers improved thermal and mechanical effectiveness; decreased emissions and lower fuel usage have made engine components popular. Insulation can reduce emissions by oxidizing hydrocarbon combustion soot precursors with engine waste heat [19]. Zirconia coatings on engine components like pistons, inlet and exhaust valves, and cylinder liners have lower heat conductivity. When used in conjunction with a glow plug, ethanol reduces tailpipe emissions but is less fuel-efficient than diesel fuel. Nevertheless, delaying the injection time helps considerably improve the thermal efficiency of the engine. As the combustion temperature rises, the outcome is improved thermal efficiency, reduced emissions of carbon monoxide and unburned hydrocarbons, and increased emissions of nitrogen oxide [20]. Ceramic materials are well-suited for high-temperature applications because of their elevated melting temperatures, robust adhesion, and resilience to wear. Enclosing combustion chamber components is a good application for ceramics. Covered engines provide superior heat retention capabilities within the combustion chamber. Thus, engine emissions and fuel consumption decrease [21]. A study contrasted a nanocoated piston with two coated pistons of different coating thicknesses. The biofuel made a lasting impact.

Similar to diesel-fueled trials on coated and nano-coated pistons, coating thickness boosts thermal efficiency, fuel consumption, and pollutant reduction [22].

The above research shows that biodiesel reduces greenhouse gas emissions and blends well with diesel. In diesel fuel, biodiesel reduces BTE and increases SFC. Diesel-biodiesel mixed fuel has worse combustion properties than diesel fuel. As biodiesel content increased, NOx emissions rose. A small amount of ethanol can lessen the restrictions on biodiesel-blended fuel. This study explores the impact of ethanol on Punnai biodiesel in 20% and 30% mixes with pure diesel. Nano coating a single-cylinder diesel engine to evaluate its performance and emissions under different load conditions.

EXPERIMENTATION AND PROCEDURES

Punnai Oil Source:

The Punnai tree, or Calophyllum inophyllum, is a tropical perennial that thrives in the coastal areas of Southeast Asia, such as India, Sri Lanka, and the Pacific Islands. It holds a special place in Tamil culture due to its robust, long-lasting wood and its various applications in traditional healing practices. The seeds of the tree yield oil that is celebrated for its skin-friendly benefits and possible healing properties. The evergreen *C. inophyllum* tree has uneven branches and grows to an average height of 8 - 20 m (25 - 65 ft). This medium and big coastal tree has 25-mm blooms and elliptical, lustrous, robust leaves. The panicle of this tree contains 4–15 flowers and spherical, green drupes that are 2–4 cm (0.8–1.6 in.) in diameter. Ripe fruit is wrinkled and yellow to brownish-red. Grey, odourless, and ligneous nuts make up the fresh, pale yellow kernel. C. inophyllum kernels yield 50–75% oil, which is useful in medicine and cosmetics. A 3-year-old tree produces approximately 22-100 kg seeds annually. These trees generally live approximately 50 years and are located in mild to warm Indian Sea coastal locations. They are prevalent in 1000–5000 mm rainfall zones.

Availability of Punnai Bio-oil and its Impact on IC Engine:

Punnai trees (Calophyllum inophyllum) are common in coastal India, especially in Tamil Nadu, Kerala, and Andhra Pradesh, where their seeds are used for medical purposes. Punnai seed oil seems promising as a biofuel for internal combustion engines. Many biodiesel manufacturing advantages come from these seeds' oil. Furthermore, its high oxidative stability inhibits oil degradation, extending shelf life and improving engine performance. Punnai oil offers an environmentally beneficial alternative to diesel due to its low sulphur level. Due to its diesel-like viscosity, Punnai oil's lubricity reduces engine wear and enables its use in I.C. engines without any modifications. Punnai's oil biodiesel contains a higher cetane number, which improves engine performance and fuel efficiency. Punnai seed oil lowers carbon emissions and fossil fuel use by providing renewable energy. Punnai oil's technical merits and popularity in India might help the country promote sustainable energy and reduce environmental effects. Figure 1 (a) shows the oil extraction process of Punnai bio-oil.

The novelty of Punnai oil Utilization:

The technical novelty of using Punnai oil (Calophyllum inophyllum) as a biodiesel source is attributed to its distinctive fatty acid composition, elevated free fatty acid levels, and advantageous fuel characteristics. The composition necessitates a two-step transesterification process that, when optimised, produces biodiesel with a high cetane number (>50), flash point (>160 °C), and density (0.87–0.89 g/cm³) compliant with ASTM requirements. Notwithstanding somewhat increased viscosity, it provides enhanced lubricity, superior combustion quality, and oxidative stability. Punnai biodiesel, which has a heat value of 38–41 MJ/kg, is suitable for diesel engines, making it a practical, non-food, and sustainable source of biodiesel.

GC-MC Analysis of Punnai Bio-Oil

The produced sample underwent purification for Punnai biofuel through the process of distillation. The level of bio-oil was determined through gas chromatography (Thermo Scientific), equipped with a flame ionization detector (FID). The setup included a TG-Wax MS column with a length of 30 m, an internal diameter of 0.25 mm, and a film thickness of 0.25 µm. The oven's temperatures increased steadily at a rate of 7 °C per minute, starting from 40 °C and reaching 180 °C. Meanwhile, the injector was kept at 230 °C, and the detector was maintained at 250 °C. Before injecting into GC, samples were filtered using 0.22 µm syringe filters. The high-purity nitrogen served as the carrier gas, while the flask generated zero air and hydrogen gases. Figure 1(b) and Table 1 show the retention time in minutes along the x-axis and the range of potential ethanol sources on the y-axis. The retention time of biofuel produced from Punnai seed oil is 2.59 minutes, suggesting that the standard time for bio-oil production closely aligns with the actual retention time observed.

Free Fatty Acid Composition:

The composition of fatty acids Gas chromatography analysed the free fatty acid content of Punnai's oil biodiesel, as seen in Figure 1 (c) and Table 2. Punnai oil biodiesel/methyl ester has 24% saturated methyl esters and 76% unsaturated methyl esters. Punnai oil contains a significant concentration of unsaturated fatty acids, with 34.29% oleic acid and 41.711% linoleic acid. These unsaturated fatty acids improve cold flow and combustion efficiency, while linoleic concentration may diminish oxidative stability. Palmitic acid (C16:0) is the most common saturated fatty acid at 14.88%, while stearic acid (C18:0) adds 6.23%, increasing biodiesel cetane number and storage stability. In tiny doses, 0.52% and 0.43% of lauric acid (C12:0) and myristic acid (C14:0) promote lubricity. Linolenic acid (C18:3), at 0.07%, is extremely unsaturated and oxidative, which improves fuel stability. With a balanced blend of saturated and unsaturated fatty acids, Punnai oil-derived biodiesel should meet fuel standards for ignition quality, viscosity, and oxidative stability.

FTIR:

The vibrational approach Fourier transform infrared spectroscopy (FTIR) finds organic compounds on biofuel surfaces. It helps qualitatively evaluate materials and comprehend organic groupings [37]. The Perkin Elmer spectrum two FTIR analyser identified chemical bonds, functional groups, and the vibrations of Punnai oil (either bending or stretching). FTIR examined Artocarpus heterophyllus peel biofuel. Figure 1(c) presents the FTIR spectrum data for the biodiesel sample, with the wavenumber (cm^{-1}) plotted against transmittance (%). Table 4 displays the measurements from the Perkin Elmer machine of functional group vibrations (500–4000 cm^{-1}) for solids and liquids, including amide, aldehyde, alkyl, ester, anhydride, phenolic, carboxylic, ketonic, and many other vibrations.

Test Sample and its Properties

The current study seeks to examine the effects of adding ethanol to nanocoated pistons powered by Punnai biodiesel. The study involved blending biodiesel from the Punnai seed biodiesel transesterification process with diesel fuel at varying volume ratios of 20% and 30%. Additionally, we added oxygenated ethanol additives at concentrations of 5% and 15%. The fuel for the nanocoated engine (NCE), known as B20E05, is a blend of 20% Punnai biodiesel (B20), 5% volumetric ethanol, and 75% pure diesel. Formulate the biodiesel fuel blends as follows: B20E15, which is 65% diesel, 20% Punnai biodiesel, and 15% ethanol; B30E05, which is 65% diesel, 30% Punnai biodiesel, and 5% ethanol; and B30E15, which is 55% diesel, 30% Punnai biodiesel, and 15% ethanol. Table 3 displays the test sample's properties.

Table 1 GC-MS analysis

Fatty Acids	Formula	Systematic name	Retention Time
Lauric acid	$C_{12}H_{24}O_2$	Dodecanoic acid (C12)	21.48
Myristic acid	$C_{14}H_{28}O_2$	Tetradecanoic acid (C14)	26.76
Palmitic acid	$C_{16}H_{32}O_2$	Hexadecanoic acid (C16)	15.68
Stearic acid	$C_{18}H_{38}O_2$	Octadecanoic acid (C18)	18.00
Oleic acid	$C_{18}H_{34}O_2$	Cis-9- Octadecanoic acid (C18:1)	26.54
Linoleic acid	$C_{18}H_{32}O_2$	Cis-9-cis12-Octadecanoicacid (C18:2)	22.14
Arachidice acid	$C_{20}H_{40}O_2$	Eicosanoic acid (C20)	27.13
Behenic acid	$C_{22}H_{44}O_2$	Docosenoic acid (C22)	24.06

Table 2 Functional group-based FTIR

Wave Number (cm^{-1})	Experimental Results (cm^{-1})	Organic Groups and Their Nature	Chemical Formation
3100-3500	3453, 3477, 3476	O-H & Stretching	Alcoholic, Phenolic
2800-3000	3453, 3477, 3476	O-H & Stretching	Alkanes
1680-2700	1750, 1745, 2027	C-H & Bending	Aromatic
1250-1650	1625, 1469, 1456	C=C & Stretching	Alkenes
1200-1000	1170, 1164, 1105	C-O & Stretching	Ester
1000-500	776, 728, 721	COO & Stretching	Carboxylic

Table 3 test sample's properties

Properties	ASTM Standard	Diesel	Punnai Biodiesel	Ethanol	Instrumentation
Kinematic viscosity (at 40 °C) (cst)	D 445	2.42	4.88	1.52	Red Wood viscometer
Density at15 °C (kg/m^3)	D 941	830	867	720	Hydrometer
LHV (MJ/kg)	D 240	42.5	40.39	26.92	Bomb Calorimeter
HHV (MJ/kg)		45.5	42.31	29.7	
Cetane Index	D 613	54	49	10	Ignition Quality Tester
Flash point (°C)	D 93	58	165	13	Pensky Martins Apparatus

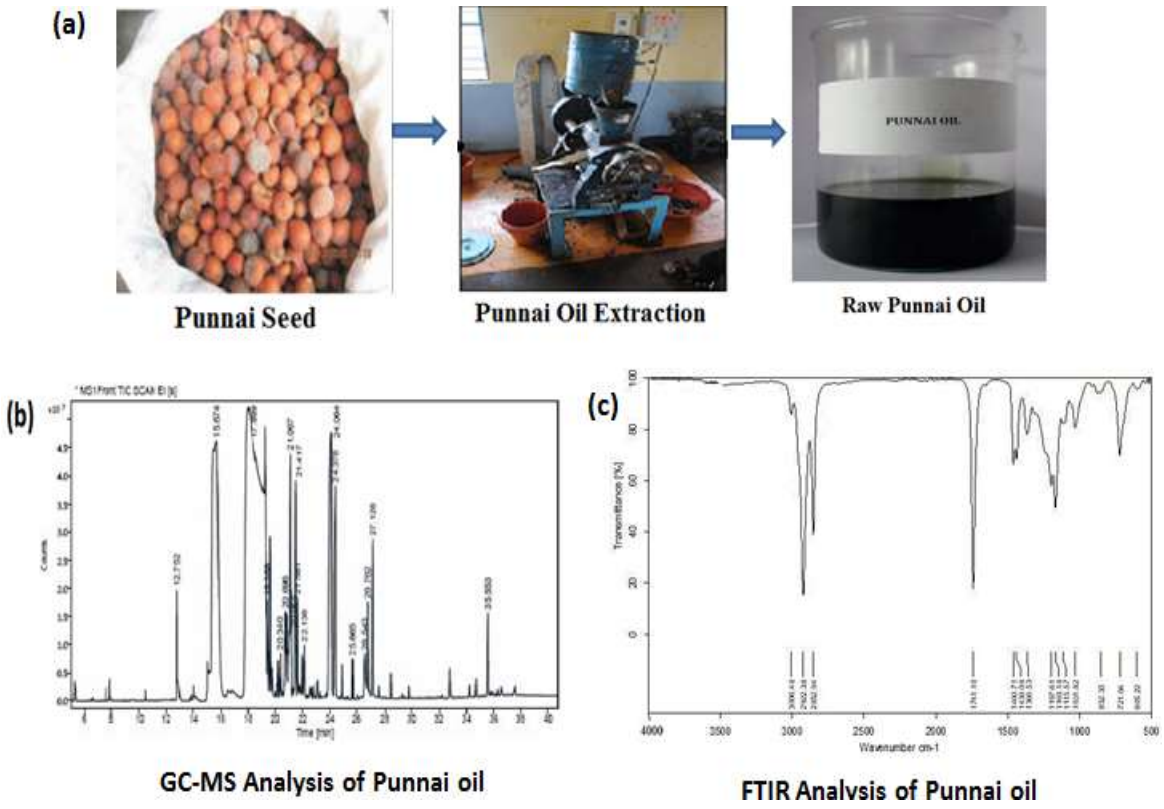

Figure 1 (a) Punnai oil extraction, (b) GC-MS analysis, and (c) FTIR analysis.

Table 4 Engine specifications

Make and Model	Kirloskar, TV1
Number of cylinders/Stroke	One/Four
Bore x Stroke	87.5 x 110 mm
Compression ratio	17.5:1
Swept volume	661cc
Maximum power output	5.2 kW at 1500rpm
Lubricating oil	SAE40
Cooling system	Water cooled
Injection pressure	210 bar
Standard Injection timing, CA bTDC	23

Test Engine and Facilities

Figure 1 shows the design of a compression ignition engine with attached instrumentation, where the prepared test fuel undergoes testing. Table 4 lists engine specs. Water-cooled eddy current dynamometers are powered by engines on base frames with universal propeller shafts. The sensors are installed at acceptable places and linked to the engine test panel to display engine torque and speed, which are utilised to calculate braking power. A high-speed digital data collection system collected pressure and TDC signals, which were stored on a computer to calculate engine combustion parameters. The AVL Digas 444 analysed NO_x, HC, CO, and CO_2 exhaust pollutants. The opacity of smoke was calculated with the help of an AVL 437C smoke gauge.

Error Analysis

In this section, the errors linked to the different metrics were calculated using the approach proposed by [31]. We computed the associated errors for the lowest possible values of the instrument's output and quality. To get the margin of error for an estimated quantity S that is dependent on a set of independent variables (X_1, X_2, X_3... X_n), one can use Eq. (1).

$$\frac{\partial S}{S} = \left\{\left(\frac{\partial X_1}{X_1}\right)^2 + \left(\frac{\partial X_2}{X_2}\right)^2 + \cdots + \left(\frac{\partial X_n}{X_n}\right)^2\right\}^{\frac{1}{2}} \quad (1)$$

The experimental minimum value of the output is

denoted by X_1 and the errors in the independent variables ∂X_1 with respect to the measuring instrument's precision are denoted by $\left(\frac{\partial X_1}{X_1}\right)$,$\left(\frac{\partial X_2}{X_2}\right)$, etc.

BTE and SFC calculation errors maxed out at 0.38 %. Cylinder pressure and crank angle errors were 0.25 and 2%, respectively. Analyser specs allow for a maximum error of 5% in measuring smoke opacity and NO_x emission.

Test procedure

Initially, the experiment was conducted in controlled environmental conditions using Punnai biodiesel and diesel blend (B20) in an unmodified engine. Prior to each observation, the engine was run for 5 minutes to generate a condition of equilibrium. Moreover, the experiments were carried out by incorporating ethanol at volumes of 5% and 15% into the diesel fuel. The ideal blend was determined to be B20%, with a compression ratio of 17.5. The injection time was set at 23º bTDC. The test results were arranged in ascending order of load, ranging from 25% to 100%. The engine trials will be conducted using four specific test fuels, namely: (1) diesel fuel, (2) B20E05 (20% biodiesel + 5% ethanol), (3) B20E15 (20% biodiesel + 15% ethanol), (4) B30E05 (30% biodiesel + 5% ethanol), and (5) B30E15 (30% biodiesel + 15% ethanol). Experimental investigations were conducted on a nanocoated DI-CI engine, maintaining consistent operating conditions at the designated power output. These tests were conducted on a single day and in ecologically comparable environments. The main motive of this study is to improve the efficiency and reduce the NO_x and smoke emissions through minor modifications to the engine's characteristics. In contrast to the author's prior study, which employed the identical ternary blend without making any engine adjustments, the current study yielded reduced efficiency and increased smoke emissions when compared to synthetic diesel fuel.

OUTCOMES AND ANALYSIS

Combustion Analysis

Cylinder Pressure (CP)

CP is the peak pressure that may be achieved within the combustion zone, following the complete burning of the fuel. Figure 3 (a) shows the cylinder pressure of different fuel mixtures as the engine load increases. Because there are more fuel oxygen molecules in biodiesel, it burns more efficiently. This means that the pressure in the combustion chamber rises faster than with regular diesel. [32]. Moreover, the use of ethanol in biodiesel blends (E05 & E15) enhances cylinder pressure, especially evident at elevated engine loads. There are a lot of things that point to this conclusion. For example, ethanol has a higher autoignition temperature and more heat when it evaporates. Biodiesel has a higher pressure when mixed with ethanol in the cylinder, and it releases more heat than biodiesel. Biodiesel blends with ethanol perform better than biodiesel blends with diesel fuel when it comes to increasing cylinder pressure and rate of pressure [33].

Heat Release Rate (HRR)

The most crucial combustion factor in a diesel engine is the cylinder HRR. One definition of HRR is the quantity of heat that an energy source may generate in a given length of time. The pressure within the cylinder and the pace at which it is increasing to its peak are the two variables that affect the heat transfer rate. [34]. There were consistent trends with respect to crank angle in the biodiesel and diesel HRRs. Figure 3 (b) clearly shows that the biodiesel trajectory has moved to the left compared to the diesel trajectory. This means that combustion happens faster in biodiesel-diesel blends than in base diesel. An increase in HRR was noted when the ethanol % rose in comparison to blended fuel. This might be because of the faster heat release followed by better mixture preparation during the delay period. The highest peak of premixed combustion HRR is observed in the fuel that is blended with ethanol, suggesting that a greater percentage of the fuel is burnt during this phase [35].

Performance Characteristics

Brake thermal efficiency (BTE)

Figure 4 (a) depicts a different fuel blend that can perform differently in terms of BTE, Biodiesel and ethanol blend of B20E15 showed a 2-3% higher BTE than pure diesel under maximum load. The higher oxygen concentration in ethanol enhances the efficiency of combustion. As a result of the high ethanol content in the mix, the viscosity and combustion rate are lower; therefore the BTE is lower than B30E15. The density and viscosity of punnai biodiesel are higher than diesel, which causes the first combustion phase to be slower and the BTE to decrease compared to diesel [10]. The blend density is increased by high levels of latent heat and volatility from ethanol, which in turn improves the brakes' thermal efficiency as the ethanol proportion increases. The temperature of the air-fuel combination drops, as the amount of ethanol in the mixture rises, leading to better-premixed combustion, since the air temperature in the emulsion is lower and there is a longer time for the fire to start because of the lower temperature in the air [23]. As a result of the coating of ceramic acts as a heat shield separating the engine from its surroundings, the engine with partially stabilized zirconia coating has a low heat rejection and achieved a much enhanced thermal efficiency in comparison to the other engines based on the fact that the coating of ceramic acts as a heat shield. By reducing heat loss, it is possible to increase the power and thermal efficiency of an engine [20].

Specific Fuel Consumption (SFC)

Fuel injection increases as engine load rises, resulting in a higher SFC ratio. Figure 4 (b) shows the SFC with engine load and ethanol ratios, indicating that the SFC reduces as the engine load increases. There was a 3.8 % decrease in SFC for the B20E05 blend and a 16.3% decrease for the B20E15 blend when correlated to diesel, respectively. Fuel consumption was 9% higher with B30E15 blends correlated to diesel, however. Due to the lower calorific value of biodiesel blends and the higher density, biodiesel blends require more fuel to run an engine than conventional diesel. Increasing the biodiesel blend

ratio leads to higher fuel consumption since it decreases the fuel mixture's density and calorific value [24]. Study results indicate that the coating provides superior heat retention, which results in higher temperatures inside the cylinders. Temperature increases in the cylinder improve the biofuel mix's oxidation, which results in better atomization. Improved atomization and vaporization reduce the consumption of fuel while maintaining the speed of the engine [17].

Equivalence Ratio (λ)

The air-to-fuel equivalence ratio (λ) was measured at full engine power for different fuel mixtures, including pure Diesel (D100) and blends of Punnai biodiesel and ethanol. The engine operated at a compression ratio (CR) of 17.5:1, which is typical for CI engines [36]. At full load, the equivalence ratio (λ) indicates how lean or rich the air-fuel mixture is compared to the stoichiometric ideal, where a λ value greater than 1 denotes a lean mixture (excess air), and a value less than 1 indicates a rich mixture. Among all tested fuels, pure diesel exhibited the highest λ value of 1.724, indicating the leanest combustion. The B20E15 blend followed closely with a λ of 1.722, suggesting similarly efficient combustion. B20E05 and B30E05 showed slightly richer mixtures, with λ values of 1.664 and 1.674, respectively. B30E15 recorded the lowest λ value of 1.459, indicating the richest mixture among the samples. Overall, all fuel blends operated under lean conditions, with diesel and B20E15 demonstrating optimal air utilisation.

Emission Characteristics

Nitrogen oxide (NOx)

Nitrogen oxide (NO_x) emissions can be reduced by reducing the premixed burning rate while releasing heat at a slower rate. In ethanol biodiesel dual-fuel engines, NO_x emissions rise with the increase in ethanol's energy share. A number of factors influence NO_x generation [23]. The sudden rise in NO_x emissions was attributed to increased engine load in the presence of higher fuel consumption. As a result, NO_x emissions decreased [21]. It is shown in Figure 5 (a) that at full load circumstances, B20E05, B2015, B30E05, and B30E15 fuels show higher NO_x concentrations than diesel, at rates of 3.8%, 4.6%, 5.4%, and 13.9%, respectively. However, one aspect of the coated engine requires attention and a result has demonstrated that coated piston engines emit more NO_x than uncoated piston engines. It may also be that the temperature of the NO_x emissions is higher, thus resulting in an earlier ignition, which transfers pressure and temperature less efficiently. A coated piston engine emits more NO_x than a nanocoated piston engine. The higher temperature and pressure in the combustion process may cause the engine to emit more NO_x, resulting in higher emissions. The majority of biofuels are burned in the premixing phase before combustion, so NO_x levels are reduced during combustion [19].

Smoke Opacity (SO)

Figure 5 (b) shows a trend in smoke release to enhance the smoke reduction in engines involving two crucial elements: elevating the combustion chamber temperature and minimising heat transfer to the coolant. Due to the high combustion chamber temperature, nanocoating can enhance evaporation by increasing the proportion of premixed fuel in the chamber of combustion. Thus, the diffusion burn is lowered, which reduces the generation of smoke as a result [26]. At maximum load conditions, the smoke generation rates increase for the biodiesel and ethanol blends when correlating to diesel. The blends B20E05, B2015, B30E05, and B30E15 produces the smoke levels of 12%, 3.8%, 13.3%, 10%, and 14.9% higher than diesel, respectively. If the fuel is burned inefficiently, smoke is produced. A reduction in smoke emissions is also influenced by the reduction in latent heat of vaporization and the ignition delay that occurs with the increasing load of the engine [27]. The application of nanocoated on engine components results in an increased heat retention rate inside the cylinder, which is completely capable of burning the fuel. As a result, coated engines reduce their smoke emissions.

Carbon monoxide (CO)

Figure 5 (d) depicts the influence of different biodiesel mixes on the release of carbon monoxide (CO). At low loads, diesel emits less CO than biodiesel blends when full combustion occurs. As a result of chemical processes that allow CO production to be enhanced, biodiesel blends emit less CO, but more CO_2 as a result of greater oxygen content [28]. Compared with pure diesel, B20E05 and B20E15 blends reduce CO concentrations by 5.8% and 8.6%, respectively, whereas B30 blends increase the amount of CO emissions. Additionally, thermal barrier coatings on engines significantly decreased the amount of CO that was emitted, with coated engines emitting significantly less CO than uncoated engines. Thermal insulation that has been coated with nanoparticles is activated by combustion in the late phase and the oxidation of CO, which results in a reduction in CO concentrations as the speed of the combustion increases. As long as the engine operates at its optimal speed, CO emissions are almost negligible, indicating that CO emissions are substantially controlled independent of piston coating [29].

Hydrocarbon (HC)

Figure 5 (c) shows the hydrocarbon exhausts. The oxidation of atmospheric hydrocarbons with oxygen in ethanol improves fuel efficiency, reducing hydrocarbon (HC) emissions. The oxidation of hydrocarbons during combustion can be enhanced by ethanol, an alcohol with oxygen. Combined with biodiesel, ethanol can reduce HC emissions and increase fuel efficiency [7]. As a result of the higher combustion pressure and temperature caused by ethanol combustion, hydrocarbons are more completely oxidized. However, hydrogen lead combustion in diesel engines produces lower combustion pressure and temperatures, leading to lower oxidation of hydrocarbons and higher emissions of HC as a result of lower pressure as well as temperature during combustion [25]. According to the findings of the study, the hydrocarbon emissions of B20E05 and B20E15 blends were reduced by 2.5% and

8.6%, respectively, when compared to pure diesel. On the other hand, the hydrocarbon emissions of B30E15 blends were raised by 10% when compared to diesel. A thermal barrier layer was employed to raise combustion temperature in the study to improve fuel combustion. Because hydrocarbons break down faster than hydrogen and oxygen in the chamber of combustion, the thermal barrier layer reduces hydrocarbon emissions. Hydrocarbon emissions cause air pollution and threaten human health, thus reducing them is crucial. A heat barrier coating must be examined together with quenching distance and flammability threshold, which are safety factors. The study also shows how ethanol mixes affect fuel usage, carbon monoxide emissions, hydrocarbon emissions, and nitrogen oxide emissions [30].

The limitations of using biodiesel are listed below:

1. The accessibility and expense of biodiesel feedstocks can be affected by variables such as land accessibility.
2. Compared to oil-based diesel, biodiesel now has a limited production capacity.
3. Biodiesel may exhibit elevated cloud point and pour point temperatures relative to petroleum diesel, potentially impacting its flow and performance under cold weather situations. Incorporating petroleum diesel or other additives might mitigate this problem.
4. Biodiesel has worse oxidative stability compared to petroleum diesel, rendering it more susceptible to deterioration and sediment development over time.

Figure 2 Nanocoated piston mounted in the cylčinder head (left) and b) layout of test engine setup (right).

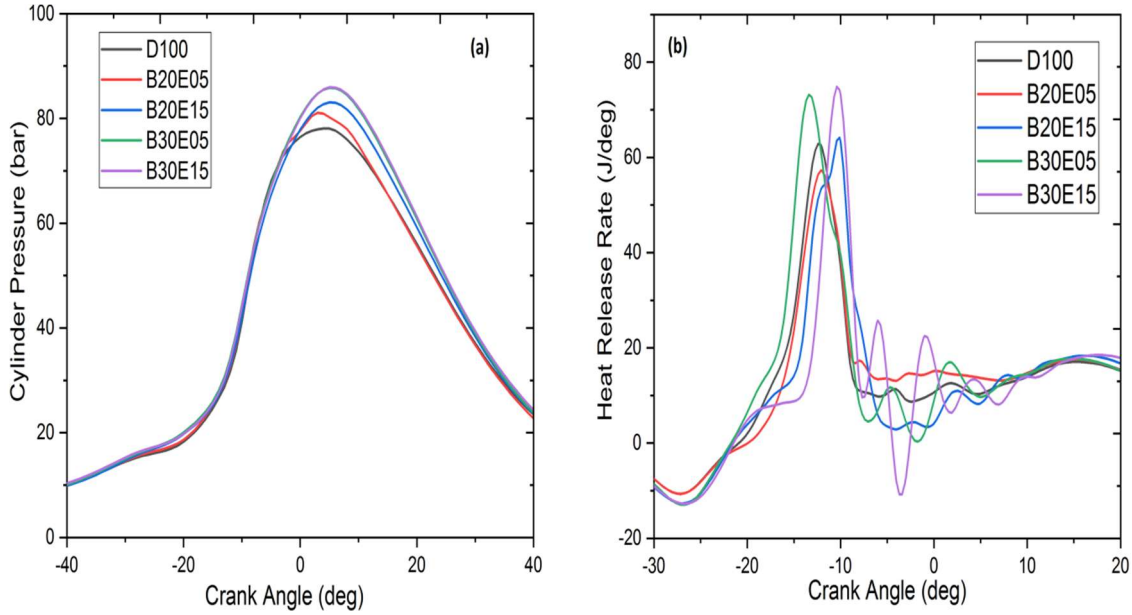

Figure 3 (a) Cylinder pressure and (b) heat release rate Vs crank angle at different load conditions.

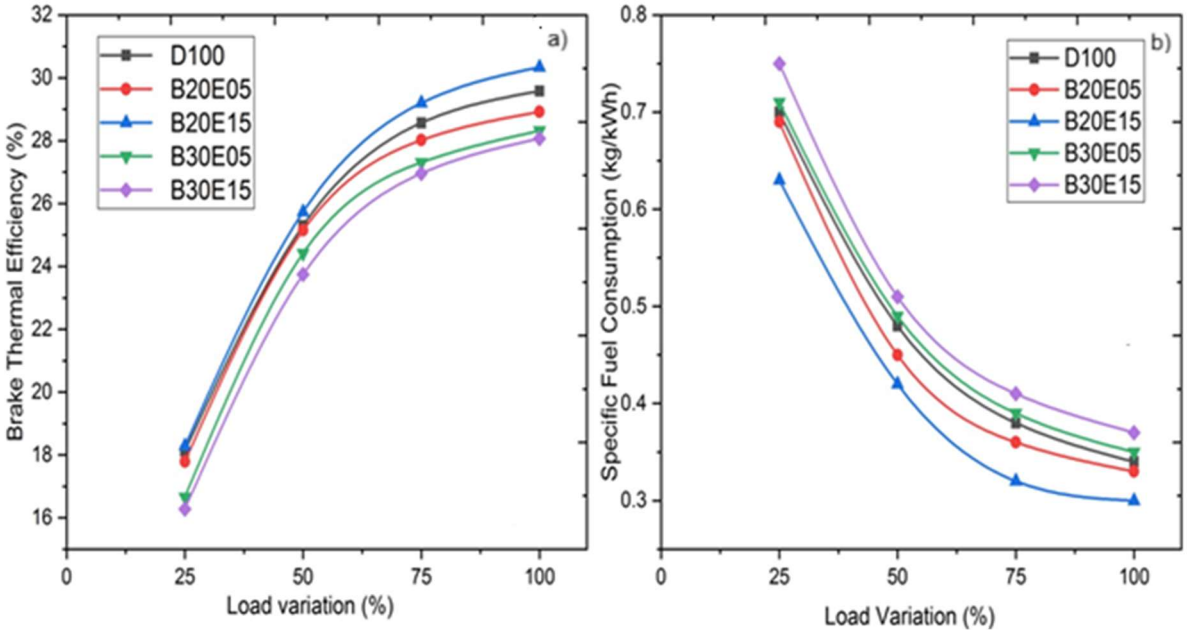

Figure 4 (a) BTE and (b) SFC Vs different load conditions

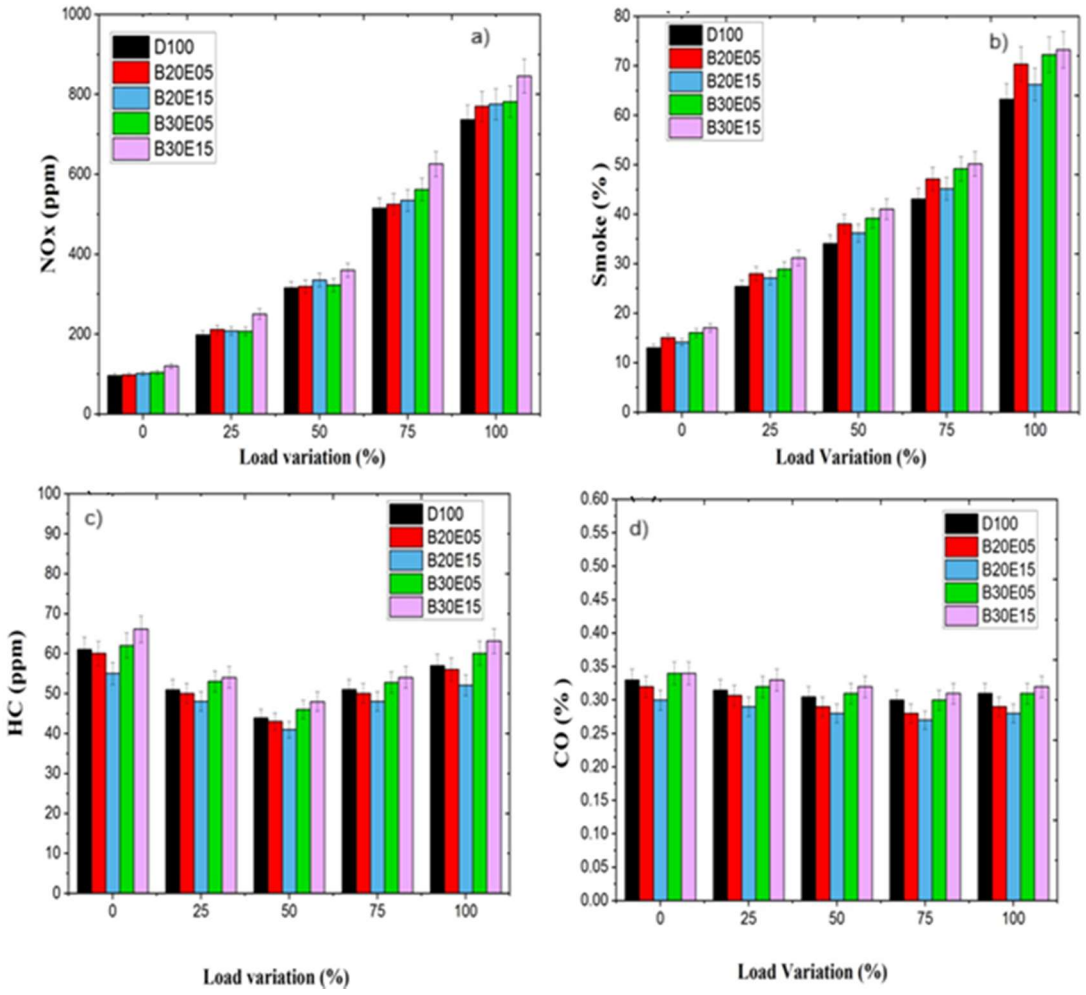

*Figure 5 (a) NOx, (b) Smoke, (c) HC, and (d) CO Vs different load conditions**

CONCLUSION

Emerging economies like India widely use diesel-powered vehicles to transport commodities and people. Traffic, fuel use, and environmental hazards rise. Plant-based biofuels, such as diesel, may solve these problems. This study aims to examine diesel engine performance with ethanol-biodiesel mixes generated from Punnai seed. A nanoparticle-covered single-cylinder diesel engine burnt biodiesel and ethanol in different proportions to optimise combustion.

- Ethanol-blended biodiesel (E05 and E15) increases cylinder pressure, particularly under high engine loads, owing to improved combustion efficiency and elevated heat release. These mixes surpass conventional diesel and biodiesel in enhancing cylinder pressure.
- The brake efficiency of engine B20E15 exhibits a 3% improvement compared to diesel. With regards to B20E05 and B20E15, ethanol contains a significantly higher concentration of oxygen compared to diesel.
- The comparison of the specific usage of these two fuel types reveals a reduction of approximately 3.8% and 16.3% in consumption of fuel, respectively.
- The combustion emissions of NO_x from the ideal B20E05 mixture exhibit an average reduction of 13.13% compared to the emissions seen in other test samples.
- The CO and HC emissions went down ranging from 5% and 9% with the B20 blends.
- Finally, operating at maximum load, the B20E15 exhibits optimal levels of CO and HC emissions, measuring 0.3% and 56 ppm, respectively. Additionally, it achieves a fuel consumption of 0.321 kg/kWh.

REFERENCES

[1] I. Veza, A.D. Karaoglan, E. Ileri, Case Stud. Therm. Eng. 31 (2022) 101817. https://doi.org/10.1016/j.csite.2022.101817.

[2] A.T. Hoang, S. Nižetić, H.C. Ong, W. Tarelko, V.V. Pham, T.H. Le, M.Q. Chau, X.P. Nguyen, Sustainable Energy Technol. Assess. 47 (2021) 101416. https://doi.org/10.1016/j.seta.2021.101416.

[3] B. Sharma, A. Shrestha, Energy Strategy. Rev. 45 (2023) 101053. https://doi.org/10.1016/j.esr.2023.101053.

[4] Y. Devarajan, R. Jayabal, D.B. Munuswamy, S. Ganesan, E.G. Varuvel, Process. Saf. Environ. Prot. 165 (2022) 374–439. https://doi.org/10.1016/j.psep.2022.07.001.

[5] M. Çelik, C.Bayındırlı, M.Mehregan, Environ. Sci. Pollut. Res. 29 (2022) 30277-30284. https://doi.org/10.1007/s11356-021-18012-1.

[6] M.N. Bin Mohiddin, Y.H. Tan, Y.X. Seow, J. Kansedo, N. Mubarak, M.O. Abdullah, Y.S. Chan, M.J. Khalid, Ind. Eng. Chem. 98 (2021) 60-81. https://doi.org/10.1016/j.jiec.2021.03.036.

[7] R. Sathyamurthy, D. Balaji, S. Gorjian, S.J. Muthiya, R. Bharathwaaj, S. Vasanthaseelan, Sustainable Energy Technol. Assess. 43 (2021) 100981. https://doi.org/10.1016/j.seta.2020.100981.

[8] P. Łagowski, G. Wcisło, D. Kurczyński, Energies 15 (2022) 6835. https://doi.org/10.3390/en15186835.

[9] Y. Devarajan, R.K. Jayabal, D. Ragupathy, H. Venu, Front. Environ. Sci. Eng. 11 (2017) 1-6. https://doi.org/10.1007/s11783-017-0891-0.

[10] B. Chidambaranathan, P. Seenikannan, P. Seenikannan. J. Therm. Sci. 24 (2020) 13-25. https://doi.org/10.2298/TSCI180325233B.

[11] K. Subramanian, S.A. Paramasivam, D. Dillikannan, M. Muthu, P.R. Yadav Sanjeevi, Int. J. Ambient Energy (2022) 1-14. https://doi.org/10.1080/01430750.2022.2103184.

[12] F. Hamdi, I. Yahya, M. Gassoumi, Z. Boutar, R.M.R. Ahsan Shah, M. Al. Qubeissi, R.Ennetta, H. S. Soyhan. Sci. Tech. Energ. Transition, 33 (2024). https://doi.org/10.2516/stet/2024033.

[13] S.Dey, A.P.Singh, S.S. Gajghate, S.Pal, B.B .Saha, M. Deb, P.K. Das. Sustainability. (2023) 5(20):14667. https://doi.org/10.3390/su152014667.

[14] M. Nagappan & J. M. Babu. Mater. Today: Proc., (2023) https://doi.org/10.1016/j.matpr.2023.01.122.

[15] L. Urtekin, S. Bayaşoğlu, Surf. Rev. Lett. 27 (2020) 1950158. https://doi.org/10.1142/S0218625X19501580.

[16] D. Sakthivadivel, P.G. Kumar, R. Prabakaran, V. Vigneswaran, K. Nithyanandhan, S.C. Kim, Case Stud. Therm. Eng. 34 (2022) 102021. https://doi.org/10.1016/j.csite.2022.102021.

[17] M. Tomar, N. Kumar, Energy Sources, Part A (2019) 1-18. https://doi.org/10.1080/15567036.2019.1623347.

[18] P. Kumaran, S. Natarajan, IOP Conf. Ser.: Mater. Sci. Eng. 993 (2020) 012014. https://iopscience.iop.org/article/10.1088/1757-899X/993/1/012014/pdf.

[19] M.M. Musthafa, Int. J. Sustainable Energy Eng. 11 (2018) 159–166. https://doi.org/10.1080/19397038.2017.1393024.

[20] M. Selvam, S. Shanmugan, S. Palani, Environ. Sci. Pollut. Res. 25 (2018) 35210-35220. https://doi.org/10.1007/s11356-018-3419-7.

[21] P. Balu, P. Saravanan, V. Jayaseelan, Mater. Today: Proc. 39 (2021) 1259–1264. https://doi.org/10.1016/j.matpr.2020.04.160.

[22] V. Dananjayakumar, M.B. Sanjeevannavar, S.M. Golabhanvi, M.A. Kamoji, Mater. Today: Proc. 42 (2021) 1387-1392. https://doi.org/10.1016/j.matpr.2021.01.113.

[23] A.M. Narad, M.P. Joshi, Results Mater. 8 (2020) 100140. https://doi.org/10.1016/j.rinma.2020.100140.

[24] L. Geng, L. Bi, Q. Li, H. Chen, Y. Xie, Energy Rep. 7 (2021) 904-915. https://doi.org/10.1016/j.egyr.2021.01.043.

[25] S.B. Sai, N. Subramaniapillai, M.S.B. Khadhar Mohamed, A. Narayanan, Fuel 296 (2021) 120708. https://doi.org/10.1016/j.fuel.2021.120708.

[26] V.E. Geo, A. Sonthalia, G. Nagarajan, B. Nagalingam, Fuel 209 (2017) 733-741. https://doi.org/10.1016/j.fuel.2017.08.036.

[27] J. Kumaraswamy, V. Kumar, G. Purushotham, R. Suresh, J. Therm. Eng. 7 (2021) 415-428. https://doi.org/10.18186/thermal.882965.
[28] S.R.K. Valiveti, H. Shaik, K.V.K. Reddy, Int. J. Ambient Energy (2020) 1-18. https://doi.org/10.1080/01430750.2020.1831592.
[29] K. Sudalaiyandi, K. Alagar, R. Vignesh Kumar, V.J. Manoj Praveen, P. Madhu, Fuel 285 (2021) 119255. https://doi.org/10.1016/j.fuel.2020.119255.
[30] N. Ramasamy, M.A. Kalam, M. Varman, Y.H. Teoh, Coatings 11 (2021) 692. http://eprints.um.edu.my/id/eprint/26425.
[31] S. Padmanabhan, C. Joel, L. Joel, O.Y. Reddy, K.G.D.S. Harsha, S. Ganesan, Nat. Environ. Pollut. Technol. 20 (2021) 2079-2086. https://doi.org/10.46488/NEPT.2021.v20i05.025.
[32] A. Naresh Kumar, P.S. Kishore, K. Brahma Raju, K. Nanthagopal, B. Ashok, Fuel 276 (2020) 118076. https://doi.org/10.1016/j.fuel.2020.118076.
[33] D. Balasubramanian, A.T. Hoang, I.P. Venugopal, A. Shanmugam, J. Gao, T. Wongwuttanasatian, Fuel 287 (2020) 119815. https://doi.org/10.1016/j.fuel.2020.119815.
[34] K.R. Kavitha, J. Jayaprabakar, A. Prabhu, Int. J. Ambient Energy 43 (2019) 778-782. https://doi.org/10.1080/01430750.2019.1670261.
[35] A.F. Emma, S. Alangar, A.K. Yadav, Energy Convers. Manage: X 14 (2022) 100214. https://doi.org/10.1016/j.ecmx.2022.100214.
[36] S. Rajendran, M. Govindasamy, Energy Sources, Part A (2021) 1-16. https://doi.org/10.1080/15567036.2021.1887408.
[37] R. Shanmugam, D. Dillikannan, G. Kaliyaperumal, M.V. De Poures, R.K. Babu, Energy Sources, Part A (2020) 43 (2020) 3064-3081. https://doi.org/10.1080/15567036.2020.1833112.
[38] K. Subramanian, S.A. Paramasivam, D. Dillikannan. J. Ravikumar, Sustainable Energy Technol. Assess. 58 (2023) 103345. https://doi.org/10.1016/j.seta.2023.103345.

SRINIVASAN KASINATHAN NARENDRANATHAN[1]

KARTHIKEYAN SUBRAMANIAN[2]

PURUSHOTHAMAN PANNEERSELVAM[1]

SRINIVASAN TIRUPATHI[2]

[1]Department of Mechanical Engineering, Agni College of Technology, Tamil Nadu, India.

[2]Department of Mechatronics Engineering, Agni College of Technology, Tamil Nadu, India

NAUČNI RAD

ANALIZA EFIKASNOSTI I IZDUVNIH GASOVA MEŠAVINA PUNAI BIODIZEL-ETANOL U NANO OBLOŽENIM MOTORIMA SA KOMPRESIONIM PALJENJEM

U ovom radu su eksperimentalno istraživane performanse, emisije i karakteristike sagorevanja nanoprevučenog motora sa kompresionim paljenjem koji koristi mešavine Punai biodizela sa etanolom z različitim odnosima. Nano-premaz je nanesen na košuljicu cilindra i glavu klipa motora kako bi se poboljšao prenos toplote i smanjilo trenje. Mešavine su pripremljene mešanjem Punai ulja sa dizel gorivom u različitim odnosima (B20 i B30). Etanol je dodat svakoj mešavini u koncentracijama od 5% i 15%. Cilj istraživanja je bio da se poboljša operativna efikasnost motora koji koristi dizel, korišćenjem klipa presvučenog termičkom barijerom, posebno prilagođenom za mešavine Punai metil-estara. Termički barijerne premazi imaju prednost nad cirkonijumom zbog njihovih izuzetnih svojstava toplotne izolacije. B20E15 ima termičku efikasnost kočenja koja je veća od dizela za oko 3%. Slično tome, B20E05 i B20E15 pokazuju smanjenje potrošnje goriva od približno 3,8% i 16,3%, respektivno. U proseku, mešavine B20 pokazale su smanjenje emisije CO i HC od 5% i 9%. Uporedna analiza je jasno pokazala da nano-prevučeni motori sa kompresionim paljenjem poboljšavaju performanse i smanjuju emisije bez ikakvih većih modifikacija.

Ključne reči: Punnai biodizel, etanol, nano-prevlaka, dizel motor, efikasnost, izduvni gasovi.

CI&CEQ
Chemical Industry & Chemical Engineering Quarterly

Available online at
Association of the Chemical Engineers of Serbia AChE
www.ache.org.rs/CICEQ

Chem. Ind. Chem. Eng. Q. 32 (2) 123–131 (2026) CI&CEQ

ZOHRA MECABIH

Department of Chemistry, Faculty of Exact Sciences,

Djillali Liabes University

Sidi Bel Abbes, Algeria.

REMOVAL OF ISOPROPYL ALCOHOL FROM WASTEWATER USING MODIFIED BENTONITE BY Fe, Cu, AND Fe-Cu

Highlights

- Catalysts based on pillared clays with Fe, Cu, and Fe-Cu were utilized.
- IPA is one of the most common pollutants in semiconductor manufacturing wastewater.
- Using catalytic wet peroxide oxidation processes for the removal of IPA.

Abstract

Catalysts based on purified bentonite (Be) pillared with Fe^{3+} (BeFe), Cu^{2+} (BeCu), and Fe-Cu (BeFe/Cu) were synthesized from Algerian bentonite and used to treat isopropyl alcohol (IPA) by catalytic wet peroxide oxidation (CWPO) with H_2O_2 at 298 K. The BeFe showed higher activity than the BeFe/Cu one for IPA removal, although the second was more active for H_2O_2 decomposition. The reaction kinetics were examined with both catalysts using the pseudo-first-order reaction model. The mechanism of H_2O_2 decomposition was known through different values of apparent activation energy (Ea) were determined from the Arrhenius equation 46 kJ/mol for BeFe with abundant formation of •OH radicals and 67 kJ/mol for BeFe/Cu with mainly production of O_2 which has a low oxidation capacity at 298 K.

Keywords: Isopropyl alcohol oxidation; Pillared clays; Cu; Fe; Fe-Cu.

SCIENTIFIC PAPER

UDC 628.3:666.322:66.094.3

INTRODUCTION

Isopropyl alcohol (IPA) is commonly used as an organic solvent such as a cleaning agent for silicon wafers [1] and a drying agent for removing residual organic matter on the water surface in the semiconductor industry [2]. This industry is a significant water consumer and producer of wastewater, which can be hazardous to the environment if not treated properly. The resulting wastewater is characterized as highly turbid due to its high solid content, high chemical oxygen demand (COD) (normally ranging between 3000 and 5000 mg/L), and major contamination from organic and inorganic solvent particles ranging from nano to micro-sized [3]. These organic compounds pose direct or indirect harm to the liver, kidney, central nervous system, and skin, and some of them have already been verified as carcinogens, teratogenic agents, and genetic mutagen for humans. Traditional wastewater treatment approaches involving physical-chemical decomposition or microorganisms have shown only limited efficiencies [4]. Therefore, the wastewater is generally treated using the activated sludge method. However, this method has problems such as a long treatment time, the necessity of pre-treatment and post-treatment, and the generation of excess sludge. Therefore, a wastewater treatment technique with a short time and less environmental load is required. Currently, advanced oxidation processes (AOPs) are commonly used to oxide complex organic contaminants that are found in wastewater and that are difficult to degrade into simpler end products through biological processes [5]. Catalytic wet peroxide oxidation (CWPO) is one of these successful AOPs, utilizing steady catalysis for the reduction of pollutants in industrial wastewater in the presence of an active catalyst [6]. AOPs are characterized by the production of •OH radicals [7], which are potent (2.8 V) and unselective oxidants that can oxidize and mineralize organic pollutants in water, yielding CO_2 and other inorganic compounds [8]. Hydroxyl radicals can be generated from H_2O_2 by using activated carbon and Fenton's reagent, among other decomposition catalysts. Fenton's reagent utilizes Fe ions as a homogeneous catalyst, producing hydroxyl and perhydroxyl radicals from water [9]:

Correspondence: Z. Mecabih, Department of Chemistry, Faculty of Exact Sciences, Djillali Liabes University Hai Larbi ben M'hidi Pb.89, 22000 Sidi Bel Abbes, Algeria,
Email: zmecabih@gmail.com
Paper received: 27 December, 2024
Paper revised: 30 May, 2025
Paper accepted: 16 June, 2025

https://doi.org/10.2298/CICEQ241227016M

$$Fe^{3+} + H_2O_2 \rightarrow Fe^{2+} + H^+ + HOO^{\cdot} \quad (1)$$

$$Fe^{2+} + H_2O_2 \rightarrow Fe^{3+} + HO^- + HO^{\cdot} \quad (2)$$

AOPs can also be carried out under heterogeneous conditions by immobilizing the iron catalyst on a support such as zeolite [10], MnOx [11], carbon material [12], and polymers [13]. Bentonite is natural clay abundantly available with good exchanging ability and unique physical and chemical properties. Modified bentonite (Be) is of great importance in the preparation of some high-technology materials such as pillared clays (PILCs). PILCs have received increasing interest in the last 2 decades as green heterogeneous catalysts in wastewater treatment due to their textural and catalytic properties in different reactions [14]. They represent a new class of microporous materials that have potential applications as catalysts [15]. In principle, any metal oxide or salt-forming polynuclear species upon hydrolysis can be inserted as a pillar [16]. The hydroxyl polycations of polynuclear metals are commonly used as pillaring agents in bentonite to modify its structures such as Al, Fe, Cu, Zr, Cr, Ce, and Ti individually or mixed, yielding PILC materials with thermal and mechanical stability [16,17], On the other hand, as indicated before, iron is the metallic ion used in Fenton's reagent. Thus, the intercalation of cations Cu-Fe, in the interlayer spacing of Be, should produce catalytically active materials for the oxidation of organic compounds with hydrogen peroxide. Be-(Cu, Fe, Al, and Cr) are the most studied, as they have been proposed as active catalysts for the oxidation of organic compounds [18–19]. Some advantages of BeFe in AOPs are their stability, their capacity to work with pH values in a range of 3–3.5, and where leaching of Fe ions is minimal [18]. Cu as oxide is a Lewis acid that has very advantageous photocatalytic properties. It is a non-toxic material, is very stable over long periods, is environmentally friendly, and has strong light absorption [18]. The use of BeCu as a catalyst of the AOPs has been mainly studied without the use of light [19]. BeFe/Cu was used in the mineralization of paracetamol by AOPs under neutral pH conditions, obtaining about 80% mineralization; this result was only 2% less than the degree of mineralization achieved at acidic pH after 180 min of the reaction [20]. The use of BeCu as a catalyst for AOPs has been studied mainly without the use of light [19,21], and some have reported its effectiveness in phenol mineralization. In some studies, Cu was added to the pre-prepared BeFeAl; the addition of Cu enhanced the oxidation of organic compounds, which was attributed to the synergy between Cu and Fe [20,22]. It has been concluded [23] that in addition to the typical Fenton reaction (Eq. (2)), other species might be appearing, like the reactive intermediate $\equiv Cu^{2+}-OH^-$ that contribute to organic compound degradation. It has also been recently demonstrated that Cu+ activates oxygen to produce powerful reactive oxygen species (H_2O_2, O_2- and •OH) [23]. Despite the extensive literature reported about the removal of IPA by CWPO using microwave [24], catalysts, such as ZrO_2 [25], $Pt/Al6Si_2O_{13}$ [26], Mo/V [27], ZnO [28], and NaX-zeolite [29,30], and by adsorption on activated bentonite [31], to the best of our knowledge, there is no work where Be-(Fe, Cu, Fe/Cu) is used as catalysts for this reaction. The present investigation deals with the study of the removal of IPA from wastewater by CWPO using BeFe, BeCu, and BeFe/Cu catalysts, and the decomposition of H_2O_2 was also discussed.

MATERIALS AND METHODS

Preparation of catalyst

All substances used in this study were highly purified (> 99%), mostly Fluka AG, Buchs SG, and ultrapure water.

The raw from Maghnia (western Algeria), supplied by Bental Company, Algeria, was purified and classified by sedimentation, and then the <2 μm fraction was collected for the pillaring experiment. The cation exchange capacity (CEC) was 98 meq/100 g of clay determinate by copper ethylenediamine ($(EDA)_2CuCl_2$) complex.

A Be powder (4 g) was put with 1 g of $FeCl_3$, $CuCl_2$, and a Fe/Cu mix (50/50% mass ratio) in a Morton press to mix the mixture well. Afterward, 1 M NaOH solution was added by 0.0625 mass ratio (OH/M, M = Fe^{3+}, Cu^{2+}) in a dropwise manner in this mixed powder to make a suspension. It rested for 24 h until a suitable paste was obtained. Further, very small beads were formed from the dough, which were calcined at 500 °C for 2 h. Be with Fe, Cu, and Fe/Cu were named by BeFe, BeCu, and BeFe/Cu, respectively.

Characterization methods

The surface morphology and elemental composition of the samples were observed by a scanning electron microscope (SEM) with an energy-dispersive X-ray spectroscopy (EDS) using the JEOL5510 model. The range of accelerating voltage was from 200 V to 30 kV with a resolution of 2 mm and magnification up to 5000×. The powder X-ray diffraction (PXRD) patterns were taken on a Philips P3710 X-ray diffractometer equipped with CuKα radiation (λ = 0.154 nm) at 40 mA and a scan rate of 0.039° (2θ)/900 s. Brunauer-Emmett-Teller (BET) surface area values were determined from 77 K N_2 adsorption using a Quantachrome Quadrasorb SI surface analyzer. The samples were previously outgassed at 363 K and 10^{-7} T for 16 h.

CWPO experiments

The maximum legal IPA concentration in wastewater effluent had not been established, so, to simulate the real situation in CWPO experiments, 10–200 ppm was used. The catalytic activity experiments for CWPO of IPA with the different catalysts were performed in a 500 mL three-necked round-bottom flask equipped with a mechanical stirrer. The pH was continuously controlled within the range of 3–3.5, which has been reported as optimal for AOP processes [18,20], as well as for CWPO with BeFe catalysts. After stabilization of the temperature at 298 K, the desired amount of Be was added to 125 mL of an aqueous IPA solution (10, 100, and 200 ppm) and it was stirred for 15 min to allow IPA adsorption onto the catalyst. The amount adsorbed was always less than 7% of the initial IPA weight. Next, add 125 mL of an aqueous H_2O_2 solution (10, 20, and 30 ppm) corresponds to the stoichiometric amount for complete oxidation of IPA. Samples from the reaction medium were withdrawn at the initial time and after 15 min, 30 min, and each hour until completing 4 h of reaction. The catalyst in these samples was removed using a nylon filter of 0.2 μm pore size. The oxidation process was followed by the evolution of total organic carbon (TOC), IPA, and H_2O_2 concentrations.

IPA was analyzed by gas chromatography-mass spectrometry (single quadrupole: Thermo Scientific). The H_2O_2 concentration was determined by a colorimetric titration method based on the formation the formation the yellow color of complex Ti(IV)-H_2O_2, using a UV-vis spectrophotometer at 410 nm. TOC was determined with a 5050-analyzer model. Since the stability of a catalyst is essential for the evaluation of its performance, a colorimetric method was used for the leaching of Fe^{3+} and Cu^{2+}.

Catalytic H_2O_2 decomposition experiments

Experiments were carried out to study the decomposition of H_2O_2 using a catalyst. Certain amounts of the catalysts were placed in glass bottles (25 mL). The catalysts were used in powder form to avoid diffusion limitations [18]. These flasks were deposited into a thermostatic bath and were magnetically stirred during the experiment. For each flask, a 100 ppm H_2O_2 solution was added quickly and the time was recorded. After a given time, an aliquot volume (2 µL) was taken from the flask, and the catalyst was removed employing a nylon filter of 0.2 µm pore size. Analyses of H_2O_2 were performed according to the above-described method [32].

RESULTS AND DISCUSSION

Characterization of the pillared clays

The variations in the chemical composition of catalysts, obtained by SEM-EDS are shown in Table 1. The results revealed an increment in the amount of Fe content in BeFe (8.76 wt%) and BeFe/Cu (9.15 wt%) as compared to Be (3.84 wt%). In Be, the Cu content was 0.13 wt% and increased to 6.53 wt% in BeFe/Cu and to 7.40 wt% in BeCu. The increase in wt% of Fe and Cu in BeFe, BeCu, and BeFe/Cu implied that Fe and Cu had been intercalated onto Be. Also, the Na content decreased after pillaring the Be with Fe and Cu ions (Table 1) due to the formation of FeO and CuO pillars between the silicate layers. Figure 1 shows the SEM images and EDX specters of Be (Figure 1 (a)), BeFe (Figure 1 (b)), BeCu (Figure 1 (c)), and BeFe/Cu (Figure 1 (d)). All samples exhibited heterogeneous surface morphology of Be surface, characterized by smooth (Figure 1(a)) and rough particles that tended to agglomerate with different sizes and irregular shapes, becoming rougher and more wrinkled ((Figure 1 (b), Figure 1 (c), and Figure 1 (d)) after the pillaring process. This difference may indicate that the oxide columns were stabilized due to the introduction of massive cations into the spaces between the clay layers. Peaks from the major elements Si, Al, and O are clearly observed in the EDX spectra of all samples (Figure 1). which were the most common chemical elements in the composition of bentonite compounds Figure 1(a). Fe (Figure 1 (b)), Cu (Figure 1 (c)), and Fe/Cu (Figure 1 (d)) were also determined, confirming the success and stability of the oxide pillared as a result of the introduction of massive cations into the spaces between the clay layers. The oriented powder X-ray diffractograms of Be and the resultant BeFe, BeCu, and Be/FeCu samples are shown in Figure 2 and Table 2 reports the basal spacing $d_{(001)}$ and the surface area values of the Be and pillared Be after calcination at 773 K. As observed from Figure 2 and Table 2, for the starting (Be), the (001) smectite peak occurred at $2\theta = 7.83°$ corresponding to a basal spacing of 11.3 Å. The d_{001} value of Be up to higher values in the range of 17.47 Å, 16.84 Å, and 15.73 Å for BeFe, BeFe/Cu, and BeCu, respectively, indicating that the modification carried out over the clay leads, in all the cases, to the successful pillaring of the material. It points out the stabilization of oxide pillars due to the introduction of bulky cations into the interlayer spaces of clay that prevents its silicate layers from closing on heating [18]. N_2-adsorption/desorption isotherms for Be, BFe, BeCu, and BeFe/Cu were obtained (Figure 3). All samples showed typical type-IV sorption isotherms, classified by IUPAC, and both showed an H3-type hysteresis loop at 0.45–0.99, indicating the mesoporosity of the materials. As can be seen from Table 2, the pillaring process substantially increases both the basal spacing and BET surface area. It can be seen that the surface area increased from 99 m^2/g for Be to 278 m^2/g for BeFe but the introduction of the Cu onto BeFe reduces the surface area that is due to the blocking of part of the catalyst pores.

Catalytic oxidation of IPA with pillared clays

Figure 4 shows the results obtained for IPA conversion, H_2O_2 decomposition, and TOC reduction in 10 ppm IPA, 1 g catalyst, and 20 ppm of H_2O_2 condition. It is clear that the pillared clay by Fe greatly increases their activity for the oxidation of IPA. Figure 4(a) shows a decrease in TOC removal, which is in all cases significantly lower than IPA conversion; this means that oxidation of IPA proceeds through the formation of different intermediates and the final result is far from complete mineralization, i.e., oxidation to $CO_2 + H_2O$.

Table 1. Chemical composition of catalysts by EDX.

Catalysts	Elemental composition (%)											
	OK	MgK	NaK	AlK	SiK	FeK	CuK	KK	CaK	TiK	LaL	Toal
Be	56.27	1.28	2.46	8.94	24.42	3.84	0.13	1.03	0.46	0.21	0.96	100.00
BeFe	53.72	2.01	1.04	12.51	18.24	8.76	0.21	1.76	0.16	1.19	0.40	100.00
BeF/Cu	53.15	0.23	0.02	12.51	18.07	9.15	6.53	0.13	0.18	0.01	0.02	100.00
BeCu	52.47	2.65	1.88	9.01	24.21	0.11	7.40	1.44	0.28	0.38	0.17	100.00

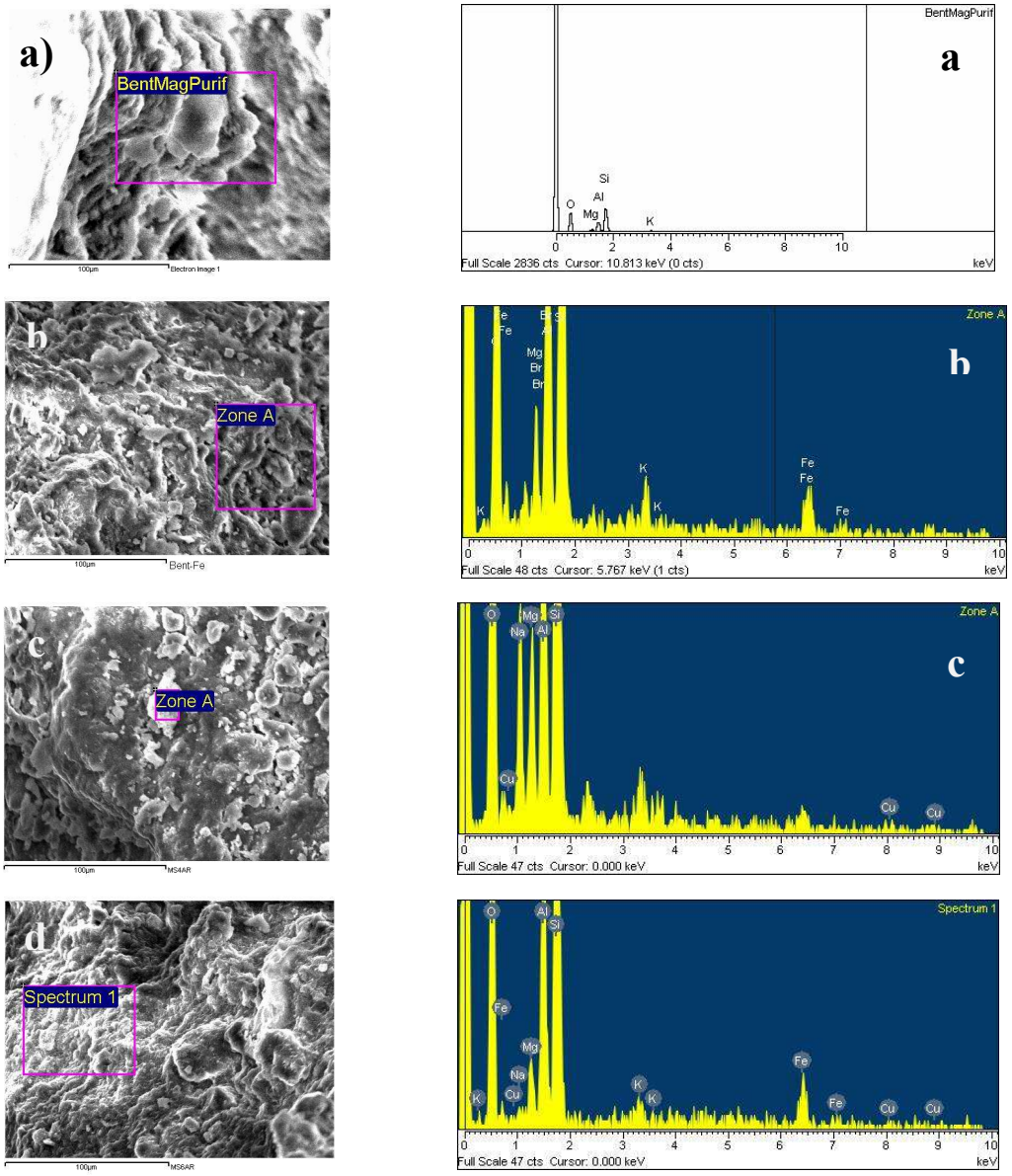

Figure 1. SEM images and EDX specters of catalysts.

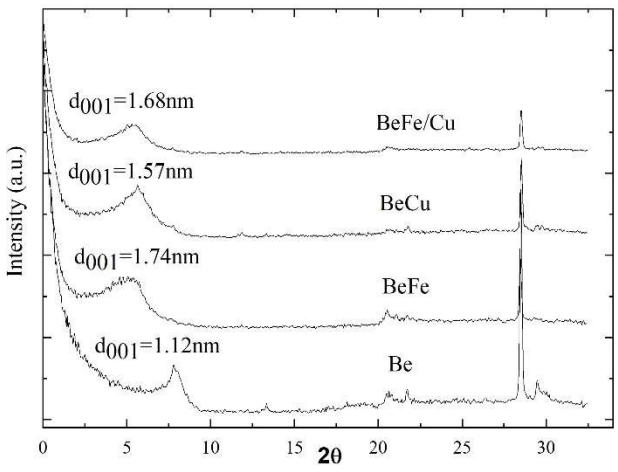

Figure 2. X-ray diffractograms of catalysts.

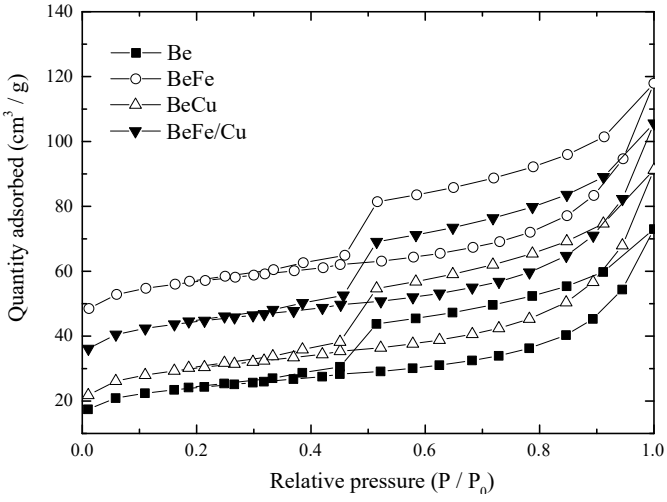

Figure 1. N_2-adsorption/desorption isotherms of catalysts

Table 1. Basal spacing (d001) and BET surface area values of catalysts.

	2θ (°)	d_{001} (nm)	S_{BET} (m^2/g)
Be	7.83	1.13	99
BeFe	5.07	1.74	278
BeFe/Cu	5.29	1.67	204
BeCu	5.67	1.56	136

The maximum TOC decrease after 3 h reaches 68% and close to 57% for both BeFe and BeFe/Cu, respectively, which means that significant amounts of intermediates remain in solution even at high reaction times. However, as Figure 4(a) shows, the presence of catalysts significantly enhances the oxidation rate of IPA compared to their absence. With BeFe, the IPA is almost completely removed (99%) in 60 min and the BeFe/Cu to 90% whereas BeCu leads to no more than 82% in the same time and complete removal requires more than 3 h of the reaction. Previous studies [18] have shown that, under acidic conditions, copper's catalytic activity is lower than iron's. As shown in Figure 4(b), the rate of H_2O_2 decomposition appears fairly similar for both BeFe and BeFe/Cu during the first 60 min of the reaction. This suggests that a different decomposition route is prevailing in both cases whereas BeFe promotes mainly the generation of OH radicals. Table 3 shows the effect of IPA removal of varying the H_2O_2 concentration on oxidation using the three catalysts for 1 h of the reaction. The oxidation rate increased as the amounts of H_2O_2 increased up to 20 ppm, indicating that the amount of •OH radicals generated by the catalyst was sufficient to degrade 10 ppm of IPA. The removal efficiency of IPA decreased with increasing concentration from (100 to 200 ppm) despite increasing H_2O_2 concentration. Because •OH generation is reduced under high IPA concentration due to blocking of catalyst active site by IPA molecules and prevents the H_2O_2 catalysis. When the H_2O_2 concentration exceeded 20 ppm, the removal of IPA decreased because of the well-known scavenging effect of •OH radicals [18,23]:

$$H_2O_2 + HO^{\cdot} \longrightarrow H_2O + H_2O^{\cdot} \quad (3)$$

$$HO^{\cdot} + H_2O^{\cdot} \longrightarrow O_2 + H_2O \quad (4)$$

Reaction (3) reduces the probability of attack by •OH radicals on organic molecules, causing the oxidation rate to fall. Although other radicals (e.g.,•OH_2) are also produced, that were generated in reaction (3), their oxidation potential is much lower than that of •OH species impairing the removal of organic compounds [18, 24]. But •OH_2 can have an additional scavenging effect on the •OH (reaction (4)) and thus the production of O_2. Thus, in subsequent experiments, 20 ppm of H_2O_2 was used in all the experiments.

Effects of the reaction temperature

To analyze this more in deep, the effects of the reaction temperature in the range of 298-323 K on the catalytic oxidation of IPA were investigated. Figure 5 shows the effects of reaction temperature for the catalytic oxidation of IPA with 20 ppm H_2O_2 and 1 g of the three catalysts. Also,

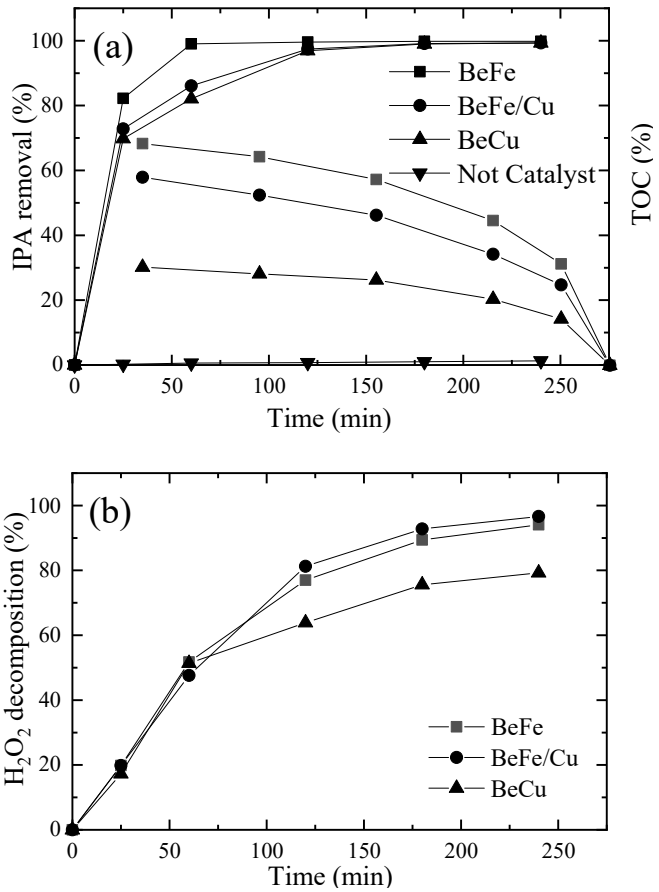

Figure 2. Results obtained in CWPO of IPA (10 ppm IPA, 1g of catalyst, 20 ppm of H2O2) by pillared clays.

Table 2. % Removal of IPA with catalysts before and after H_2O_2 addition.

H_2O_2 Conc.(ppm)	IPA Conc.(ppm)	IPA removal (%)		
		Pillared clay		
		BeFe	BeCu	BeFe/Cu
10	200	10.74	10.11	12.52
20		30.36	29.78	44.75
30		17.23	14.13	16.79
10	100	11.14	10.07	17.64
20		55.01	51.19	70.37
30		40.36	38.36	52.36
10	10	30.98	28.32	40.52
20		90.16	83.18	99.02
30		57.83	50.69	69.72

the TOC removal increases with the reaction temperature. After 3 h, at 323 K the TOC removal was more than 99.3% of all three samples whereas it was constant for a long time at low reaction temperatures of 298-313 K. This was because acetone and acetic acid were produced via the oxidation of IPA and C-C bond cleavage. Therefore, the low

rate of TOC oxidation decomposition is due to the formation of acetone, which contains the same amount of carbon as IPA and acetic acid is stable [24]. The kinetics of TOC decomposition with each of these three catalysts were studied to obtain the corresponding values of the apparent activation energy (Ea). For the leaching test, five consecutive IPA oxidation tests were performed with BeFe and BeFe/Cu catalysts. As can be seen in Figure 6, the leaching amount of metal oxides Fe^{3+} and Cu^{2+} were lower than 0.22 mg/L for Fe^{3+} in the case of BeFe and BeFe/Cu and 0.12 mg/L for Cu^{2+} in the case of BeFe/Cu after five times catalysts reuse, which can be neglected and this indicates the successful production of a stable catalyst characterized by a strong interaction between the metal oxides and PILC catalyst surfaces, and its suitability for continuous operation. Thus, it cannot explain the differences observed in the activity of both catalysts.

H_2O_2 decomposition

The kinetics of H_2O_2 decomposition with BeFe and BeFe/Cu catalysts to obtain the corresponding values of the apparent activation energy was studied. An initial H_2O_2 concentration of 200 ppm (5.67 mmol/L) with 1g/L of catalysts was used for H_2O_2 decomposition in the absence of IPA at different temperatures within the 298-323 K temperature range. Figure 7 shows the results obtained which, the rate of decomposition is significantly higher with the BeFe/Cu catalyst. It was found that the rate of decomposition of H_2O_2 increases with the increase in temperature, and significantly higher with the BeFe/Cu catalyst (Figure 7(a)). Additionally, the results reveal that the decomposition of H_2O_2 follows pseudo-first-order (PFO) kinetics [33,34]:

$$-\frac{d[H_2O_2]}{dt} = k_{app}[H_2O_2] \quad (5)$$

$$Ln\left(\frac{[H_2O_2]}{[H_2O_2]0}\right) = -k_{app}t \quad (6)$$

where k_{app} is the apparent first-order rate constant, and $[H_2O_2]$ and $[H_2O_2]_0$ are the concentrations of H_2O_2 in the solution at any time t and time zero, respectively. The experimental values of H_2O_2 concentration versus time were fitted and demonstrated to be a good fit to the first-order reaction with the lines shown in Figure 7b to the data by linear regression, resulting in correlation coefficients >0.990.

The temperature dependence of the reaction rate constants was expressed by the Arrhenius equation:

$$k = A\ exp\left(-\frac{E_a}{RT}\right) \quad (7)$$

where A is the frequency factor (s^{-1}), E_a is the activation energy (J/mol), R is the universal gas constant (J/(mol K), and T is the reaction temperature (K).

The E_a is calculated by using the following equation:

$$\ln k = -\frac{E_a}{RT} + \ln A \quad (8)$$

The Arrhenius plot of the apparent kinetic constant values is presented in Figure 8. The different prevailing mechanisms of H_2O_2 decomposition mentioned above can be explained by the difference in apparent E_a values of BeFe and BeFe/Cu. The corresponding values of the E_a were 46 and 67 kJ/mol for BeFe and BeFe/Cu, respectively. As indicated in the section on the effects of reaction temperature, E_a for BeFeCu was calculated using the Arrhenius equation, which found 109 kJ/mol. It is noted that the inclusion of Fe in these catalysts in the presence of H_2O_2 drastically lowers the E_a and increases their activity for IPA oxidation. The results of the E_a values for the H_2O_2 decomposition were obtained in literature in the range of 80.2 kJ/mol for ZrO_2 [25], 48 kJ/mol for ZnO [28], and 5.32 kJ/mol for activated bentonite [31].

To test the feasibility of the present work compared to some catalysts commonly used for IPA oxidation reported in the literature, the catalytic activity data of catalysts in the removal of IPA was summarized in Table 4. This study showed that our catalysts exhibit high efficiency, being as efficient as materials such as $Pt/Al_6Si_2O_{13}$ for BeFe/Cu while significantly outperforming those reported in the literature for BeFe (Table 4).

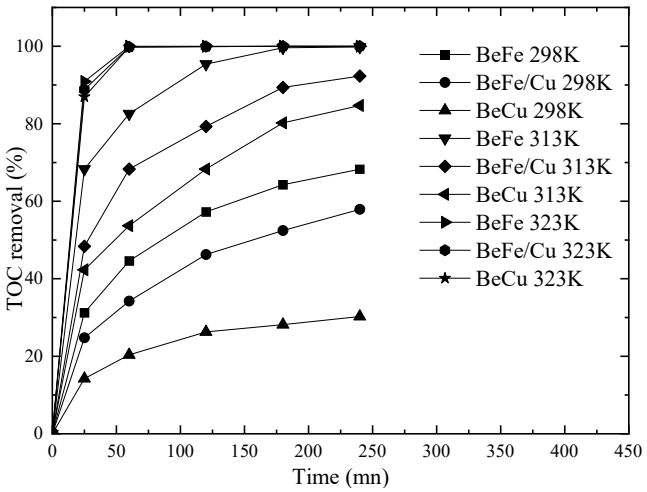

Figure 3. TOC removal by CWPO of IPA (20 ppm H_2O_2 and 1 g of BeFe, BeCu, and BeFe/Cu) at different temperatures.

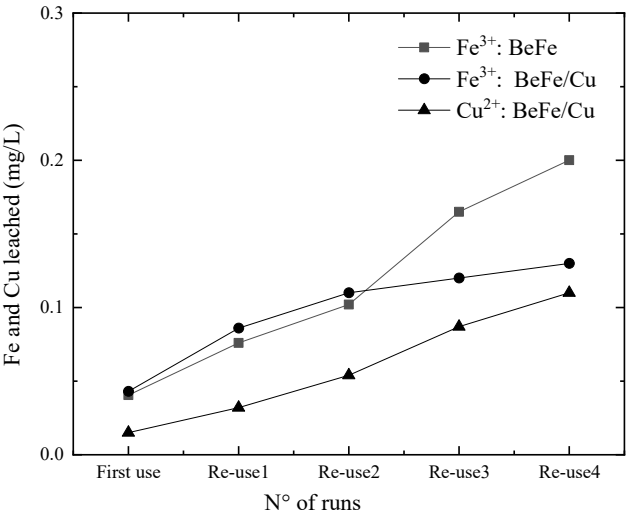

Figure 4. Evolution of Fe leached from BeFe and BeFe/Cu during the oxidation runs.

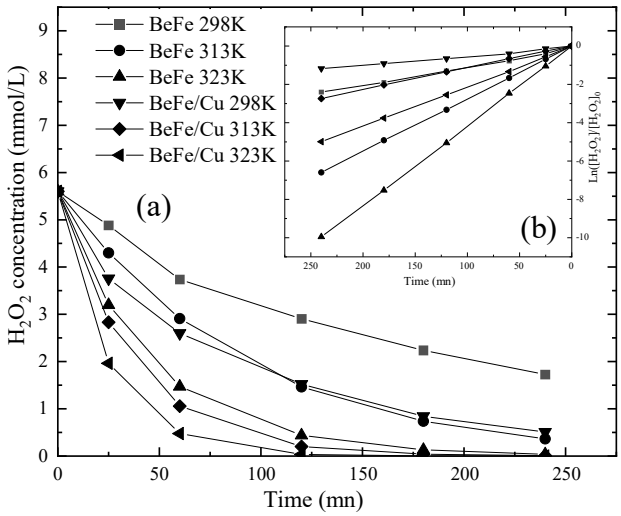

Figure 5. Decomposition kinetics of H_2O_2 with BeFe and BeFe/Cu at three different temperatures.

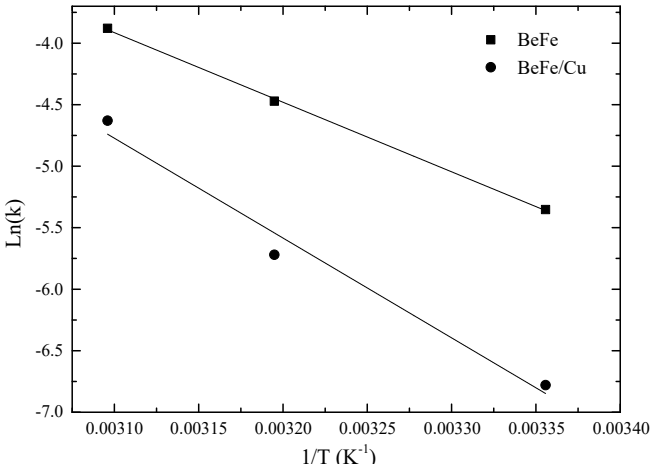

Figure 6. Arrhenius plot of the apparent kinetic constant for H2O2 decomposition with BeFe and BeFe/Cu.

Table 3. Comparison of the catalytic activity of the present catalysts in the removal of IPA with reports published in other literature.

Catalysts	Reaction temperature (K)	Removal efficiency (%)	Refs.
ZrO_2	473	100	[25]
$Pt/Al_6Si_2O_{13}$	573	90	[26]
Mo/V	423	90	[27]
ZnO	333	97	[28]
NaX-zeolite	393	97	[29]
Activated bentonite	303	62	[31]
BeFe	303	99	In this study
BeCu	303	82	In this study
BeFe/Cu	303	90	In this study

CONCLUSIONS

Wastewater containing IPA is difficult to decompose using conventional treatment processes. An AOPs has been recognized as a promising process for IPA and other hazardous organic wastewater treatment. PILCs prepared from Fe, Cu, and Fe/Cu with commercial Algerian bentonite were used for the removal of IPA using AOPs with H_2O_2 at 298 K. The catalysts based on Be with Fe showed a higher activity for the IPA and TOC removal, while BeFe/Cu decomposed H_2O_2 more rapidly, producing more $^{\bullet}OH$ radicals than BeFe. This last species is much less active for oxidation in the mild conditions used. The kinetic analysis of the H_2O_2 decomposition showed that the reaction correlated well with the PFO reaction model. On the other hand, the E_a values obtained for the decomposition of H_2O_2 using both BeFe and BeFe/Cu catalysts supported the conclusions about the different oxidation mechanisms of these two clays. The high activity of BeFe/Cu for the decomposition of H_2O_2 gives it great importance for removing organic pollutants from wastewater.

REFERENCES

[1] Y. Xiao, H.Y. Xu , H.M. Xie, Z.H. Yang, G.M. Zeng, Int. J. Environ. Sci. Technol. 12 (2015) 2381-2388. https://doi.org/10.1007/s13762-014-0634 -8.

[2] H.L. Sheng, S.W. Chuen, J. Hazard. Mater. 106 (2024) 161-168. https://doi.org/10.1016/j.jhazmat.2003.11.012.

[3] Y.H. Teow, Y.H. Chiah, K.C. Ho, E. Mahmoudi, J. Clean. Prod. 337 (2022) 130569 https://doi.org/10.1016/j.jclepro.2022.130569.

[4] Q. Tran, C. Hsieh, T.Y. Yang, H. Tung, J. Water. Reuse. Desalin. 9 (2019) 213-224. https://doi.org/10.2166/wrd.2019.015

[5] Y. Deng, R. Zhao, Curr. Pollut. Rep. 1 (2015) 167-176. https://doi.10.1007/s40726-015-0015-z.

[6] J. J. R. Marquez, I. Levchuk, M. Sillanpaa, Catalysts. 8 (2018) 1-18. https://doi:10.3390/catal8120673.

[7] Z. U. H. Khan, N. S. Gul, S. Sabahat, J. Sun, K. Tahir, N. S. Shah, M. Nawshad, A. Rahim, M. Imran, J. Iqbal, T. M. Khan, S. Khasim, U. Farooq, J. Wu, Ecotoxicol. Environ. Saf. 267 (2023) 115564. https://doi.org/10.1016/j.ecoenv.2023.115564.

[8] C. Amor, J. R. Fernandes, M. S. Lucas, J. A. Peres, Environ. Technol. Innov. 21 (2021) 101183 https://doi.org/10.1016/j.eti.2020.101183.

[9] T.B. Nguyen, C. Di Dong, C.P. Huang, C.W. Chen, S.L. Hsieh, S. Hsieh, J. Environ. Chem. Eng. 8 (2020), 104139, https://doi.org/10.1016/j.jece.2020.104139.

[10] S. Queiros, V. Morais, C. S.D. Rodrigues, F.J. Maldonado-Hodar, L. M. Madeira, Sep. Purif. Technol. Volume 141 (2015) 235-245. https://doi.org/10.1016/j.seppur.2014.11.046.

[11] J. Zheng, H. J. Lim, T. Hedtke, J. H. Kim, S. Zhang, Appl. Catal. B. 359 (2024) 124531. https://doi.org/10.1016/j.apcatb.2024.124531.

[12] Y. Sun, P. Zhou, P. Zhang, S. Meng, C. Zhou, Y. Liu, H. Zhang, Z. Xiong, X. Duan, B. Lai, Chem. Eng. J. 450 (2022) 138423. https://doi.org/10.1016/j.cej.2022.138423.
[13] W. Gao, J. Tian, Y. Fang, T. Liu, X. Zhang, X. Xu, X. Zhang, Chemosphere 243 (2020) 125334. https://doi.org/10.1016/j.chemosphere.2019.125334.
[14] J. Baloyi, T. Ntho, J. Moma, RSC. Adv. 8 (2018) 5197-5211. https://doi.10.1039/C7RA12924F.
[15] F. Ayari, G. Manai, S. Khelifi, M.T. Ayadi, J. Saudi. Chem. Soc. 23 (2019) 294-306. https://doi.org/10.1016/j.jscs.2018.08.001.
[16] J Zhu, K. Wen, Y. Wang, L. Ma, X. Su, R. Zhu, Y. Xi, H. He, Micropor. Mesopor. Mat. 265 (2018) 104-111. https://doi.org/10.1016/j.micromeso.2018.02.007.
[17] J. Baloyi, T. Ntho, J. Moma, RSC Adv. 10 (2018) 5197-5211. https://doi.org/10.1039/C7RA12924F.
[18] R. Romero, Catalysts 159 (2025) 2-29. https://doi.org/10.3390/catal15020159.
[19] N. Bueno, A. Perez, R. Molina, S. Moreno, Catal. Today 418 (2023) 114135. https://doi.org/10.1016/j.cattod.2023.114135.
[20] L. Hurtadoa, R. Romeroa, A. Mendozaa, S. Brewer, K. Donkor, R.M. G. Espinosa, R. Natividad, J. Photochem. Photobiol. A. 373 (2019) 162-170. https://doi.org/10.1016/j.jphotochem.2019.01.012.
[21] M. K. Zamisa, T. W. Seadira, S. J. Baloyi, Environ. Pollut. 361 (2024) 124842. https://doi.org/10.1016/j.envpol.2024.124842.
[22] S. Minz, S. Garg, R. Gupta, Indian Chem. Eng. 60 (2018) 16-36, https://doi.org/10.1080/00194506.2016.1270780.
[23] H. Belhadjltaief, M.Benzina, M. E. Galvez, P. D. Costa, C. R. Chim.18 (2015) 1161-1169. https://doi.org/10.1016/j.crci.2015.08.004
[24] Q. T. P. Tran, Y. H. Chuang, S. Tan, C. H. Hsieh, T. Y. Yang, H Tung, Ind. Eng. Chem. Res. 60 (2021) 12461-12473. https://doi.org/10.1021/acs.iecr.1c01464.
[25] M. Sadiq, M. Ali, R. Aman, H.U Rashid, M. N. Umar, Quim. Nova. 38 (2015) 891-895. http://doi.org/10.5935/0100-4042.20150097.
[26] R. Abbas-Ghaleb, D. Chlala, Braz. J. Chem. Eng. 36 (2019) 1175-1184. https://doi.org/dx.doi.org/10.1590/0104-6632.20190363s20190023.
[27] N. I. Aghayeva, S. A. Mamedkhanova, Processes Petrochem. Oil Refin. 24 (2023) 371-378. https://doi.org/10.36719/1726-4685/94/371-378
[28] Y. Dehmani, A. Amhoud, S. Abouarnadasse, Int. J. Anal. Chem. 7 (2021) 6667551. https://doi.org/10.1155/2021/6667551.
[29] R. Beauchet, J. Mijoin, I. Batonneau-Gener, P. Magnoux, Appl. Catal. B. 100 (2010) 91-96, https://doi.org/10.1016/j.apcatb.2010.07.017
[30] T. Xue, L. Yang, Front. Chem. 9 (2021) 751581. https://doi:10.3389/fchem.2021.751581.
[31] A. Abdulloh, G. Supriyanto, O. W. Ningsih, Adsorption of isopropyl alcohol (IPA) in water using activated bentonite, in 2nd International conference on collaboration seminar of chemistry and industry, Surabaya, Indonesia (2018), p. 217. https://doi.org/10.1088/1755-1315/217/1/012013.
[32] H. Wang, S. Schoebel, F. Schmitz, H. Dong, K. Hedfalk, MethodsX. 7 (2020) 100816. https://doi.org/10.1016/j.mex.2020.100816.
[33] A.Varon Lopez, K. H. Lopez, S. Giannakis, N. Benítez, J. Photochem. Photobiol. A. 344 (2017) 228-237. https://doi.org/10.1016/j.jphotochem.2017.04.019.
[34] C. L. Lopez, J. M. Pascual, M. V. M. Toledo, M. M. Munıo, E. Hontoria, J. M. Poyatos, Int. J. Environ. Sci. Technol. 12 (2015) 3255-3262. https://doi.org/10.1007/s13762-015-0755-8.

ZOHRA MECABIH

UKLANJANJE IZOPROPIL-ALKOHOLA IZ OTPADNIH VODA KORIŠĆENJEM BENTONITA MODIFIKOVANOG POMOĆU Fe, Cu I Fe-Cu

Department of Chemistry, Faculty of Exact Sciences,

Djillali Liabes University

Sidi Bel Abbes, Algeria

Katalizatori na bazi prečišćenog bentonita (Be) sa Fe^{3+} (BeFe), Cu^{2+} (BeCu) i Fe-Cu (BeFe/Cu) sintetizovani su iz alžirskog bentonita i korišćeni za tretman izopropil-alkohola (IPA) katalitičkom mokrom peroksidnom oksidacijom sa H_2O_2 na 298 K. BeFe je pokazao veću aktivnost za uklanjanje IPA od BeFe/Cu, koji je bio aktivniji za razgradnju H_2O_2. Kinetika reakcije je ispitana sa oba katalizatora korišćenjem modela reakcije pseudo-prvog reda. Vrednosti prividne energije aktivacije razgradnje H_2O_2, koje su određene iz Arenijusove jednačine, iznosile su 46 kJ/mol za BeFe sa obilnim formiranjem $OH^{\cdot}$ radikala i 67 kJ/mol za BeFe/Cu sa produkcijom O_2, koji ima nizak oksidacioni kapacitet na 298 K.

Ključne reči: Oksidacija izopropil-alkohola, pilarne gline, Cu, Fe, Fe-Cu.

NAUČNI RAD

CI&CEQ
Chemical Industry & Chemical Engineering Quarterly

Available online at
Association of the Chemical Engineers of Serbia AChE
www.ache.org.rs/CICEQ

Chem. Ind. Chem. Eng. Q. 32 (2) 133–142 (2026) CI&CEQ

STEVA M. LEVIĆ[1]

JELENA JOVIČIĆ-PETROVIĆ[1]

MILICA MIRKOVIĆ[1]

SLAVICA KEREČKI[1]

KATA TRIFKOVIĆ[2]

VIKTOR NEDOVIĆ[1]

VERA RAIČEVIĆ[1]

[1]University of Belgrade,
Faculty of Agriculture,
Belgrade, Serbia

[2]Inlecom Commercial Pathways,
Gateway Business Suites,
Killarney, Ireland.

SCIENTIFIC PAPER

UDC 631.4:631.461:579

SPRAY DRYING OF PHOSPHATE-SOLUBILIZING BACTERIA FOR THE PRODUCTION OF NEW BIOFERTILIZERS

Highlights

- Phosphate-solubilizing strains of *Azotobacter*, *Pseudomonas,* and *Bacillus* were characterized.
- Selected strains showed multifunctional plant growth-promoting traits.
- The spray drying method was successfully applied for bacteria encapsulation.
- Encapsulates with particle size below 5 μm were obtained, suitable for seed inoculation.
- The encapsulation procedure requires further optimization to achieve higher cell numbers.

Abstract

Phosphate-solubilizing bacteria represent a sustainable solution to cope with phosphorus unavailability in agricultural soil. However, the success of their application is highly dependent on multiple environmental factors, and a novel approach is needed for bioformulations. The present study aimed to evaluate the suitability of the spray drying method for encapsulation of phosphate-solubilizing bacteria Azotobacter chroococcum F14/2, Bacillus megaterium 11/3, and Pseudomonas putida P1. Three strains were characterized, grown under optimal conditions, and encapsulated as a whole medium-cell system using the spray drying method and maltodextrin as carrier material. The described procedure provided encapsulates with an average particle size below 5 μm, moisture content under 10%, and satisfactory powder properties. The cell viability of encapsulates (after storage) was in the following order: Bacillus megaterium 11/3 > Azotobacter chroococcum F14/2 > Pseudomonas putida P1. Additional protection during spray drying was most probably achieved by the presence of microbial exopolysaccharides, which opened the possibilities for further optimization of encapsulation procedures.

Keywords: Azotobacter, Pseudomonas, Bacillus, encapsulation, soil.

INTRODUCTION

Plants require phosphorus (P) for their biological cycle and it is considered as one of the main nutrients for efficient crop production [1]. Despite the abundance of P in the soil, it generally remains unavailable for the plants, especially under unfavorable soil pH [2]. Modern agriculture is mainly based on P, which is implemented into the soil via mineral fertilizers. The implementation of P by fertilizers is one of the main issues in modern agriculture, especially regarding the accelerated depletion of P minerals used in fertilizer production [1]. Hence, there is a rising interest in new solutions for P management in agriculture.

Despite the important role of phosphate-solubilizing microbes in plant nutrition and the P biogeochemical cycle, the research on those microbes is far behind studies on nitrogen-fixing microbes [3]. Inoculation of plant seeds by phosphate-solubilizing bacteria could potentially improve the P soil dynamic, reduce the need for the application of commercial fertilizers, and generally improve the ecological aspect of modern agriculture [4]. Phosphate-solubilizing microbes are identified among various species of bacteria [5]. Two main mechanisms are known regarding the increase of P availability by beneficial microbes. One of them is the solubilization of insoluble phosphates due to local acidity increase by acid production, and the other mechanism includes the activity of phosphatases,

Correspondence: S. Lević, Department of Food Technology and Biochemistry, University of Belgrade, Faculty of Agriculture, Nemanjina 6, 11080, Belgrade, Serbia,
Email: slevic@agrif.bg.ac.rs
Paper received: 16 December, 2024
Paper revised: 17 April, 2025
Paper accepted: 11 June, 2025

https://doi.org/10.2298/CICEQ241216017L

important for the mineralization of P contained in the form of organic compounds [6].

Bacteria exhibiting one or both mechanisms affect plant nutrition, thus belonging to the group of Plant Growth Promoting Bacteria (PGPB). Those microbes may additionally exhibit other plant growth-promoting (PGP) traits such as the production of siderophores, indole-acetic acid (IAA), and exopolysaccharides, which represent not only an important added value, but it was also confirmed that they show synergistic effects which leads to a better phosphate solubilization [7,8]. *Azotobacter* representatives are recognized as beneficial inoculants in agriculture mainly because of their nitrogen-fixing ability [9]. *Bacillus* and *Pseudomonas* species, particularly *B. megaterium* and *P. putida* are known in terms of increasing P availability to plants [10]. Besides well-described beneficial effects, the success of the promising strains' application is highly dependent on multiple environmental factors.

The main issue regarding the implementation of plant-beneficial microbes is related to their susceptibility to unfavorable environmental conditions that may hinder microbe's positive effects on plant growth. To overcome these limitations of as-prepared biomass and its further implementation in the agro sector, especially as PGP agents, encapsulation may be included in biomass preparation steps [11]. Encapsulation is usually defined as the protection of an active compound by the formation of layer(s) of selected carrier material(s) suitable for specific applications. In this regard, by applying an adequate encapsulation method, encapsulates could be formed into various shapes and sizes. Spray drying remains the main encapsulation technique accepted by many industries as a cost-effective and very efficient method for the production of encapsulates in the form of fine powders and with low water content [12]. Also, spray drying showed its potential for encapsulation of soil-beneficial microbes, such as P-solubilizing microorganisms [13].

As far as we know, this is the first study dealing with the encapsulation of non-spore-forming bacterial strains by spray drying (with maltodextrin as carrier material) and with the bacterial products formed during cultivation to be used as biofertilizers. In addition, there is a lack of studies that cover the entire pathway of processing PGPB into biofertilizers, i.e. isolation, identification, cultivation of the biomass, encapsulation, and characterization of the encapsulates. Taking into account all the points mentioned above, the aim of the present study was to evaluate the suitability of the spray drying method for encapsulation of beneficial phosphate-solubilizing bacteria belonging to different genera of PGPB. The bacterial strains *Azotobacter chroococcum* F14/2, *Bacillus megaterium* 11/3, and *Pseudomonas putida* P1 were characterized, grown under optimal conditions, and encapsulated as whole medium-cells system using spray drying method and maltodextrin as carrier material. The obtained encapsulates were analyzed in terms of morphological, physical, and chemical properties. Also, the viability of encapsulated phosphate-solubilizing bacterial strains was tested following the encapsulation procedure and after the storage period.

MATERIALS AND METHODS

Bacterial Isolation and Identification

Bacterial isolates used in this study originate from agricultural soil and were obtained using the standard dilution method and selective media. *A. chroococcum* F14/2 was isolated on the Fiodorov agar medium [14], and *B. megaterium* 11/3 was isolated on the National Botanical Research Institute's phosphate medium with $Ca_3(PO_4)_2$ (NBRIP; [15]). The NBRIP medium was used to search for isolates that can solubilize P, thus forming halo zones on the media. *A. chroococcum* F14/2 and *B. megaterium* 11/3 were identified and characterized within the research being presented; *P. putida* P1 was identified to the species level and characterized as PGPB in a previous research by Karličić *et al*. [16].

DNA isolation of the bacterial strains was performed using the Soil Mini-Prep Kit (Zymo Research, USA). The 16S rRNA region of *A. chroococcum* F14/2 was amplified with 63F and 1387 primers. A PCR reaction volume of 50 µL consisted of 5 µL 10xBuffer, 1 µL dNTP mix, 2 µL of each primer, 0.2 µL Taq polymerase, 1 µL template DNA, and RNAse free water up to 50 µL. The applied PCR program was: 95 °C/5 min, 35 cycles (95 °C/30 s, 55 °C/30 s, and 72 °C/1 min), 72 °C/1 min. The 16S rRNA region of *B. megaterium* 11/3 was amplified using the primer pair UNI 16SR/UNI 16SF. The Fast Gene Taq HotStart PCR Kit (Kapa Biosystems) was used for the PCR mixture consisting of: 10 µL 10xBuffer, 3 µL 25 $MgCl_2$, 1 µL dNTP mix, 2 µL of each primer, 0.2 µL Taq polymerase, 1 µL DNK, and RNA free water until 50 µL. The mixture was subjected to the following regime: 95 °C/5 min, 35 cycles (95 °C/30 s, 55 °C/30 s, and 72 °/1 min) and 72 °C/1 min. PCR products were sequenced in both directions by the Macrogen Sequencing Service (Macrogen Europe, Amsterdam, The Netherlands), using the same primer pairs as in the PCR reaction. Consensus sequences were compared with representative sequences from the Gene Bank database. 16S rRNA sequences of the strains included in the research are deposited to the Gene Bank database under the following accession numbers: OP975801 and ON478151 for *A. chroococcum* F14/2 and *B. megaterium* 11/3, respectively.

Characterization of Plant Growth Promoting Activity

Phosphate-solubilization capacity of the strains was tested on an NBRIP medium as described by Nautiyal [15]. The NBRIP medium was spot-inoculated and incubated at 30 °C for two weeks. The test was performed in three replicates. After measurement of halo zones and colony diameter, the solubilization index (*SI*) was calculated as follows:

SI = (colony diameter + halo zone diameter) / colony diameter.

The capability of tested strains to produce acid and alkaline phosphatase as well as naphthol-AS-BI-phospho-hydrolase was tested by API ZYM test (bioMérieux, France) according to the manufacturer's instructions.

The siderophore production was tested on a modified Chrome Azurol S (CAS) medium as described by

Lakshmanan *et al.* [17]. The appearance of a yellow-orange zone around the colony was considered a positive result. The production of exopolysaccharides (EPS) was tested on a medium for stimulation of the EPS production, according to Paulo *et al.* [18]. Sterile filter paper discs (5 mm Ø) were placed on the medium, inoculated with 5 µL of overnight bacterial cultures, and incubated for 48 h at 30 °C. The presence of slime around the discs indicated EPS production, which was confirmed by the formation of precipitates after mixing the slime with 96% ethanol. The colorimetric method described by Patten and Glick [19] was used to determine the indole-acetic acid (IAA) production by bacterial strains. Briefly, the strains were grown in a medium amended with 100 µg/mL of L-tryptophan (Sigma Aldrich, USA) for 72h at 30 °C and 150 rpm (Environmental Shaker-Incubator ES-20, BIOSAN, Latvia), and the supernatant mixed with the Salkowski reagent was used for the absorbance measurement at 530 nm (T70 UV/VIS Spectrometer, PG Instruments Ltd). A calibration curve was obtained by measuring the absorbance of solutions in the concentration range of 1-100 µg/mL of IAA (Sigma Aldrich, USA).

Encapsulation

Cultivation of Bacterial Strains

Bacterial strains were grown separately, by gradually increasing the volume of the growth media, until 1.5 L. *A. chroococcum* F14/2 was grown using a medium consisting of 10 g peptone, 10 g glucose, and 5 g NaCl per 1 L of distilled water, while *B. megaterium* 11/3 and *P. putida* P1 were grown in the Tryptic Soy Broth (Torlak, Serbia). The cultures were grown in a temperature-controlled rotary shaker (150 rpm, 30 °C) for 48 h, except for *A. chroococcum* F14/2 which was grown for 72 h. The CFU/mL in the final liquid culture was determined using a McFarland densitometer (Grant Instruments, Ltd. England).

Encapsulation Procedure

For encapsulation of the selected microorganisms, the spray drying technique and maltodextrin as a carrier material were used. After the cultivation period, the cell suspension (whole broth with the cells) was mixed with maltodextrin (10 g of maltodextrin/100 mL of cell suspension; maltodextrin (C*MD 01915), Palco, Serbia) on the magnetic stirrer for about 30 min. The encapsulation procedure was carried out using a spray drier B-290 (BÜCHI, Switzerland) under the following conditions: inlet temperature 130 °C; outlet temperature ~65 °C; liquid flow 8 mL/min. After spray drying, the samples in the powdered form were packaged in hermetic packaging and stored at room temperature and 4 °C. The yield of the encapsulation process (%) was calculated as the weight ratio of encapsulates and dry weight of feed material [20].

Characterization of the Encapsulates

Scanning Electron Microscopy (SEM)

The morphology of encapsulates was examined using scanning electron microscopy (SEM). Prior to the analysis, the samples were placed on the SEM sample stubs with a two-sided adhesive tape and plated with gold using an instrument BALTEC SCD 005. The SEM analysis was performed by a microscope JEOL JSM-6390LV (JEOL, Japan). The SEM images (of at least 100 particles) were used for the particle size analysis by the ImageJ program.

Attenuated Total Reflectance-Fourier Transform Infrared Spectroscopy (ATR-FTIR)

The chemical properties of encapsulates and the potential chemical interactions between encapsulates' constituents were investigated using an IR-Affinity-1 infrared spectrometer (Shimadzu, Japan). The measurements were performed with the attenuated total reflection (ATR) technique in the spectral range of 4000–600 cm^{-1} and at a resolution of 4 cm^{-1}. The spectra processing and presentation were realized using Spectragryph software [21]. Spectra were baseline corrected, smoothed using Savitzky-Golay filters with 5 points and the second-order polynomial function, and normalized (Standard Normal Variates, SNV).

Moisture Content

The moisture content of encapsulates was analyzed using a procedure described by Kalušević *et al.* [20]. Briefly, samples were measured before and after drying at 105 °C in the drying oven to constant mass, and the moisture content (in %) was calculated from the mass loss.

Hygroscopicity

The hygroscopicity of obtained encapsulates was measured according to the procedure described by Tomsone *et al.* [22]. Briefly, samples (1 g each) were exposed to air with ~75% relative humidity created by a saturated NaCl solution in a closed vessel. After one week, samples were weighed and hygroscopicity was calculated based on the amount of the adsorbed water (expressed as mass of adsorbed moisture/100 g of dry matter).

Bulk and Tapped Densities, Flowability, and Cohesiveness

Bulk and tapped densities of encapsulates were measured following the method recommended by European Pharmacopoeia 8.0 [23]. In short, the bulk density was calculated from the ratio between the mass of the sample and the volume it occupies in the measuring cylinder. The tapped density was determined after manual tapping of the sample in the measuring cylinder. The value of the tapped density was calculated as the ratio between the sample mass and the volume after 500 taps. The flowability of samples was calculated as a Carr index (CI, %), while the cohesiveness was expressed as the Hausner ratio (HR), based on the values of bulk and tapped densities [24].

Survival of Bacterial Strains during and after Encapsulation

Survival of bacterial strains was determined right after encapsulation and after storage for two months at room temperature and 4 °C. The encapsulates were crushed in a sterile mortar and mixed with 1% Na-citrate solution at a ratio of 1:10. Further serial dilutions were prepared with

sterile 0.9% NaCl solution, and the following selective media: Fiodorov agar [14], Nutrient agar (Torlak, Serbia), and Cetrimide agar (HiMedia Laboratories Pvt. Ltd., India) for Azotobacter, Bacillus and Pseudomonas strains, respectively.

Statistical Analysis

Analyses were performed in triplicate and data were presented as mean ± standard deviation (unless otherwise stated), using PAST software [25]. One-way ANOVA was applied to determine significant differences between the physical parameters of encapsulates. The Tukey test was used at $p \leq 0.05$ to identify significant differences among the means (or the Kruskal-Wallis test and Mann-Whitney test for the non-normally distributed data).

RESULTS AND DISCUSSION

Molecular Identification

The obtained 16S rDNA sequence of strains 11/3 and 14/2 showed a high percentage of identity (above 99% and 96%, respectively) as *Bacillus megaterium* and *Azotobacter chroococcum* strains from a database, thus confirming their belonging to these species.

Characterization of Bacterial PGP traits

All of the studied strains manifest at least one of the mechanisms to improve the P availability in soil, simultaneously showing some other PGP traits. *A. chroococcum* F14/2 and *P. putida* P1 showed the ability for both solubilization of P salts and mineralization of organic P compounds. On the other side, *B. megaterium* 11/3 produces enzymes involved in mineralization with a neglectful ability to solubilize inorganic forms of P (Table 1).

The ability to mineralize organic P compounds was observed in all three isolates through the activity of acid and alkaline phosphatase and naphthol-AS-BI-phosphohydrolase. *A. chroococcum* F14/2 and *B. megaterium* 11/3 showed the ability to produce EPSs, which was important for the successful root colonization and establishment of plant-microbe interaction. The production of IAA was observed in *P. putida* P1, which was at the same time characterized by the most pronounced phosphate solubilization activity. Our results showed that *A. chroococcum* F14/2 exhibited several mechanisms beneficial for plant nutrition, in addition to its ability to fix nitrogen (Table 1). *P. putida* P1 could also produce siderophores, while the tested *Bacillus* strain did not show this ability. Many soil bacteria usually exhibit various plant growth-promoting traits, which are also important for the successful phosphate solubilization and uptake by plants. However, these traits such as the production of siderophores, indole-acetic acid, and exopolysaccharides (Table 1) vary depending on bacteria strain and environmental conditions. For example, *Azotobacter* representatives are known for their ability to dissolve phosphates, although this cannot be considered a common PGP trait, even at the species level. While *A. chroococcum* F14/2 phosphate SI was 1.94, Kerečki *et al.* [9] reported that the positive effects of *A. chroococcum* F8/2 on sugar beet growth were related to several PGP traits, but excluding phosphate solubilization, which was tested but not confirmed. Nosrati *et al.* [26] also observed variations in the phosphate solubilization potential of multiple *Azotobacter* isolates collected from diverse soil types. *Pseudomonas*, including *P. putida* as its representative, has been recognized as a microbe involved in phosphate solubilization and mineralization [27]. It should be pointed out that soil pH can vary, which also affects the solubility of inorganic P salts; the ability to produce both acidic and alkaline phosphatase is of crucial importance for the strains' selection. Climate conditions significantly affect the activity of phosphatases, but nitrogen availability can be of specific importance when temperature and water accessibility are not limiting factors [28]. Thus, the combination of nitrogen-fixing and phosphate-solubilizing properties could be a promising tool for plant nutrition improvement.

Furthermore, EPS production has been described as an important factor in the solubilization of tricalcium phosphate, as bacterial EPSs showed the P-holding capacity which additionally contributes to the P availability [29]. Although there are literature findings about EPS production by *P. putida* strains [30], the tested *P. putida* P1 did not show the ability to produce EPS. According to Sandhya and Ali [31], this trait can be highly dependent and triggered by the presence of some stressors in the environment, so the ability to produce EPS cannot be completely excluded under environmental conditions.

Regarding P, some findings show not only the indirect effect of bacterial IAA on root development and nutrient uptake but also the promotion of organic acids secretion by IAA, which directly affects phosphate solubilization [32]. We detected IAA production by *P. putida* P1, which was consistent with the previously described *P. putida* strains that exhibit both phosphate solubilization and IAA production activity [33]. Pyoverdine is a widely studied siderophore produced by bacteria from the *Pseudomonas* genus, whose primary role is in iron uptake, but other functions include improvement of access to phosphates in nutrient-depleted soil [34]. Thus, in addition to phosphate solubilization and mineralization, the demonstrated PGP traits identified among the tested bacterial strains in the present study could contribute significantly to the potential of bacterial strains to improve P uptake efficiency. The set of traits indicates the potential of tested strains to be used as microbial inoculants in modern agriculture.

Encapsulation of Phosphate-Solubilizing Bacteria

As we showed above, selected bacterial strains exhibit promising phosphate-solubilizing and plant growth-promoting properties. However, after cultivation, bacterial biomass is unstable for a long period of storage and also difficult to apply, especially for plant seed covering. Namely, to fulfill its role as a growth-promoting agent, it is necessary to introduce the bacterial biomass close to the plant root system. Hence, covering the plant seeds prior to planting is a promising strategy for inoculation of crops. The important issue in the use of beneficial soil microbes is providing a stable product until the expected sowing season [35]. In this regard, spray drying is a technique that

provides fast water removal from bacterial biomass which is essential for the preservation of bacterial cells, thereby reducing shipping and storage costs.

Therefore, in the present study, bacterial biomass, together with growth medium, was encapsulated using a spray drying technique and maltodextrin as a carrier material. This approach should provide encapsulates suitable for plant seed inoculation with phosphate-solubilizing microbes aimed to enhance P availability for plants and reduce the use of industrial fertilizers. Additionally, we applied encapsulation of the whole cell suspension (broth with the cells), which eliminated the biomass separation step, thus reducing the waste and simplifying the production procedure, while preserving most of the valuable extracellular metabolites.

Morphological Properties of Encapsulates

As a result of spray drying encapsulation of whole cells/media suspensions, fine powders were obtained. The color of the encapsulates (i.e. powders) was white (*A. chroococcum* F 14/2 encapsulate) or pale brown (*B. megaterium* 11/3 and *P. putida* P1 encapsulates) due to differences in the color of the media; the *Azotobacter* growth medium was white, while the *Bacillus* and *Pseudomonas* growth media exhibited brown color as a result of different chemical compositions. Detailed data on the physical properties of encapsulates (powders) are provided in Table 2. The encapsulation process yield was also affected by the growth media composition; the yield of *A. chroococcum* F 14/2, *B. megaterium* 11/3 and *P. putida* P1 encapsulates was 60.9±5.0%, 79.4±7.2%, and 76.3±4.7%, respectively.

The obtained encapsulates' particles (Fig. 1) were spherical or irregularly shaped, depending on the sample that was subjected to spray drying. The encapsulates showed micromorphological properties that are typical for particles obtained by spray drying and maltodextrin as a carrier material [36]. Maltodextrin is a suitable carrier for the encapsulation processes by the spray drying technique and provides encapsulates with suitable morphological and physical properties. In addition, the yield of maltodextrin-based encapsulates is high, making them suitable for the encapsulation of complex mixtures of active ingredients. Although other carriers, such as gum Arabic, may be even more suitable for encapsulation by spray drying [20], maltodextrin is cheaper and more readily available compared to many other carrier materials. Here should be mentioned that the initial spray drying trials without maltodextrin resulted in high losses, i.e., low product yield. Also, the spray-dried encapsulates without maltodextrin were sticky and inappropriate for further analysis and handling.

However, the observed surface properties of encapsulates were different, depending on the bacterial species used for spray drying. As can be seen, encapsulates of *A. chroococcum* F14/2 show smoother surfaces (which are even more pronounced in the case of smaller particles) compared to the other two formulations. Namely, the smoother surface of *A. chroococcum* F14/2 encapsulates could be explained by the presence of exopolysaccharides produced during cell cultivation. According to literature data, *Azotobacter* species produce exopolysaccharides that belong to the group of alginates [37]. The presence of alginate and generally polysaccharides in the formulations for spray drying could provide more structurally stable particles [38]. As our results showed (Table 1), *A. chroococcum* F14/2 and *B. megaterium* 11/3 produced exopolysaccharides, consequently providing an additional carrier material and encapsulates with more desirable surface properties. In this context, strains should be tested for the presence of EPS or even grown under conditions that promote EPS production. The significant presence of the EPS could reduce the need to add commercial polysaccharides (such as alginates) in formulations for spray drying encapsulation, reducing process costs and providing better protection of the biofertilizer. The encapsulate size (Table 2) is generally in the ranges common for formulations based on maltodextrin as a carrier material, while the formation of poly-dispersed particles is also noticed, which is expected during spray drying [36].

Physical Properties of Encapsulates

The main physical properties of encapsulates are shown in Table 2. Hygroscopicity of samples was in the range of ~8–17 g H_2O/100 g, depending on encapsulated bacterial species.

The hygroscopicity of encapsulates obtained in this study was in accordance with the literature data for spray dried-maltodextrin/alginate-based encapsulates (11-15 g H_2O/100 g) [38]. Generally, the higher hygroscopicity is an obstacle to storage, manipulation, and potential application of encapsulates, especially for seed coating. Yonekura *et al*. [38] showed that the samples with low moisture contents exhibited low hygroscopicity. From this, one could conclude that increased moisture content (and hygroscopicity) could lead to undesirable biochemical reactions at the cellular level and consequently to a reduction in cell number during storage. This may partly explain the lower cell count in the *Pseudomonas putida* P1 encapsulates after storage (i.e. the encapsulates with the highest moisture content and hygroscopicity). On the other hand, *Azotobacter chroococcum* F14/2 encapsulates exhibited much lower hygroscopicity compared to the other two bacterial encapsulates. As we showed above, the particles with encapsulated *Azotobacter* cells have smoother surfaces, which probably provide a better barrier for moisture. However, these results pointed out that to preserve the physical properties of encapsulates and to maintain high cell viability, proper packaging of encapsulates should be considered. Further improvement of the spray drying process could be aimed at optimizing the encapsulation parameters, especially in reducing the moisture content in the encapsulates. In general, the moisture content of spray-dried powders containing live cells should be below 4% for prolonged storage [38]. It could be achieved by increasing the drying temperature. However, higher drying temperatures can lead to thermal damage to the cells. In this regard, spray drying encapsulation of phosphate-solubilizing bacteria requires optimization of various process parame-

ters such as growth conditions, drying temperature, carrier composition, and storage conditions.

To evaluate the handling properties of encapsulates, bulk, and tapped density, the Carr index (CI) and Hausner ratio (HR) were measured or calculated (Table 2). The values for the Carr index (CI) and Hausner ratio (HR) were in ranges of 27-34% and 1.38-1.51, respectively. According to Jinapong *et al.* [24], the values for the CI below 15% indicate a very good flowability of powders, while with CI values above 45%, the flowability is considered very bad. Also, according to the same authors, cohesiveness expressed as the Hausner ratio could be classified as low (HR < 1.2), intermediate (HR = 1.2-1.4), and high (HR > 1.4). Spray-dried encapsulates of phosphate-solubilizing bacteria obtained in this study can be classified as powders with fair flowability and intermediate cohesiveness. Here also *A. chroococcum* F14/2 encapsulates showed better flowability and cohesiveness in comparison with *B. megaterium* 11/3, and *P. putida* P1 encapsulates. Hence, handling, storage, and general manipulation of *A. chroococcum* F14/2 encapsulates should be more convenient, especially for potential application on seeds and further encapsulate processing, such as agglomeration.

Chemical Properties of Encapsulates

FTIR spectroscopy was used to test the chemical stability of encapsulates and to identify changes in their chemical properties as a result of chemical interactions between constituents (Fig. 2).

Table 1. Plant growth-promoting (PGP) properties of *Azotobacter chroococcum* F14/2, *Bacillus megaterium* 11/3, and *Pseudomonas putida* P1 (the latest characterized within Karličić *et al.* [16]).

	Bacterial strain		
Plant Growth Promoting Characteristic	*Azotobacter chroococcum* F14/2	*Bacillus megaterium* 11/3	*Pseudomonas putida* P1
Phosphate solubilization index (SI)	1.94	1.11	2.70
Production of alkaline phosphatase	+	+	+
Production of acidic phosphatase	+	+	+
Production of naphthol-AS-BI-phosphohydrolase	+	weak	+
Production of exopolysaccharides (EPS)	+	+	-
Production of indole-acetic acid (IAA)	-	-	1.2 μg/ml
Production of siderophores	+	-	+

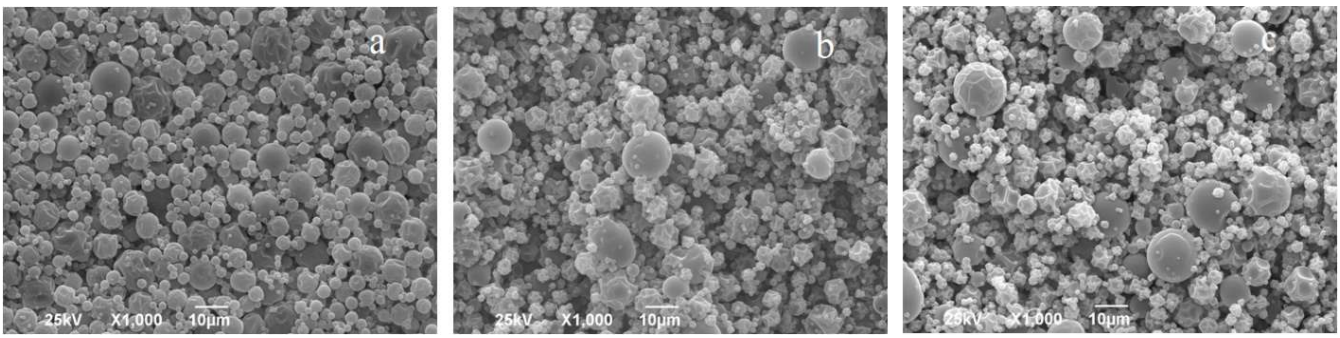

Fig. 1 SEM micrographs of Azotobacter chroococcum F14/2 (a), Bacillus megaterium 11/3 (b), and Pseudomonas putida P1 (c) spray-dried encapsulates.

Table 2. Physical properties of encapsulates.

Sample (encapsulates)	Mean particles size±s.d.* (μm)	Moisture content (%)	Hygroscopicity g H_2O/100 g of sample	Bulk density (g/mL)	Tapped density (g/mL)	CI (%)	HR
Azotobacter chroococcum F14/2	3.4±2.8^{a}	5.62±0.07^{a}	8.93±0.02^{a}	0.28 ± 0.00^{a}	0.39 ± 0.01^{a}	27.51 ± 1.86^{a}	1.38 ± 0.03^{a}
Bacillus megaterium 11/3	4.7±3.8^{b}	7.73±0.04^{b}	18.68±0.01^{b}	0.29 ± 0.01^{ab}	0.44 ± 0.01^{bc}	33.79 ± 1.75^{b}	1.51 ± 0.04^{b}
Pseudomonas putida P1	4.5±3.7^{b}	8.04±0.05^{c}	16.97±0.06^{c}	0.27 ± 0.01^{ac}	0.41 ± 0.01^{ad}	33.64 ± 1.05^{b}	1.51 ± 0.02^{b}

* s.d.-standard deviation

$^{a-d}$ The values in the same column superscripted with the same letter are not significantly different ($p \leq 0.05$)

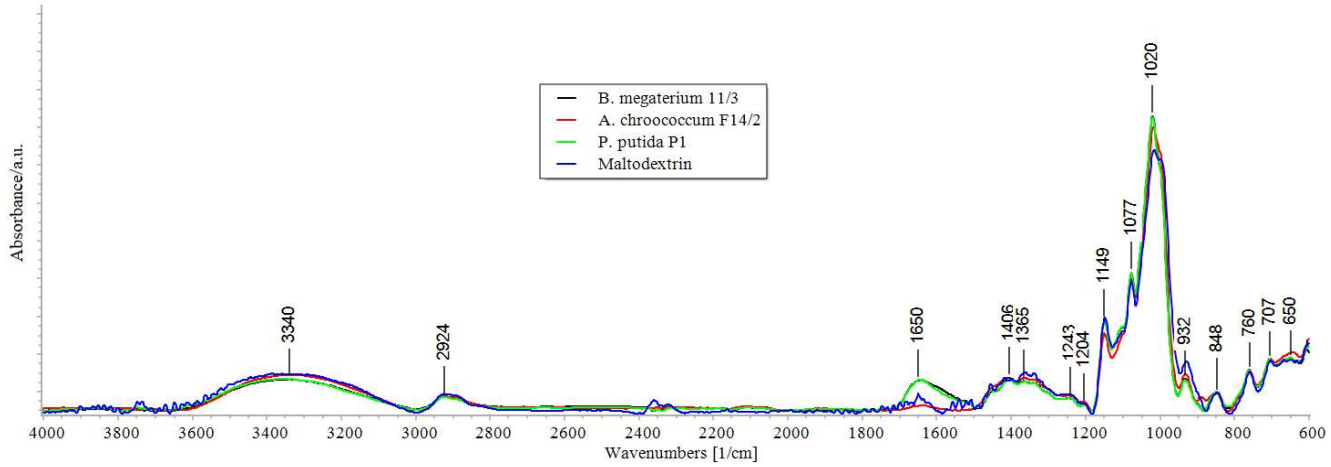

Fig. 2 FTIR spectra of encapsulates and maltodextrin.

The bands at around 3340 cm^{-1} are due to OH groups stretching vibrations and at ~ 2920 cm^{-1} is the band of C-H bonds. At around 1650 cm^{-1} are bands of water present in the particles, while at 1149 cm^{-1}, 1077 cm^{-1}, and 1020 cm^{-1} are bands identified as typical for carbohydrates, with low-intensity bands below 1000 cm^{-1} related to pyranose ring of sugars [39]. In the FTIR spectra of the encapsulates, the band positions associated with major encapsulate constituents, i.e., carbohydrates and primarily maltodextrin are very close, regardless of encapsulated bacterial strain. Moreover, the maltodextrin bands are dominant in all spectra of encapsulates, overlapping bands from growth media constituents and bacterial metabolic products, indicating sufficient cover-protection of cells. The similarities observed in the FTIR spectra suggest that the encapsulation procedure provides encapsulates without strong chemical interactions between constituents. Kalušević *et al.* [36] reported a similar absence of chemical interactions for spray-dried encapsulates of grape skin extract and maltodextrin. In this regard, the thermal and chemical stability of maltodextrin makes it preferable as a carrier material for spray drying encapsulation of complex liquid media and cells.

Storage Stability of Encapsulated Cells

Besides the simplified handling and application on plants, one of the most important benefits of dried microbial biofertilizers encapsulates is the possibility of their prolonged storage. Our results show that the cell viability of all tested strains was not significantly changed during encapsulation (Table 3).

However, storage significantly reduced the number of viable cells, making the applied encapsulation technique inadequate for *P. putida* P1 long storage. The number of viable *P. putida* P1 cells after two months of storage was below 3 log CFU/g, regardless of the storage temperature. On the contrary, *B. megaterium* 11/3 showed a favorable survival rate, while *A. chroococcum* F14/2 cell number declined, which was more pronounced when it was stored at room temperature.

The results for the cell number in encapsulates emphasize the importance of microbe properties, especially spores formation, for the survivability of spray-dried microbial biofertilizers. Encapsulates of *B. megaterium* 11/3 had a log CFU of 7.34 after encapsulation and 6.06 after two months of storage at room temperature. Stamenković Stojanović *et al.* [40] showed that a spore-forming *Bacillus subtilis* (after thermal shock procedure) and spray drying using maltodextrin as a carrier exhibited a very high survival rate of 8.45 log CFU/g even after storage at room temperature for one year. In this study, the lower cell number of all three encapsulated bacterial strains could be due to the lower initial cell number in the growth media. We used a rotary shaker for the production of bacterial biomass prior to encapsulation, which resulted in an overall lower cell number in the growth medium and consequently in the encapsulates compared to the literature [40]. Bioreactors with control of agitation and aeration could be used for increasing cell numbers aimed for encapsulation. On the other hand, *Azotobacter chroococcum* F14/2 encapsulates obtained in this study exhibited a relatively high number of cells compared to *Pseudomonas putida* P1. Since both species do not produce spores, and both belong to the group of Gram-negative bacteria, known as unstable as dry encapsulates [35], one of the explanations for a higher number of *Azotobacter* live cells in encapsulates could be the presence of exopolysaccharides. Namely, besides maltodextrin, exopolysaccharides may provide additional protection for cells. Polysaccharides have been used for the encapsulation of nitrogen-fixing microorganisms and effectively preserve relatively high numbers of live cells during the spray-drying process [35]. Since both *Azotobacter chroococcum* F14/2 and *Bacillus megaterium* 11/3 produce exopolysaccharides (Table 1), it could be expected that these macromolecules increase the possibility for cell survival at elevated temperatures and rapid dehydration through spray drying. On the other hand, the low number of *Pseudomonas putida* P1 cells in the encapsulates after storage could be explained by a higher moisture content of encapsulates compared to the other two bacterial species. High moisture content is the basis for more intense biochemical reactions on the cell level, which may cause increasing in the cell death rate in the case of *Pseudomonas putida* P1 encapsulates.

To overcome the problems related to the high moisture content of the encapsulates, and especially the decreasing of cell numbers during storage, an alternative encapsulation process could be considered. For example, the 'CLAM'

process (one-step, spray-dry cross-linked alginate micro-encapsulation process) that combines spray drying and gelling of carrier showed promising results in the preservation of nitrogen-fixing bacteria, enabling a high number of seed inoculants [35]. Such modification of spray drying encapsulation could be of interest for the preservation of non-spore-forming bacteria tested in this study, especially *Pseudomonas* strains, and potentially could provide biofertilizers with enhanced storage properties.

Encapsulates of the phosphate-solubilizing bacteria obtained in this study could be used in the direct seed covering. Additionally, since spray drying produced encapsulates with good physical properties, the agglomeration of the encapsulates could be applied. Agglomerated encapsulates are a more convenient form for the usual methods of fertilizer application in the fields. Also, the plant growth-promoting traits of the one bacterial strain may not be sufficient to cover the broader demands required from biofertilizers. Hence, future work could be oriented toward the creation of mixtures of various biofertilizers and the study of their effects on plant growth.

Table 3. Survival of *Bacillus megaterium* 11/3, *Azotobacter chroococcum* F14/2, and *Pseudomonas putida* P1 during and after encapsulation.

	Number of bacteria in liquid culture before encapsulation	Number of bacteria after encapsulation	Number of bacteria in encapsulates after 2 months of storage at 4 °C	Number of bacteria in encapsulate after 2 months of storage at room temperature
Bacterial strain	log CFU/mL		log CFU/g	
Bacillus megaterium 11/3	7.34±0.05	7.36±0.05	6.32±0.07	6.06±0.06
Azotobacter chroococcum F14/2	7.06±0.13	7.43±0.04	5.69±0.39	4.47±0.33
Pseudomonas putida P1	8.69±0.06	8.65±0.02	< 3	< 3

CONCLUSIONS

Three bacterial strains *B. megaterium* 11/3, *A. chroococcum* F14/2, and *P. putida* P1, characterized as beneficial PGPB, were encapsulated using spray drying technique and maltodextrin as carrier material. Variations in the properties of the obtained encapsulates were observed, and the strains showed different survival rates. The cell count after storage was highest for *B. megaterium* 11/3 (6.32 log CFU/g), followed by *A. chroococcum* F14/2 (5.69 log CFU/g) and *P. putida* P1 (<3 log CFU/g). Storage at 4 °C had a more positive effect on the preservation of the encapsulated cells compared to storage at room temperature. *A. chroococcum* F14/2 and *B. megaterium* 11/3 produced the exopolysaccharides, which could be a promising feature for the preservation of the cells and successful root colonization.

Encapsulates obtained by spray drying showed promising physical properties that open up possibilities for the application of encapsulated PGPB strains directly on the seeds i.e. by direct seed inoculation. The direct application of the encapsulated PGPB strains on seeds would overcome the relatively low cell number after storage and could allow successful root colonization and establishment of plant-microbe interaction in the early stages of plant growth.

Here should be pointed out some observed limitations of the encapsulated PGPB strains as well as the recommendations for further development. The low cell number of the encapsulates after storage could be the result of an initial lower cell count in the medium for cell cultivation. This problem could be overcome by cell cultivation in the bioreactors with controlled aeration and agitation. Optimization of growth conditions could increase the production of exopolysaccharides and other PGP traits, enabling more successful root colonization. Also, the cells could be more effectively preserved by optimization of the spray drying procedure and reduction of moisture content in encapsulates as well as by the introduction of new innovative spray drying encapsulation procedures and new carrier materials.

Acknowledgments

This work was supported by the Ministry of Science, Technological Development and Innovations, Republic of Serbia (Contract No. 451-03-137/2025-03/200116), and The Innovation Fund of the Republic of Serbia (Contract No. 244/2).

REFERENCES

[1] S.Z. Sattari, A.F. Bouwman, K.E. Giller, M.K. Ittersum, Proc. Natl. Acad. Sci. (PNAS) 109 (2012) 6348-6353. https://doi.org/10.1073/pnas.1113675109.

[2] C. Xiao, R. Chi, X. Pan, F. Liu, J. He, Ann. Microbiol. 63 (2013) 173-178. https://doi.org/10.1007/s13213-012-0458-z

[3] J. Li, J. Lu, H. Wang, Z. Fang, X. Wang, S. Feng, Z. Wang, T. Yuan, S. Zhang, S. Ou, X. Yang, Z. Wu, X. Du, L. Tang, B. Liao, W. Shu, P. Jia, J.L. Liang, Biol. Rev. 96 (2021) 2771-2793. https://doi.org/10.1111/brv.12779.

[4] Y. Li, Q. Li, G. Guan, S. Chen, PeerJ. 8 (2020) e9062. https://doi.org/10.7717/peerj.9062.

[5] Y. Wang, S. Peng, Q. Hua, C. Qiu, P. Wu, X. Liu, X. Lin, Front. Microbiol. 12 (2021) 693535. https://doi.org/10.3389/fmicb.2021.693535.

[6] G. Kalayu, Int. J. Agron. (2019) 4917256. https://doi.org/10.1155/2019/4917256.
[7] Y. Yi, W. Huang, Y. Ge, World J. Microbiol. Biotechnol. 24 (2008) 1059-1065. https://doi.org/10.1007/s11274-007-9575-4.
[8] A.A. Alemneh, G.R. Cawthray, Y. Zhou, M.H. Ryder, M.D. Denton, Arch. Microbiol. 203 (2021) 3825-3837. https://doi.org/10.1007/s00203-021-02364-w.
[9] S. Kerečki, I. Pećinar, V. Karličić, N. Mirković, I. Kljujev, V. Raičević, J. Jovičić-Petrović, J. Plant Interac. 17 (2022) 719-730. https://doi.org/10.1080/17429145.2022.2091802.
[10] N. Oteino, R.D. Lally, S. Kiwanuka, A. Lloyd, D. Ryan, K.J. Germaine, D.N. Dowling, Front. Microbiol. 6 (2015) 745. https://doi.org/10.3389/fmicb.2015.00745.
[11] M. Schoebitz, C. Ceballos, L. Ciampi, J. Soil. Sci. Plant Nutr. 13 (2013) 1-10. https://doi.org/10.4067/S0718-95162013005000001.
[12] N.J. Zuidam, E. Shimoni, in Encapsulation Technologies for Active Food Ingredients and Food Processing, N.J. Zuidam, V. Nedovic (eds.). New York (2010), p. 3. https://doi.org/10.1007/978-1-4419-1008-0.
[13] R. Brindavathy, M. Gnanachitra, Madras Agric. J. 104 (2017) 304-307. https://doi.org/10.29321/MAJ.2017.000066.
[14] G.R. Anderson, Soil Sci. 86 (1958) 57-62.
[15] C.S. Nautiyal, FEMS Microbiol. Lett. 170 (1999) 265-270. https://doi.org/10.1111/j.1574-6968.1999.tb13383.x.
[16] V. Karličić, D. Radić, J. Jovičić-Petrović, B. Lalević, F. Morina, V. Golubović Curguz, V. Raičević, iForest 10 (2017) 692-699. https://doi.org/10.3832/ifor2135-010.
[17] V. Lakshmanan, D. Shantharaj, G. Li, L.A. Seyfferth, A.L. Sherrieri, H.P. Bais, Planta 242 (2015) 1037-1050. https://doi.org/10.1007/s00425-015-2340-2.
[18] M.E. Paulo, P.M. Vasconcelos, S.I. Oliveira, de Jesus M.H. Affe, R. Nascimento, S.I. de Melo, M.R. de Abreu Roque, S.A. de Assis, Food Sci. Technol. 32 (2012) 710-714. https://doi.org/10.1590/S0101-20612012005000094.
[19] C.L. Patten, B.R. Glick, Appl. Environ. Microbiol. 68 (2002) 3795-3801. https://doi.org/10.1128/AEM.68.8.3795-3801.2002.
[20] A. Kalušević, S. Lević, B. Čalija, M. Pantić, M. Belović, V. Pavlović, B. Bugarski, J. Milić, S. Žilić, V. Nedović, J. Microencapsul. 34 (2017) 475-487. https://doi.org/10.1080/02652048.2017.1354939.
[21] F. Menges, "Spectragryph - optical spectroscopy software" [software]. (2018) Available from: http://www.effemm2.de/spectragryph/ [Accessed July 7, 2024].
[22] L. Tomsone, R. Galoburda, Z. Kruma, V. Durrieu, I. Cinkmanis, Foods 9 (2020) 1332. https://doi.org/10.3390/foods9091332.
[23] The European Pharmacopoeia, 8th edition (Ph. Eur. 8.0) (2014) Strasbourg: Council of Europe.
[24] N. Jinapong, M. Suphantharika, P. Jamnong, J. Food Eng. 84 (2008) 194-205. https://doi.org/10.1016/j.jfoodeng.2007.04.032.
[25] Ø. Hammer, D.A.T. Harper, P.D. Ryan, Palaeont. Electr. 4 (2001) 9.
[26] R. Nosrati, P. Owlia, H. Saderi, I. Rasooli, M.A. Malboobi, Iran. J. Microbiol. 6 (2014) 285-295.
[27] A. Blanco-Vargas, L.M. Rodríguez-Gacha, N. Sánchez-Castro, R. Garzón-Jaramillo, L.D. Pedroza-Camacho, R.A. Poutou-Piñales, C.M. Rivera-Hoyos, L.A. Díaz-Ariza, A.M. Pedroza-Rodríguez, Heliyon 6 (2020) e05218. https://doi.org/10.1016/j.heliyon.2020.e05218.
[28] O. Margalef, J. Sardans, M. Fernández-Martínez, R. Molowny-Horas, I.A. Janssens, P. Ciais, D. Goll, A. Richter, M. Obersteiner, D. Asensio, J. Peñuelas, Sci. Rep. 7 (2017) 1337. https://doi.org/10.1038/s41598-017-01418-8.
[29] Y. Yi, W. Huang, Y. Ge, World J. Microbiol. Biotechnol. 24 (2008) 1059-1065. https://doi.org/10.1007/s11274-007-9575-4.
[30] G.Y. Celik, B. Aslim, Y. Beyatli, Carbohydr. Polym. 73 (2008) 178-182. https://doi.org/10.1016/j.carbpol.2007.11.021.
[31] V. Sandhya, Sk. Z. Ali, Microbiology 84 (2015) 512-519. https://doi.org/10.1134/S0026261715040153.
[32] C. Bianco, R. Defez, Appl. Environ. Microbiol. 76 (2010) 4626-4632. https://doi.org/10.1128/AEM.02756-09.
[33] S. Srivastava, S. Srivastava, Sci. Rep. 10 (2020) 5855. https://doi.org/10.1038/s41598-020-62725-1.
[34] X.X. Zhang, P.B. Rainey, Evolution 67 (2013) 3161-3174. https://doi.org/10.1111/evo.12183.
[35] B.M. Arbaugh, F. Rezaei, M. Mohiti-Asli, S. Pena, H.B. Scher, T. Jeoh, ACS Agric. Sci. Technol. 2 (2022) 950-959. https://doi.org/10.1021/acsagscitech.2c00107.
[36] A.M. Kalušević, S.M. Lević, B.R. Čalija, J.R. Milić, V.B. Pavlović, B.M. Bugarski, V.A. Nedović, J. Food Sci. Technol. 54 (2017) 3411-3420. https://doi.org/10.1007/s13197-017-2790-6
[37] S.S. Gauri, S.M. Mandal, B.R. Pati. Appl. Microbiol. Biotechnol. 95 (2012) 331-338. https://doi.org/10.1007/s00253-012-4159-0.
[38] L. Yonekura, H. Sun, C. Soukoulis, I. Fisk, J. Funct. Foods 6 (2014) 205-214. https://doi.org/10.1016/j.jff.2013.10.008.
[39] D.P. Vargas-Muñoz, L.E. Kurozawa, Braz. J. Food Technol. 23 (2020) e2019254. https://doi.org/10.1590/1981-6723.25419.
[40] S. Stamenković Stojanović, I. Karabegović, B. Danilović, V. Nedović, A. Kalušević, S. Mančić, M. Lazić, Span. J. Agric. Res. 20 (2022) e0803. https://doi.org/10.5424/sjar/2022203-19062.

STEVA M. LEVIĆ[1]

JELENA JOVIČIĆ-PETROVIĆ[1]

MILICA MIRKOVIĆ[1]

SLAVICA KEREČKI[1]

KATA TRIFKOVIĆ[2]

VIKTOR NEDOVIĆ[1]

VERA RAIČEVIĆ[1]

[1]University of Belgrade,
Faculty of Agriculture,
Belgrade, Serbia

[2]Inlecom Commercial Pathways,
Gateway Business Suites,
Killarney, Ireland.

NAUČNI RAD

SPREJ SUŠENJE FOSFAT-SOLUBILIZIRAJUĆIH BAKTERIJA ZA PROIZVODNJU NOVIH BIOFERTILIZATORA

Fosfat-solubilizirajuće bakterije predstavljaju održivo rešenje za suočavnje sa nedostatkom fosfora u poljoprivrednom zemljištu. Međutim, uspeh njihove primene u velikoj meri zavisi od velikog broja faktora životne sredine i potreban je novi pristup za dobijanje bioformulacija. Cilj ovog istraživanja je da se proceni pogodnost metode sprej sušenja za inkapsulaciju fosfat-solubilizirajućih bakterija: Azotobacter chroococcum F14/2, Bacillus megaterium 11/3 i Pseudomonas putida P1. Ova tri soja su okarakterisana, uzgajana pod optimalnim uslovima i inkapsulisana kao ceo sistem koji sadrži podlogu i ćelije korišćenjem metode sprej sušenja i maltodekstrina kao nosača. Opisanim postupkom dobijeni su inkapsulati sa prosečnom veličinom čestica ispod 5 µm, sadržajem vlage ispod 10% i zadovoljavajućim svojstvima za praškaste uzorke. Ćelijska vijabilnost inkapsulata (nakon čuvanja) bila je sledećim redom: Bacillus megaterium 11/3 > Azotobacter chroococcum F14/2 > Pseudomonas putida P1. Dodatna zaštita tokom sprej sušenja najverovatnije je postignuta prisustvom mikrobnih egzopolisaharida, što otvara mogućnosti za dalju optimizaciju postupaka inkapsulacije.

Ključne reči: Azotobacter, Pseudomonas, Bacillus, inkapsulacija, zemljište.

Chemical Industry & Chemical Engineering Quarterly

Available online at
Association of the Chemical Engineers of Serbia AChE
www.ache.org.rs/CICEQ

Chem. Ind. Chem. Eng. Q. 32 (2) 143–151 (2026) CI&CEQ

VENKATESAN SUBRAMANIAN

RAGHU PALANI

Department of Mechanical Engineering, Sri Venkateswara College of Engineering,

Tamil Nadu, India.

COMPARATIVE ANALYSIS OF MORINGA OIL AND RUBBER SEED OIL BIODIESELS IN DIESEL ENGINES

Highlights

- The performance of biodiesel blends (MO20 and RB20) improves as brake power increases.
- Rubber seed and moringa biodiesel power diesel engines effectively.
- MO20 increases NO_x by 20%, but both MO20 and RB20 reduce UBHC emissions.
- Using moringa oil methyl ester blends as a sustainable alternative to reduce pollution.
- The reduction in emissions is an important benefit of biodiesel.

Abstract

Energy resources are diminishing, and environmental problems are becoming more prevalent. In this regard, biodiesel from moringa oil (MO) and rubber seed oil (RSO) promises to be an excellent alternative to diesel fuels, while also requiring far less modification from existing diesel engines. Performance metrics analysis reveals that biodiesel consumes a slightly higher amount of fuel at lower loads because of its relatively lower calorific value. At 4.4 kW, MO methyl ester blend (MO20) achieved a brake thermal efficiency of 30%, outperforming diesel (26%) and RSO methyl ester blend (RB20) achieved a brake thermal efficiency of 28%. MO20 reduced CO emissions by 60% compared to diesel and 55% compared to RB20. Furthermore, MO20 increased NO_x emissions by 10% at higher brake power levels compared to RB20 and 20% for diesel. RB20 and MO20 biodiesel blends exhibit lower HC compared to diesel by 24% and 28% respectively. These reductions in carbon monoxide and hydrocarbon emissions make biodiesel blends, mostly from MO, cleaner and well sustainable compared to conventional diesel, with their environmental and performance benefits for diesel engine applications.

Keywords: Biodiesel, diesel engine, alternative fuel, moringa oil, rubber seed oil, emissions.

SCIENTIFIC PAPER

UDC 662.756.3:621.436.3

INTRODUCTION

Developing alternative energy sources is a primary priority to reduce fossil fuel use. These solutions must meet rising energy needs sustainably. One notable option is biodiesel, made from waste and non-edible oils. It can be combined with diesel fuel and used in diesel engines, especially those that use non-edible oils, as an eco-friendly alternative to mineral diesel. Diesel engines have thus become popular amongst most consumers in the automobile market for their improved fuel efficiency. However, the finite nature of fossil fuel reserves and the deepening crisis of the environment have prompted scientists to expand their gaze to other fuels that could supplant diesel without an attendant diminution of high performance. In this process, biodiesel, whose origin is related to fatty acid triglycerides, has become a potential candidate. In addition, because only minor modifications are required, diesel engines can be converted into clean, sustainable energy sources without compromising the efficiency of the engines.

Another alternative that can be used is rubber seed oil (RSO). It is a recyclable, environmentally friendly alternative fuel. Oil extracted from the seeds of the rubber tree, which is abyproduct of the latex industry, may help to reduce dependence on fossil fuel and support carbon sequestration. But both biodiesel and rubber esters face challenges as alternative fuels. Blending, pyrolysis, and emulsification increase vegetable oil viscosity. Research suggests that one method to improve. Transesterification gives oils and fats fuel characteristics [1,2]. One species that is frequently grown is *M. oleifera*, which is evergreen, grows quickly, and has deciduous leaves [3]. Due to its high

Correspondence: V. Subramanian and R. Palani, Department of Mechanical Engineering, Sri Venkateswara College of Engineering, Pennalur, Sriperumbudur -602 117, Tamil Nadu, India.
Email: venkyy1992@gmail.com, praghu@svce.ac.in
Paper received: 11 December, 2024
Paper revised: 27 April, 2025
Paper accepted: 24 June, 2025

https://doi.org/10.2298/CICEQ241211018P

viscosity, pure vegetable oil makes it difficult to atomize gasoline and causes the fuel spray to penetrate deeper into the material. Problems with engine deposits and lubricating oil thickening are partially caused by this greater penetration [4].

Biodiesel is a viable and environmentally sustainable alternative to traditional fossil fuels, especially petroleum-derived diesel [5-7]. Sustainable transition to renewable sources is a good way to mitigate climate change and ensure future generations can satisfy their energy demands [8-10].

Ozsezen and Canakci [10] revealed that waste palm oil methyl esters or canola oil methyl esters instead of diesel fuel decreased the brake power (BP) by 4-5% and boosted the brake specific fuel consumption (BSFC) by 9-10%. Methyl esters reduced CO by 59-67%, hydrocarbons (HC) by 17-26%, CO_2 by 5-8%, and smoke opacity by 56-63%. However, they increased NO_x emissions by 11-22% compared to diesel fuel across the speed range. Based on experiments, RSOMEs are a viable compression ignition engine fuel.

RSO with high FFA was successfully converted to biodiesel using a two-step transesterification process, yielding fuel with properties close to diesel [11]. Since exhaust emissions decreased, biodiesel's specific fuel consumption increased by less than 11.4%, which may be acceptable. Researchers found that biodiesel, alone or in blends, can power compression ignition outboard engines, providing an alternative to diesel [12]. It is readily accessible and can meet the escalating global energy demands [13-15]. Rajan and Pradeepraj [13] investigated engine performance with 1-hexanol fumigation utilizing Moringa biodiesel-diesel blend (MOBD). Compression ignition (CI) engine carburetoring of *n*-hexanol into the intake manifold was tested. It was shown that 10% *n*- hexanol fumigation enhanced MOBD25 brake thermal efficiency (BTE) by 1.08% compared to other diesel and other fumigation ratios. MOBD25 fumigated with 30% *n*- hexanol reduced NO_x and smoke by 36% and 38%. The result shows that 30% *n*-hexanol fumigation in the MOBD25 blend greatly decreased NO_x emissions with a BTE penalty. Rajaraman *et al.* [14] observed *M. oleifera* biodiesel (B20 and B100) blending and engine performance and exhaust emissions utilizing a direct injection CI engine at full load. The trials showed that *M. oleifera* blended fuel had worse thermal efficiency than standard diesel fuel due to its high viscosity, density, and reduced calorific value. Compared to diesel fuel, *M. oleifera* mixed fuel produced less PM, CO, HC, and NO_x [15]. The biodiesel production process involves an acid-catalyzed pretreatment followed by alkaline-catalyzed transesterification. The key properties of RSOMEs are compared with those of other esters and diesel fuel.

Ramalingam and Mahalakshmi [16] investigated biodiesel-diesel-1-hexanol (B-D-H) and *M. oleifera* biodiesel-diesel-ethanol (B-D-E) mixes using a compression ignition engine. Test results indicate B90-D5-H5 had the lowest BSFC and the greatest BTE, 0.375 kg kW^{-1} h^{-1} and 28.8%. His greatest NO_x emission was 1090 ppm in B80-D5-E15. B100 had the lowest NO_x of (846 ppm), maximum HC emissions (34 ppm) at 100% load, and lowest smoke opacity (34%). Unfortunately, biodiesel-diesel-alcohol mixtures enhanced engine performance but reduced emissions like normal diesel. Diesel usage decreases with biodiesel-diesel-alcohol mixtures. Thus, ethanol and 1-hexanol are the best blending diesel for fuel quality, performance, and emissions.

Rashed *et al.* [17] explore the performance and emissions of moringa biodiesel-fueled diesel engines compared to palm, jatropha, and diesel fuel. This article evaluated only 20% of each biodiesel in the diesel engine, even though open literature suggests using up to 20% without modification. Blended fuel reduces average CO and HC emissions, apart from NO_x, compared to diesel fuel. *M. oleifera* is commonly referred to as “behen oil” or “ben oil” due to its high content of behenic acid (docosanoic acid). These characteristics make *M. oleifera* oil suitable for biodiesel production [18]. There are numerous biodiesel feedstocks, including edible and non-edible oils (*Ceiba pentandra*, palm, *Jatropha curcas*, *Calophyllum inophyllum*, waste food oils) and animal fats (tallow and lard) [19-24]. Energy is essential for our daily lives, driving human development and fostering economic growth and productivity. Salaheldeen *et al.* [19] evaluated the performance, emissions, and combustion of diesel and RSO methyl esters (RSOMEs) blends in a direct injection diesel engine at 19°, 23°, and 27° 19°, 23°, and 27° bTDC. At 19° bTDC, RB20 had lower energy content and viscosity than diesel and moringa oil (MO), resulting in improved BTE and reduced specific fuel consumption. Diesel and RB20 had equivalent fuel usage and lower CO emissions. Advance injection timing boosted NO_x emissions, while retarding it improved fuel economy, HC and CO emissions, and RB20 thermal efficiency. Taguchi found a multi-response signal-to-noise ratio of 23 optimum. Biodiesel spray properties are theoretically analyzed in the study. Saravanan *et al.* [20] found that the crude rice bran oil methyl esters (CRBMEs) had a lower delay period and maximum pressure rise than diesel. The CRBME blend also released heat earlier than diesel, but the difference was smaller. According to Sivalakshmi and Balusamy [21], neem oil-alcohol blends improve the BTE. These blends reduce smoke, CO, and HC at higher loads. When compared to pure neem oil, the mixes eliminated NO_x emissions minimally, except for the ethanol blend.

Soudagar *et al.* [22] reported trans-esterification of *M. oleifera* oil to make biodiesel under working circumstances. B10 and B20 biodiesels are compared to high-speed diesel in a compression ignition engine for performance and emissions. Engine speed ranged from 1000 to 2400 rpm at full load. All performance and exhaust pollutant results were analyzed. MO10 produced 7.44%, 7.51%, and 7.7% reductions in the BP, BSFC, and CO_2. Smoke opacity and HC decreased 24% and 10.27% for MO10. MO10 has 2.5% and 9% higher CO and NO_x emissions than diesel. Tamilselvan *et al.* [23] published an extensive analysis of diesel engines that run on biodiesel, including their performance, combustion, and emission parameters. The current studies show that biofuels are the greatest way to enhance gasoline quality. Sustainable, oxygenate-free,

sulfur-free, and biodegradable biofuels are amazing. Biofuels are also a great option considering efficiency, as they could run on the existing diesel engines and do not require any adjustment whatsoever. Scientists have taken extreme and considerable tests on the diesel engine to prove their supremacy over standard fuels based on indicators of emissions and performance. In this article, pure biodiesel in the engine and the combustion of biodiesel with fuel will be thoroughly examined. This paper is a good study wherein biodiesel CO_2, CO, HC, and NO_x are utilized in a diesel engine. Venkanna and Reddy [24] demonstrated that warmed honne oil improves BTE and exhaust gas temperature (EGT). Preheated honne oil emits more NO_x than unheated, although emissions of SO, CO, and HC are lower.

The global use of biodiesel is steadily increasing as countries seek sustainable alternatives to fossil fuels and aim to reduce environmental pollution. Biodiesel derived from renewable sources not only lowers greenhouse gas emissions but also enhances energy security [25]. Among emerging feedstocks, RSO and MO show strong potential for widespread adoption, especially in regions with rich agricultural resources. This study investigates the performance and emission characteristics of RB20 and MO20 blends, emphasizing their suitability for large-scale application as clean, efficient substitutes for conventional diesel [26,27]. While studies have highlighted the potential of biodiesel blends MO20 and RB20 in improving engine performance and reducing emissions, there is limited research comparing these blends in terms of long-term performance, engine durability, and optimal blend ratios. Further studies are needed to explore the feasibility of these biodiesels as sustainable alternatives to diesel under varying operational conditions.

The twin challenges of the world are fossil fuel depletion and environmental pollution. Increasing costs and depleting hydrocarbon reserves require alternative fuels to fulfill growing energy needs and reduce environmental damage. The present study examined MO methyl esters (MOMEs) and RSOMEs blends (MO20 and RB20) as biodiesel alternatives. This study highlights the potential of MO20 and RB20 biodiesel blends as sustainable alternatives to conventional diesel. The research demonstrates that these biodiesel blends improve engine performance as the brake power (BP) increases. Notably, MOME blends reduce NO_x emissions by 20% compared to diesel, offering a significant environmental benefit. These findings underscore the role of biodiesel in reducing emissions, making it a promising solution for cleaner, more efficient fuel use in diesel engines.

MATERIALS AND METHODS

Fuel Preparation

MO was extracted from the seeds of the *M. oleifera* plant through cold-pressing. The extracted oil underwent a two-step transesterification process. First, an acid-catalyzed pretreatment was conducted using sulfuric acid to reduce the high FFA content below 1%. Subsequently, a base-catalyzed transesterification was performed using methanol (molar ratio of 6:1) and sodium hydroxide (NaOH) as a catalyst at 60 °C for 1.5 hours. After the reaction, the mixture was allowed to settle in a separating funnel, leading to two distinct layers: biodiesel (upper layer) and glycerol (lower layer). The biodiesel layer was washed with warm distilled water to remove residual catalyst and methanol and then dried at 110 °C to eliminate moisture, yielding MOME.

RSO was obtained from rubber tree seeds (*Hevea brasiliensis*) through mechanical expeller pressing. Due to the higher free fatty acid (FFA) content in raw RSO, a similar two-step esterification method was used. Initially, the oil was treated with sulfuric acid and methanol to reduce the FFA level. The second stage involved base-catalyzed transesterification using methanol (molar ratio of 6:1) and potassium hydroxide (KOH) as a catalyst, maintaining a reaction temperature of 60 °C for 2 hours. The resulting mixture was separated into biodiesel and glycerol layers. The biodiesel was washed thoroughly with warm water and dried to achieve a pure RSO methyl ester. After confirming that both biodiesel samples met ASTM D6751 fuel standards, they were blended with mineral diesel at a ratio of 20% biodiesel to 80% diesel by volume to prepare MO20 and RB20 blends. *M. oleifera* is known for its high oil content and ability to reduce emissions, particularly NO_x, while RSO is widely available as a by-product of the rubber industry, making it a cost-effective and sustainable option. Both oils have shown promising results in previous studies for their fuel properties and environmental benefits, which motivated their inclusion in this research. The goal was to compare these biodiesel blends for their potential to improve engine performance and reduce harmful emissions when used in existing diesel engines. These blends were used for engine testing without any modification to the diesel engine. Table 1 shows the tested properties of Diesel, MO20, and RB20.

Experimental technique

The experimental investigation was carried out using a single-cylinder, four-stroke, water-cooled, naturally aspirated, direct injection (DI) diesel engine rated at 4.4 kW at 1500 rpm, as shown in Figure 1. The engine was coupled to an eddy current dynamometer equipped with a digital torque indicator and load control mechanism for precise loading conditions. A fuel measurement system consisting of a burette and a stopwatch was used to measure the fuel consumption by recording the time taken for a fixed volume of fuel. An AVL 444 Digas gas analyzer was used to measure exhaust gas emissions, including CO, HC, and NO_x. The specification of the emission measurement instrument is represented in Table 2. For combustion analysis, an AVL indimeter system, incorporating an in-cylinder pressure transducer (AVL GH12D), crank angle encoder, and data acquisition system, was employed to monitor the cylinder pressure variation, rate of heat release, and ignition delay. The cooling water flow rate was maintained constant to ensure consistent operating temperatures. Prior to each test, the engine was warmed up for 20 minutes to reach steady-state conditions. Fuel tanks were cleaned before switching fuels to prevent

Table 1. Properties of pure oils, pure biodiesels, blends, and diesel.

Property	MO	RSO	MOME	RSOME	MO20 blend	RB20 blend	Diesel
Density at 20 °C, (kg/m³)	910	920	870	880	842	882	840
Calorific value (kJ/kg)	39.000	38.500	42.000	41.800	42.460	41.522	43.000
Specific gravity	0.91	0.92	0.87	0.88	0.90	0.91	0.84
Viscosity (cSt)	35.6	32.4	5.5	5.8	3.6	5.2	2.5-3.2
Flash point (°C)	220	210	170	160	84	125	65
Fire point (°C)	240	230	190	180	92	152	78
Cetane number	47	45	52	50	64	43	45-55

Table 2. Specification of the emission measurement instruments.

Instrument name	Measured emissions	Model	Manufacturer	Measurement range	Accuracy
AVL DiGas 444 Analyzer	CO, HC, NO_x	DiGas 444	AVL, Austria	CO: 0-10%, HC: 0-20,000 ppm, NO_x: 0-5000 ppm	±1% of full-scale reading

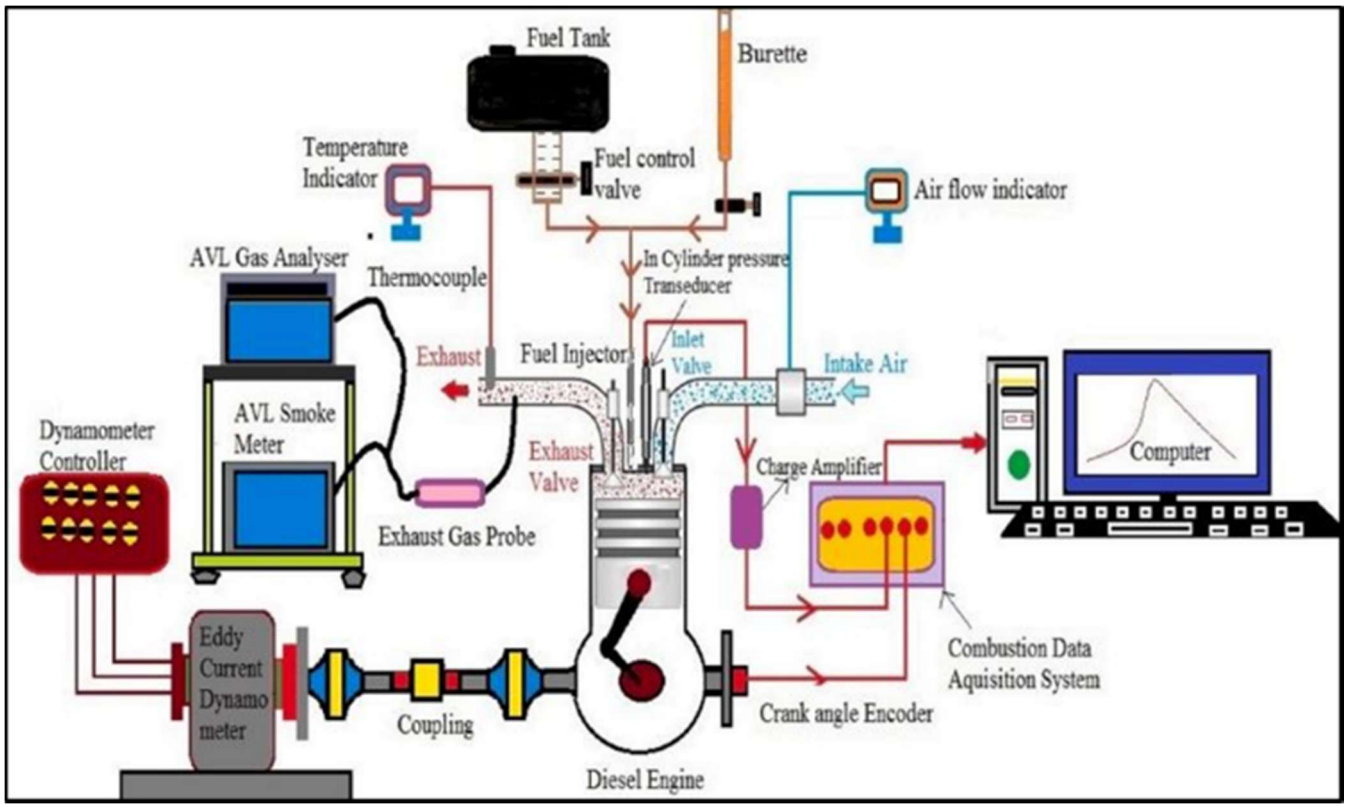

Figure 1. Experimental setup.

contamination. The baseline readings were first recorded using neat diesel fuel, followed by testing with MO20 and RB20 blends under identical loading conditions. All experiments were conducted at a constant engine speed of 1500 rpm, varying the load incrementally from no load to full load in steps, and measurements were repeated three times to ensure repeatability. The ambient temperature and barometric pressure were also recorded during testing to account for environmental influences. Uncertainty analysis was performed for the experimental measurements and found to be within acceptable limits: ±2.1% for the BTE, ±2.0% for the BP, and ±2.11% for the BSFC. Emission measurements had uncertainty levels of ±0.1% for CO, ±5 ppm for HC, and ±0.11% for NO_x. A computer processed the data, including parameters like power output, torque, and fuel consumption, while an AVL combustion analyser measured the rate of heat release and emissions (including NO_x, CO, and HC [12].

Test Methodology

The engine's maximum torque was initially estimated, and it was then started under no-load conditions using a hand crank with the decompression lever activated. After initiating the engine, it was allowed to run under no-load conditions for several minutes to ensure that the speed stabilized at its rated value. The engine was then operated at a constant speed while monitoring fuel consumption, utilizing a time indicator calibrated for a 10-cc fuel quantity. An eddy current dynamometer was employed to conduct experiments under variable load conditions. Testing was performed using biodiesel, and the results were meticulously recorded. This procedure was replicated

under identical operating conditions for all fuel blends tested, including diesel and biodiesel blends of MO20 and RB20. The exhaust gas temperature was measured under the same operating conditions for each blend in the range of 350-400 °C for low load to full load. To ensure the experiment's accuracy, uncertainty analysis is necessary. At 0.7%, 0.18 s, and 2.01 of fuel, time, and braking power testing were accurate. A digital dynamometer (accuracy ±0.1%) was employed for the BP measurement, and a calibrated gas analyzer (accuracy ±2%) was used for emission parameters such as CO, HC, and NO_x. All instruments were calibrated before testing according to the manufacturer's guidelines. This systematic approach highlights the relevance and precision of the measurement tools and strengthens the credibility of the reported data. The BSFC of +2.11, the BP of +2.01, and the BTE of +2.10 uncertainties were computed using root-sum-square measurement. The uncertainty on measured exhaust emission values was estimated using the measuring range and resolution of the instrument for each emission component, and the values were CO = +0.1%, HC = +0.005%, and NO_x = +0.00011%, respectively. MOMEs and RSOMEs were selected according to Rajaraman *et al.* [14].

RESULTS AND DISCUSSION

The experimental results for engine performance and emissions characteristics using diesel, MO20, and RB20 fuel blends are presented and discussed in this section. Key performance indicators such as the BSFC and BTE are evaluated, along with critical emission parameters including CO, HC, and NO_x. The discussion highlights the influence of biodiesel blends on engine behavior under varying load conditions, comparing their performance against conventional diesel fuel. RB20 and MO20 biodiesel blends suggest a strong potential for real-world applications. These blends can be used in existing diesel engines with minimal modifications, promoting a smoother transition toward renewable fuels. However, practical challenges must be considered before large-scale adoption. Issues such as fuel stability over long storage periods, the slightly higher viscosity of biodiesel blends, cold flow properties in colder climates, and the current limitations in large-scale production and supply infrastructure may affect widespread use. The findings reveal that biodiesel blends, particularly MO20, can enhance engine efficiency and significantly reduce pollutant emissions, offering a promising alternative to fossil diesel in compression ignition engines.

Performance Characteristics

Consideration of engine performance, as measured by metrics like the BSFC and BTE, is crucial for determining fuel economy. BSFC as a function of the BP is illustrated in Figure 2 for diesel, biodiesel blends (RB20 and MO20), and other fuels. An integral part of the BSFC is the fuel characteristics, including density, viscosity, and heating value.

Figure 2 clearly shows that for all three fuels, the BSFC generally reduces as the BP increases. But the rate at which BSFC declines differs depending on the fuel. When the BP increases, diesel fuel shows the largest reduction in BSFC, whereas RSO and MO show noticeably slower rates of improvement. More specifically, over the whole BP range, MO exhibits a somewhat greater BSFC than diesel. This implies that there may be a slight decrease in fuel efficiency when using moringa biodiesel instead of diesel. One of the most notable findings is how RSO performs. At a low BP, RSO has a somewhat higher BSFC than diesel, but at higher BP levels, it converges with diesel and even exceeds it. For instance, at 1 kW of BP, the BSFC for diesel is approximately 160 g/kWh, while it is higher for RSO(180 g/kWh) and MO (190 g/kWh). However, at 4.4 kW, the BSFC for RSO and diesel converges around 100 g/kWh, suggesting improved fuel efficiency for RSO at higher power levels. BSFC was higher for biodiesel blends (RB20 and MO20) because of higher densities and viscosities are higher and energy densities are lower than diesel fuel. One major reason why fuel atomization is slower in MO20 and RB20 blends is because of their higher viscosity, which in turn leads to poor air-fuel mixing. Soudagar *et al.* [22] reported similar outcomes.

Diesel and biodiesel mixes (RB20 and MO20) are illustrated in Figure 3 along with the relationship between braking power and the BTE. The BTE tends to rise in conjunction with the BP for all three fuels, as seen in Figure 3. This suggests a positive correlation between power production and the efficiency of transferring fuel energy into mechanical work. The fuel economy that increases with increasing BP is highest for diesel, and the rates of improvement are noticeably lower for biodiesel blends (RB20 and MO20). More specifically, RSOME blends show a somewhat poorer BTE over the whole BP range as compared to diesel. It implies that a tiny amount of biodiesel added may cause a slight decrease in fuel efficiency. The performance of MO is possibly the most remarkable finding. At a low BP, MO's BTE is marginally lower than diesel's, but as the BP increases, it converges with diesel and even outperforms it. For all fuels, including diesel and biodiesel mixes (RB20 and MO20), the BTE increases as braking power increases. For instance, at 2 kW, diesel exhibits a BTE of 25%, while MO is slightly lower, at 23%. As the BP reaches 4 kW, MO surpasses diesel, achieving 30% efficiency compared to diesel's 28%. A decrease in the BTE is a negative effect, related to energy content and fuel consumption when the fuel is changed [22].

Emission Characteristics

Figure 4 shows the correlation between CO emissions and the BP for three distinct fuel types: diesel, biodiesel blends (RB20 and MO20). Figure 4 shows the CO emissions for all diesel, biodiesel blends (RB20 and MO20). CO emissions of all three fuels generally increase as the BP increases. The rate of rise, however, differs greatly throughout the fuels. When the BP increases, diesel fuel shows the highest increase in CO emissions, while biodiesel blends (RB20 and MO20) show noticeably lower emissions. At maximum BP levels, RB20 exhibits a significant decrease in CO emissions relative to diesel. This suggests that adding a small quantity of biodiesel to diesel fuel can significantly reduce emissions. The way that MO20

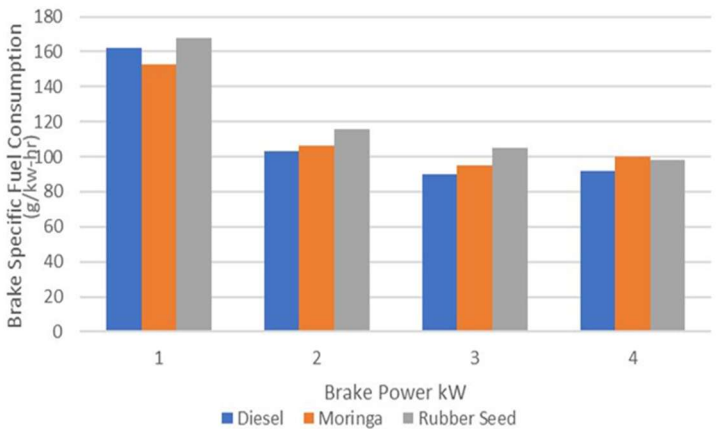

Figure 2. Relationship between the BP with the BSFC for diesel and biodiesel blends (RB20 and MO20).

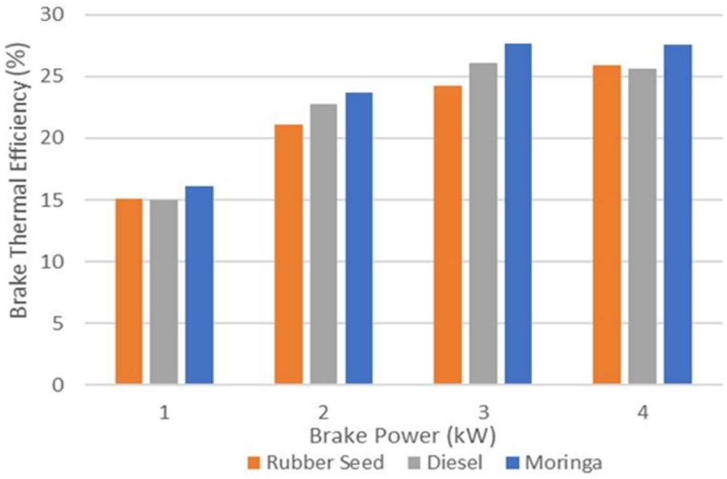

Figure 3. Relationship between the BTE with the BP for diesel and biodiesel blends (RB20 and MO20)

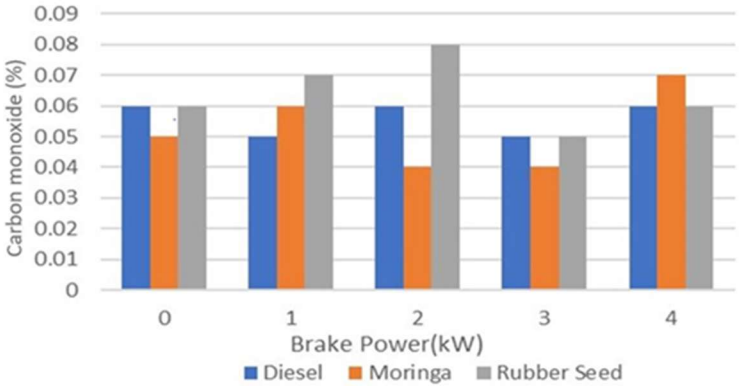

Figure 4. Relationship between CO emission with the BP for diesel and biodiesel blends (RB20 and MO20).

performs is possibly the most remarkable finding. MO20 consistently emits substantially less CO than both diesel and RB20 over all BPs. MO20 and RB20 biodiesel blends have more oxygen and cetane than diesel fuel. Especially with oxygen-rich biodiesel, higher cylinder pressure and temperature facilitate full combustion [9]. This suggests that biodiesel blends might greatly reduce air pollution, particularly CO_2, if used as a fuel.

The BP and UBHC emissions of diesel and MO20 and RB20 biodiesel blends are shown in Figure 5, which clearly shows that for all three fuels, unburned hydrocarbon emissions normally increase with increasing BP. Nonetheless, there are notable differences in the pace of rise among the fuels. When the BP increases, UBHC emissions from diesel fuel rise at the fastest rate, while emissions from RB20 and MO20 fuels are noticeably lower. For instance, RSOME blends exhibit a moderate decrease in emissions of UBHC as compared to diesel, especially at higher BP levels. Reduced HC emissions compared to diesel at rated speed are often the result of better fuel combustion made possible by the oxygen content of MO20 and RB20 [5].

Figure 6 indicates that for all three fuels, NO_x emissions typically increase with the increase in the BP for diesel, RB20, and MO20. The rate of rise, however, shows significant variations throughout the fuels. Diesel fuel is indicated to present the biggest increase of NO_x emissions with the increment in the BP, whereas biodiesel blends, such as RB20 and MO20 fuels, present noticeably lower emissions. More particularly, for a higher BP, NO_x emissions are moderate for RB20 with respect to diesel. NOx emissions also significantly increase with MO20, resulting in a 20% increase in NOx emissions as compared to diesel and a 10% rise in RB20. MOME blends continuously produce significantly less amount of NOx emissions compared to RSOMEs and diesel in the entire range of the BP. It implies that biodiesel blends as fuels can produce a drastic reduction in air pollution, especially concerning NOx. Figure 6 concludes with the fact that biodiesel blends, especially MO biodiesel blends, provide an effective means of reducing the emissions of NOx from diesel engines. Higher NOx emissions for biodiesel blends are due to higher viscosity and density, and have a high cetane number. One major reason why fuel atomization is slower in MO20 and RB20 blends is because of their higher viscosity, which in turn leads to poor air-fuel mixing. The oxygen concentration of *M. oleifera* biodiesel is higher than that of neat diesel fuel. Furthermore, the content of Furthermore, the content of biodiesel in fuel blends is directly correlated to the rise in NO_x emissions. Also, Ozsezen and Canakci [10] reported similar outcomes.

CONCLUSIONS

The research findings strongly indicate that biodiesel, especially from RSO and MO, is a feasible alternative to conventional diesel. The performance characteristics reveal that BSFC for both biodiesel blends (MO20 and RB20 initially

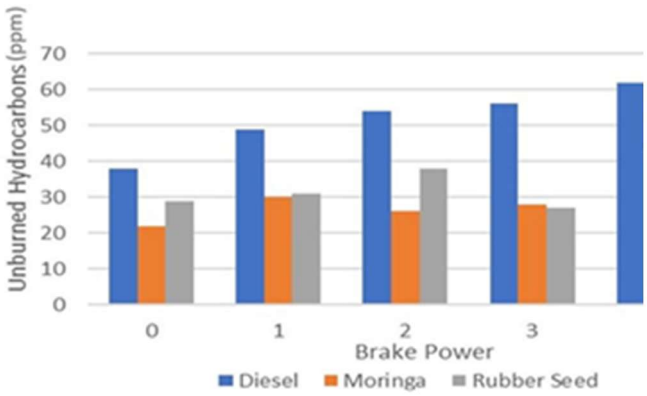

Figure 5. Relationship between HC emission with the BP for diesel and biodiesel blends (RB20 and MO20).

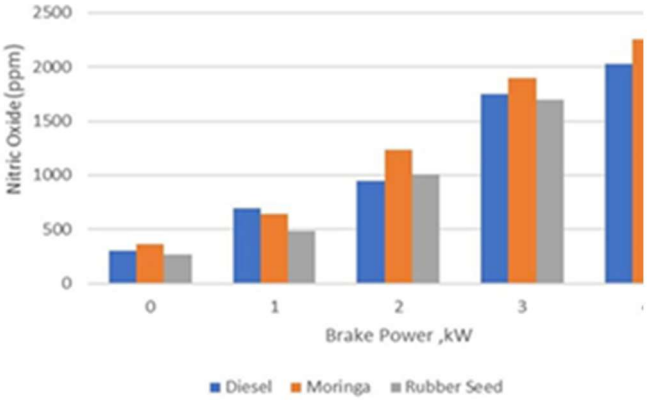

Figure 6. Relationship between NO_x emission with the BP for diesel and biodiesel blends (RB20 and MO20).

exceeds diesel, but as the BP increases, their efficiencies improve. From an environmental standpoint, the reduction in emissions is a significant advantage of biodiesel. CO emissions are markedly lower with biodiesel blends. Diesel emissions are around 0.08% by volume, while MOME blends (MO20) emit significantly less at 0.03%. NO_x emissions also show a substantial increase with MOME blends, producing a 20% rise in NO_x than diesel at a 4 kW of BP. The substantial reductions in harmful emissions, such as up to 60% less CO and 20% more NO_x emissions with MOME blend (MO20) compared to RB20 diesel, RB20 and MO20 biodiesel blends, exhibit lower UBHC emissions compared to diesel by 24% and 28% underscore the environmental benefits. This data is critical for policymakers, manufacturers, and consumers aiming to balance fuel economy with environmental responsibility. Future research should focus on optimizing the blend ratios of RSO and MO biodiesel to further enhance the engine performance and emission characteristics. Detailed studies on specific emissions such as particulate matter, NO_x formation, and after-treatment technologies could provide deeper insights. Additionally, long-term engine durability tests and investigations under varied climatic conditions would be valuable to ensure the practical viability of these biodiesel blends on a larger scale. These findings support the potential of biodiesel, especially MOME blends, as a sustainable alternative for reducing pollution while maintaining competitive engine performance.

Acknowledgments

It is our pleasure to acknowledge the assistance provided to us by the management of Sri Venkateswara College of Engineering in developing the experimental setup that we needed to carry out this research.

Abbrevations

BP - Brake power

BSFC - Brake specific fuel consumption

BTE - Brake thermal efficiency

BTDC - Before top dead center

CRBME - Crude rice bran oil methyl esters

D5 - 5% diesel in a biodiesel blend

EGT - Exhaust gas temperature

E15 - 15% ethanol and 85% gasoline or diesel

H5 - 5% Hexanol in the fuel blend.

HC - Hydrocarbon

MO - Moringa oil

MOB - Moringa oil biodiesel I

MOBD25 - 25% moringa oil methyl esters blended with diesel fuel

MOME - Moringa oil methyl esters

MO20 - 20% Moringa oil methyl esters blended with diesel fuel

PBDF - Petroleum-based diesel fuel

PM - Particulate matter

RB - Rubber seed oil biodiesel

RSOME - Rubber seed oil methyl esters

REFERENCES

[1] N.R. Abdullah, M.S.M. Zaharin, A.M.I. Mamat, M.R.M. Nawi, H. Sharudin, J. Technol. 76(11) (2015) 107-112. https://doi.org/10.11113/jt.v76.5920.

[2] D. Agarwal, A.K. Agarwal, Appl. Therm. Eng. 27(13) (2007) 2314-2323. https://doi.org/10.1016/j.applthermaleng.2007.01.009.

[3] A.K. Azad, M.G. Rasul, M.M.K. Khan, S.C. Sharma, R. Islam, Procedia Eng. 105 (2015) 601-606. https://doi.org/10.1016/j.proeng.2015.05.037.

[4] S.C.A. De Almeida, C. Rodrigues Belchior, M.V.G. Nascimento, L. Dos, S.R. Vieira, G. Fleury, Fuel 81(16) (2002) 2097-2102. https://doi.org/10.1016/S0016-2361(02)00155-2.

[5] F. Hussain, M.E.M. Soudagar, A. Afzal, M.A. Mujtaba, I.M. Rizwanul Fattah, B. Naik, B.M.H. Mulla, I.A. Badruddin, T.M. Yunus Khan, V.D. Raju, R.S. Gavhane, S.M. Ashrafur Rahman, Energies 13(17) (2020) 4578. https://doi.org/10.3390/en13174578.

[6] S. Jindal, B.P. Nandwana, N.S. Rathore, V. Vashistha, Appl. Therm. Eng. 30(5) (2010) 442-448.https://doi.org/10.1016/j.applthermaleng.2009.10.004.

[7] V. Karthickeyan, Fuel 235 (2019) 538-550. https://doi.org/10.1016/j.fuel.2018.08.030.
[8] B. Kathirvelu, S. Subramanian, Environ. Eng. Res. 22 (2017) 294-301. https://doi.org/10.4491/eer.2016.145.
[9] S. Murillo, J.L. Miguez, J. Porteiro, E. Granada, J.C. Moran, Fuel 86 (2007) 1765–1771. https://doi.org/10.1016/j.fuel.2006.11.031.
[10] A.N. Ozsezen, M. Canakci, Energy Convers. Manage. 52 (2011) 108-116. https://doi.org/10.1016/j.enconman.2010.06.049.
[11] A.S. Ramadhas, S. Jayaraj, C. Muraleedharan, Renew. Energy 30 (2005) 795-803. https://doi.org/10.1016/j.renene.2004.07.002.
[12] P. Raghu, R. Sundarrajan, R. Rajaraman, M. Ramaswamy, S. Sathyanaryanan, Int. J. Veh. Struct. Syst. 12 (2020) 82. https://doi.org/10.4273/ijvss.12.1.18.
[13] K. Rajan, R. Pradeepraj, Int. J. Innov. Technol. Explor. Eng. 9 (2020) 1783–1786. https://doi.org/10.35940/ijitee.B7242.019320.
[14] S. Rajaraman, G.K. Yashwanth, T. Rajan, R. Siva Kumaran, P. Raghu, Proc. ASME Int. Mech. Eng. Congr. Expo. 2009 Volume 3: Combustion Science and Engineering, 13–19, (2009) pp. 27-34. https://doi.org/10.1115/IMECE2009-11265.
[15] A.S. Ramadhas, C. Muraleedharan, S. Jayaraj, Renewable Energy 30 (2005) 1789–1800. https://doi.org/10.1016/j.renene.2005.01.009.
[16] S. Ramalingam, N.V. Mahalakshmi, RSC Adv. 10 (2020) 4274-4285. https://doi.org/10.1039/c9ra09582a.
[17] M.M. Rashed, M.A. Kalam, H.H. Masjuki, M. Mofijur, M.G. Rasul, N.W.M. Zulkifli. Ind. Crops Prod. 79 (2016) 70-76. https://doi.org/10.1016/j.indcrop.2015.10.046.
[18] U. Rashid, F. Anwar, B.R. Moser, G. Knothe, Bioresour. Technol. 99 (2008) 8175-8179. https://doi.org/10.1016/j.biortech.2008.03.066.
[19] M. Salaheldeen, M.K. Aroua, A.A. Mariod, S.F. Cheng, M.A. Abdelrahman, A.E. Atabani, Energy Convers. Manage. 92 (2015) 535-542. https://doi.org/10.1016/j.enconman.2014.12.087.
[20] S. Saravanan, G. Nagarajan, G. Lakshmi Narayana Rao, S. Sampath, Energy 35 (2010) 94-100. https://doi.org/10.1016/j.energy.2009.08.029.
[21] S. Sivalakshmi and T. Balusamy, Int. J. Ambient Energy 32 (2011) 170-178. https://doi.org/10.1080/01430750.2011.625717.
[22] M.E.M. Soudagar, H.M. Khan, T.M. Yunus Khan, L. Razzaq, T. Asif, M.A. Mujtaba, A. Hussain, M. Farooq, W. Ahmed, K. Shahapurkar, A. Alwi, T.M. Ibrahim, U. Ishtiaq, A. Elfasakhany, M.A.A. Baig, M.S. Goodarzi, M.R. Safaei, Appl. Sci. 11 (2021) 7071. https://doi.org/10.3390/app11157071.
[23] P. Tamilselvan, N. Nallusamy, S. Rajkumar, Renew. Sustain. Energy Rev. 79 (2017) 1134–1159. https://doi.org/10.1016/j.rser.2017.05.176.
[24] B.K. Venkanna, C.V. Reddy, Int. J. Energy Technol. Policy 9 (2013) 1-14. https://doi.org/10.1504/IJETP.2013.055813.
[25] A.K. Agarwal, Renew. Sustain. Energy Rev. 150 (2022) 111551. https://doi.org/10.1016/j.rser.2021.111551.
[26] A. Demirbas, Energy Convers. Manag. 226 (2021) 113528. https://doi.org/10.1016/j.enconman.2020.113528.
[27] U. Rashid, Bioresour. Technol. 351 (2022) 126891. https://doi.org/10.1016/j.biortech.2022.126891.

VENKATESAN SUBRAMANIAN

RAGHU PALANI

Department of Mechanical Engineering, Sri Venkateswara College of Engineering,

Tamil Nadu, India.

UPOREDNA ANALIZA BIODIZELA IZ ULJA MORINGE I ULJA KAUČUKOVOG SEMENA U DIZEL MOTORIMA

Energetski resursi se smanjuju, a ekološki problemi postaju sve rasprostranjeniji. U tom smislu, biodizel iz ulja moringe (MO) i ulja kaučukovog semena (RSO) obećava da će biti odlična alternativa dizel gorivima, a istovremeno zahteva daleko manje modifikacije u odnosu na postojeće dizel motore. Analiza performansi otkriva da je potrošnja biodizela nešto veća pri manjim opterećenjima zbog svoje relativno niže kalorijske vrednosti. Pri 4,4 kW, mešavina metil-estara MO (MO20) postigla je termičku efikasnost kočenja od 30%, nadmašujući dizel (26%), dok je mešavina metil-estra RSO (RB20) postigla termičku efikasnost kočenja od 28%. MO20 je smanjila emisiju CO_2 za 60% u poređenju sa dizelom i 55% u poređenju sa RB20. Međutim, MO20 je povećala emisiju NO_x za 10% i 20% pri višim nivoima snage kočenja u poređenju sa RB20 i dizelom, redom. Mešavine biodizela RB20 i MO20 pokazuju niži sadržaj ugljen-monoksida u poređenju sa dizelom za 24% i 28% redom. Ova smanjenja emisija ugljen-monoksida i ugljovodonika čine mešavine biodizela, uglavnom iz MO, čistijim i održivije u poređenju sa konvencionalnim dizelom, sa njihovim ekološkim i performansnim prednostima za primenu u dizel motorima.

Ključne reči: Biodizel, dizel motor, alternativno gorivo, ulje moringe, ulje kaučukovog semena, emisije.

NAUČNI RAD

CI&CEQ
Chemical Industry & Chemical Engineering Quarterly

Available online at
Association of the Chemical Engineers of Serbia AChE
www.ache.org.rs/CICEQ

Chem. Ind. Chem. Eng. Q. 32 (2) 153–162 (2026) CI&CEQ

MAHA ABDELILEH[1]

MANEL BEN TICHA[2]

NIZAR MEKSI[1,3]

HATEM DHAOUADI[1]

[1]University of Monastir, Faculty of Sciences of Monastir, Research Laboratory of Environmental Chemistry and Clean Processes, Tunisia.

[2]Department of Early Childhood, University College of Turabah, Taif University, Saudi Arabia

[3]University of Monastir, National Engineering School of Monastir, Department of Textile, Tunisia.

SCIENTIFIC PAPER

UDC 677.027.4:547.978.66.021.4

APPLYING DENSITY FUNCTIONAL THEORY TO PREDICT THE REDUCTION POTENTIAL IN THE INDIGO DYEING PROCESS

Highlights

- Experimental results were assessed using redox potential and color strength.
- E_{HOMO} values showed iron(II) gluconate had the highest electron-donating power.
- Complexation energy calculations matched well with experimental dyeing results.
- DFT efficiently predicted the reducing power of organic iron(II) salts.

Abstract

This study employs density functional theory (DFT) to quantify the electron donor-acceptor properties and polarizability of organic iron(II) salts as reducing agents in indigo dyeing processes. The potential of some iron(II) salts to serve as environmentally friendly alternatives to the ecologically harmful sodium dithionite in the indigo dyeing process was investigated. A comparative analysis assessed the redox potential of reduced indigo and the color strength of dyed fabrics. Experimental results identified iron(II) gluconate as the most efficient, yielding superior color intensity. Theoretical calculations using B3LYP/LANL2DZ confirmed the superior electron-donating ability of iron(II) gluconate compared to the other iron(II) salts. The indigo reduction ability with the iron(II) salts was evaluated on the basis of complexation energies. The theoretical thermodynamic study reveals that the indigo-iron(II) gluconate complex is the most thermodynamically stable, requiring less energy input for its formation compared to the other complexes. Iron(II) salts-to-indigo electron donations in the complexes studied have been revealed by Mulliken charge analysis. These findings highlight the efficiency of DFT-based approaches in accurately predicting the reducing capacity of iron(II) salts and their suitability as eco-friendly alternatives in indigo dyeing applications.

Keywords: Indigo dyeing; iron(II) salts; DFT calculations; experimental results, complexation energy.

INTRODUCTION

Indigo dyeing is a widely used process in the textile industry, known for its distinctive blue color and durability. In this process, the initially insoluble dye needs to be reduced into its leuco-soluble form, which exhibits an affinity for cellulosic fibers. Once indigo penetrates the fiber, it is fixed by regenerating its initial insoluble form, typically through oxidation with air. Currently, the majority of indigo dyeing processes rely on sodium dithionite as a reducing agent [1]. However, this chemical compound poses several challenges. Sodium dithionite is highly flammable, demanding special storage precautions, and exhibits poor stability [2]. Furthermore, its oxidation results in the production of sulfates, sulfites, thiosulfates, and toxic sulfides, all of which have detrimental toxic effects on the environment and corrosive impacts on waste lines. The decomposition of sodium dithionite also affects aerobic processes during wastewater treatment [3]. Consequently, there is an urgent need to identify eco-friendly alternatives that maintain or improve the efficiency of the dyeing process while reducing environmental impact.

Numerous environmentally friendly reducing agents were explored as alternatives to sodium dithionite, such as sodium borohydride [4,5] and α-hydroxycarbonyls (e.g., glucose, hydroxyacetone) [6]. While these compounds align with environmental standards, they fall short in terms of dyeing performance compared to sodium dithionite.

Iron(II) complexes were extensively employed for the chemical reduction of indigo [7,8]. A recent consideration

Correspondence: M. Abdelileh, University of Monastir, Faculty of Sciences of Monastir, Research Laboratory of Environmental Chemistry and Clean Processes, 5000Monastir, Tunisia.
Email: maha.abdelileh@gmail.com
Paper received: 17 March 2025
Paper revised: 3 June 2025
Paper accepted: 3 July 2025

https://doi.org/10.2298/CICEQ250317020A

involves the use of ecological enzymes in combination with iron(II) sulfate as a reducing agent for indigo dyeing. The efficiency of several enzymes, such as alkaline catalase and alkaline protease combined with iron(II) sulfate in the indigo reduction and solubilization was also studied [9]. Dyeing performance with this approach demonstrated comparability with that achieved using sodium dithionite [10].

Density functional theory (DFT) has become one of the most powerful computational tools for understanding and predicting the electronic properties and chemical reactivity of molecules. In particular, DFT is highly effective in studying systems where electron transfer and donor-acceptor interactions are fundamental [11]. These interactions are important in various chemical and biological processes, such as charge transport in organic semiconductors, redox reactions in electrochemistry [12], and energy transfer in photovoltaic materials [13]. A thorough survey of the literature reveals a significant gap in studies utilizing DFT to explain the reduction mechanism of indigo. While extensive research has been conducted on the dyeing properties, redox behavior, and reduction of indigo using conventional chemical and electrochemical methods, there is a notable absence of computational investigations that employ DFT to elucidate the electronic and molecular factors governing its reduction process.

This paper presents a novel and unique feature in indigo dyeing processes by combining experimental reduction and dyeing experiments with DFT. The capacity of iron(II) gluconate (E 574), iron(II) lactate (E 585), and iron(II) fumarate to reduce indigo was studied and compared to that of conventional sodium dithionite. These ferrous compounds, commonly used as food additives and dietary supplements, are notable for their low toxicity and biocompatibility. The organic iron(II) salts used are considered environmentally friendly as they undergo oxidation to ferric compounds during the dyeing process. These ferric compounds can act as flocculants, promoting the aggregation and subsequent removal of suspended solids and dye residues during wastewater treatment. This dual role as reducing agents and facilitators of effluent purification makes them attractive, sustainable alternatives to the conventional sodium dithionite reducing agent. Their use supports cleaner production practices and aligns with circular economy principles in textile manufacturing. DFT was used to quantify the electron donor-acceptor character and the polarizability of organic iron(II) salts. In order to quantify the reducing power of iron(II) salts and their efficiency in the dyeing process, the complexation energies between the reducing agents and indigo molecules were calculated. The effectiveness of DFT was evaluated by comparing the predicted interaction energy values with the obtained redox potential values and the color strength of the dyed samples.

EXPERIMENTAL

Chemicals and Materials

The chemicals used were: Sodium hydroxide (NaOH ≥ 99%, Loba Chemie, Germany), iron(II) gluconate dihydrate ($C_{12}H_{22}FeO_{14}$, Sigma-Aldrich, USA), iron(II) lactate ($C_6H_{10}FeO_6$ ≥ 98%, Sigma-Aldrich, Spain), iron(II) fumarate ($C_4H_3FeO_4$ ≥ 95%, Sigma-Aldrich, Spain).

Dyeing experiments using indigo powder ($C_{16}H_{10}N_2O_2$, Benzema, Switzerland) were performed on 100% bleached cotton fabric with the following specifications: plain weave structure, a fabric weight of 173 $g \cdot m^{-2}$, warp count of 25 yarns cm^{-1}, and weft count of 31 yarns cm^{-1}.

Indigo Reduction process

The reduction of indigo by organic iron(II) salts was conducted using 2 $g \cdot L^{-1}$ of indigo, 15 $g \cdot L^{-1}$ of sodium hydroxide, and a reducing agent concentration of 0.02 $mol \cdot L^{-1}$ at 75 °C for 120 min. The dye bath was prepared and subsequently placed in an AHIBA dyeing autoclave. Once the reduction temperature reached 75° C, the reducing agent was introduced to the dye bath. After 120 min, the redox potential was measured using a pH meter (pHM210) equipped with a platinum electrode and a reference electrode (Ag/AgCl, 3KCl). The reduced dye bath was then utilized for dyeing experiments following the 6-dip-6-nip method.

To compare the dyeing results achieved with iron(II) salts with those of conventional methods, a series of tests employing sodium dithionite as a reducing agent were conducted. These tests adhered to the guidelines of the traditional process used at an industrial scale. Typically, the dye bath contains 2 $g \cdot L^{-1}$ of indigo, 4 $g \cdot L^{-1}$ of sodium hydroxide, and 4 $g \cdot L^{-1}$ of sodium dithionite, maintained at a temperature of 50 °C [14].

Dyeing process

Cotton samples were dyed using the 6-dip/6-nip impregnation process. Each cycle (1 dip-1 nip) consisted of immersing the fabric in the dye bath for 1 minute, followed by aeration for approximately 2 minutes. This process was repeated six times. After dyeing, the samples were thoroughly washed with tap water and dried at room temperature.

Color strength measurement

Dyed samples were estimated by measuring the color strength (K/S) at 660 nm using a Spectraflash 600+ spectrophotometer (Datacolor International, USA, illuminant: D65, geometry: d/10°). The presented results were calculated as the mean of three values. The color strength value (K/S) was calculated following the Kubelka-Munk equation [15]:

$$K/S = \frac{(1-R)^2}{2R} - \frac{(1-R_0)^2}{2R_0} \quad (1)$$

where K is the absorption coefficient, S is the scattering coefficient, R_0 is the reflectance value of undyed fabric, and R is the reflectance of the dyed fabric.

DFT calculations

The optimized structures of the ferrous salts molecules, sodium dithionite and indigo, were determined using the Gaussian16 program package, based on the B3LYP level of theory in conjunction with the LANL2DZ basis set, accompanied by Grimme's D3BJ correction [16,17] and CPCM model for water solvation. Molecular orbitals were visualized by GaussView 6, while the VMD

1.9.4 program was used for Electrostatic potential (ESP) visualization [18]. The multifunctional wavefunction analyzer, Multiwfn, was employed to analyze electron density distributions [19]. The ESP evaluation code based on the LIBRETA library is being used.

To better understand the reduction mechanism of indigo with iron(II) salts and sodium dithionite, key quantum chemical descriptors of the reducing agents were analyzed based on the highest occupied molecular orbital (HOMO) and the lowest unoccupied molecular orbital (LUMO) energy values. The HOMO corresponds to the highest energy level occupied by electrons, reflecting a molecule's ability to donate electrons. In contrast, the LUMO represents the lowest available energy level, indicating the molecule's capacity to accept electrons. The energy gap (E_{Gap}), defined as the difference between HOMO and LUMO energy levels, serves as a parameter for assessing the molecule's stability and reactivity [20].

The overall reactivity descriptors using Koopman's theorem [21] are expressed by the following equations:

Electronegativity $\chi = \frac{(IP+EA)}{2}$ *(2)*

Chemical potential $\mu = \frac{-(IP+E\ )}{2}$ *(3)*

Hardness $\eta = \frac{(IP-EA)}{2}$ *(4)*

Electrophilicity index $\omega = \frac{\mu^2}{2\eta}$ *(5)*

Energy gap $\Delta E = E_{LUMO} - E_{HOMO}$ *(6)*

where E_{HOMO} is the highest occupied molecular orbital energy, E_{LUMO} is the lowest unoccupied molecular orbital energy, $IP = -E_{HOMO}$ is the ionization potential, and $EA = -E_{LUMO}$ is the electron affinity. Absolute electronegativity (χ), expressed in electron volts (eV), is a chemical descriptor that quantifies a system's (atom, molecule, ion, or radical) ability to attract electrons when forming chemical bonds, making it a useful tool for predicting chemical reactivity and behavior in various interactions. Softness is a characteristic attributed to molecules that denotes the capacity of an atom or group of atoms to accept electrons [22]. Hardness (η) characterizes the resistance of the molecular electron cloud to deformation under small perturbations. The electrophilicity index (ω) is a parameter that measures the energy reduction resulting from the maximum electron flow between donor and acceptor in a reaction, as defined by Eq. (5) [23]. Molecules can exhibit either electrophilic behavior, characterized by a higher electrophilic index, or nucleophilic behavior, associated with a lower electrophilic index, during reactions [24].

RESULTS AND DISCUSSION

Assessment of the Reducing Ability of Iron(II) Salts and Their Impact on Dyeing Performance

The influence of reducing agents concentration on the evolution of redox potential was examined in the presence of 2 g·L^{-1} of indigo and 15 g·L^{-1} of sodium hydroxide. To compare the reduction capacities of iron(II) salts with those of the conventional process, reductions were performed with different concentrations of sodium dithionite using 4 g·L^{-1} of caustic soda at a temperature of 50 °C.

The results are presented in Figure 1(a). This figure demonstrates that sodium dithionite generates the most negative redox potential values, below –700 mV, from a concentration of 0.01 M, highlighting its high efficiency as a reducing agent for indigo. Besides, it can be observed that exceeding a concentration of 0.036 M 16 g·L^{-1}, iron(II) gluconate gives a redox potential of about –732 mV. Iron(II) fumarate gives its minimum redox potential of -520 mV for a concentration of 0.047 mol·L^{-1}. This value decreases to -532 mV at a concentration of 0.043 mol·L^{-1} for iron(II) lactate. These findings indicate that iron(II) lactate and iron(II) fumarate are less effective as reducing agents and cannot achieve complete reduction of indigo.

Following the reduction of indigo with various reducing agents, the resulting dye baths were used for dyeing experiments. The dyeing performance was evaluated by measuring the color strength (*K/S*) at 660 nm. Figure 1(b) illustrates the variation in color strength of the dyed samples as a function of reducing agent concentration. The results indicate that iron(II) gluconate exhibits significantly superior dyeing performance compared to the other iron(II) salts, achieving a *K/S* value of 19 at a concentration of 0.04 mol·L^{-1} (18 g·L^{-1}). This value exceeds the color strength (*K/S*) of 17 obtained from reference dyeings using sodium dithionite. Beyond this concentration, a slight decline in color strength is observed. Similarly, iron(II) fumarate shows an increase in color strength from 0.07 mol·L^{-1} (12 g·L^{-1}), peaking at *K/S*= 5 at 0.095 mol·L^{-1} (16 g·L^{-1}), after which the color strength stabilizes. For iron(II) lactate, the color strength begins to increase from a concentration of 0.04 mol·L^{-1}and reaches a maximum *K/S* value of 11 at 0.085 mol·L^{-1} (20 g·L^{-1}), suggesting that a large quantity of this reducing agent is required to effectively reduce indigo. These findings indicate that, in addition to generating the necessary redox potential, iron(II) gluconate achieves the highest color strength, confirming its superior efficiency as a reducing agent in indigo dyeing.

DFT study of the investigated iron(II) salts as reducing agents for indigo

Global reactivity descriptors of indigo and iron(II) salts

Geometries of indigo and the reducing agents were first optimized using the B3LYP level of theory with the LANL2DZ basis set. The HOMO and LUMO energies were determined. From these two parameters, the molecular properties and global reactivity descriptors of the iron(II) salts, reducing agents, and indigo were calculated and tabulated in Table 1.

To evaluate the electron-donating capabilities of various iron(II) salts, their HOMO energy levels (E_{HOMO}) were analyzed and compared to that of sodium dithionite. E_{HOMO} is a key quantum chemical descriptor associated with a molecule's ability to donate electrons; a higher (less negative) HOMO value generally reflects stronger electron-donating potential [25,26]. As shown in Table 1, iron(II) gluconate has the least negative HOMO value (-6.19 eV)

among the studied salts, indicating the highest electron-donating ability in this group. In comparison, sodium dithionite exhibits a much higher HOMO energy (-3.50 eV), highlighting its superior reducing power.

Furthermore, iron(II) gluconate shows the largest HOMO-LUMO gap (4.45 eV) and highest chemical hardness (η = 2.23 eV), suggesting greater electronic stability and lower polarizability features typically associated with kinetically stable but less reactive species. Conversely, sodium dithionite, with its minimal energy gap (0.41 eV) and extremely low hardness (η = 0.21 eV), exhibits a highly reactive nature, consistent with its well-known effectiveness as a reducing agent.

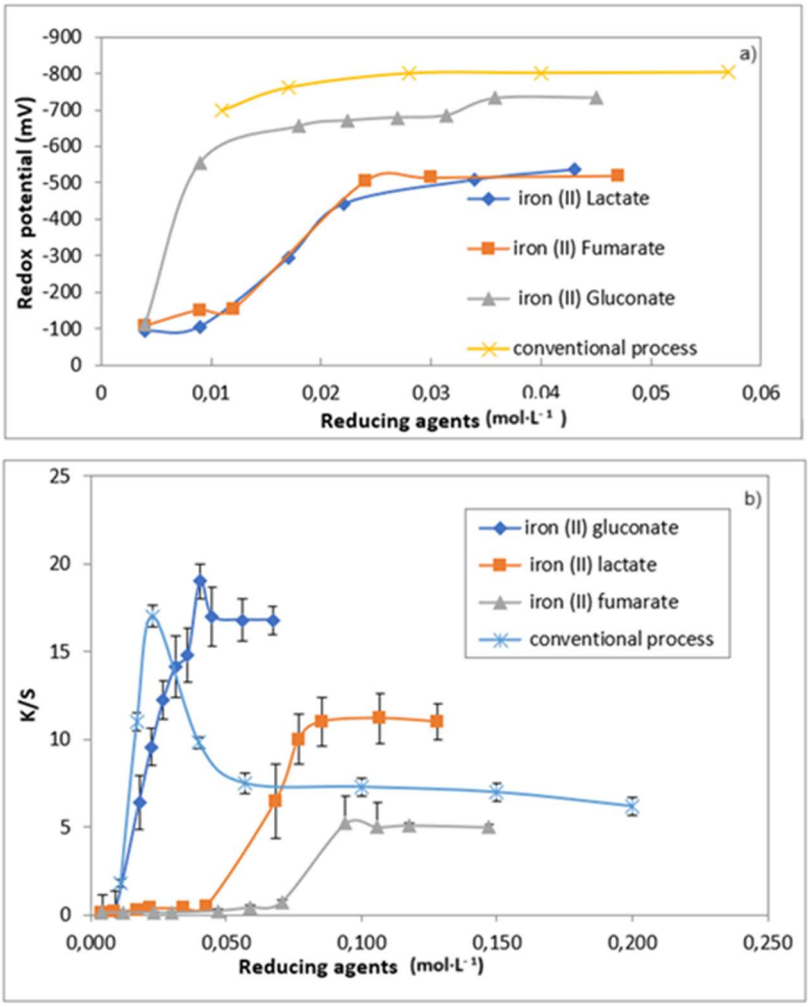

Figure 1. The evolution of (a) redox potential and (b) color strength (K/S) of the dyed samples as a function of the reducing agent concentrations.

Table 1. The optimized calculations of global reactivity descriptors for iron(II) salts.

Molecule	HOMO (eV)	LUMO (eV)	GAP (eV)	μ (eV)	η (eV)	ω (eV)
Indigo	-5.52	-3.21	2.31	4.37	1.16	8.25
Sodium dithionite	-3.50	-3.09	0.41	3.30	0.21	26.48
Iron(II) fumarate	-7.54	-4.30	3.24	5.92	1.62	10.83
Iron(II) lactate	-6.51	-2.21	4.30	4.36	2.15	4.43
Iron(II) gluconate	-6.19	-1.73	4.45	3.96	2.23	3.52

Notably, sodium dithionite displays an exceptionally high softness value (S = 4.76 eV), in contrast to iron(II) fumarate (0.617 eV), iron(II) lactate (0.465 eV), and iron(II) gluconate (0.448 eV). This high softness reflects its strong polarizability and electronic flexibility, both of which contribute to its rapid electron-transfer capacity in redox systems.

Regarding the electrophilicity index (ω), the trend among the iron(II) salts follows: iron(II) fumarate (10.83 eV) > iron(II) lactate (4.43 eV) > iron(II) gluconate (3.52 eV).

This descending order indicates that iron(II) gluconate is the least electrophilic and therefore the most nucleophilic, suggesting a greater ability to donate an electron pair during electron-transfer processes. Although sodium dithionite has an unusually high electrophilicity index (ω = 26.48 eV), a result of its high chemical potential and low hardness, this descriptor primarily reflects its overall reactivity. In aqueous solution, dithionite behaves as a strong reducing agent due to favorable thermodynamics and its capacity to deliver electrons to suitable oxidants.

Overall, the quantum chemical descriptors calculated for the studied compounds align well with the experimental dyeing results. In particular, the performance of iron(II) gluconate, which combines a relatively negative HOMO energy with moderate softness and low electrophilicity, supports its potential as an efficient and sustainable alternative to conventional reducing agents in textile applications.

Analysis of Electrostatic Potential (ESP)of the reducing agents and indigo

The Electrostatic Potential (ESP) maps provide a visual representation of the charge distribution within a molecule, allowing for the identification of electrophilic (electron-deficient) and nucleophilic (electron-rich) regions, which are critical for understanding molecular reactivity and non-covalent interactions [27-29]. In the ESP maps shown in Figure 2, red regions correspond to areas of high electron density (negative potential), indicating nucleophilic sites, while blue regions represent low electron density (positive potential), characteristic of electrophilic centers. Intermediate colors, such as light blue, yellow, and green, reflect areas of slight electron deficiency, slight electron richness, and neutrality, respectively.

The ESP surfaces of the iron(II) salts, gluconate, fumarate, and lactate, clearly show that the regions surrounding the Fe(II) centers are predominantly blue, indicating significant electron deficiency and supporting their role as electrophilic centers. In contrast, the ligands coordinating to Fe (II), particularly oxygen-containing groups, display red regions consistent with their nucleophilic nature. Notably, the ESP map of indigo reveals strong red zones around the carbonyl oxygen atoms, confirming them as the most nucleophilic sites within the molecule. This polarity pattern suggests favorable electrostatic interactions between the electrophilic iron(II) centers and the nucleophilic carbonyl oxygens of indigo, thereby supporting potential complexation pathways. These findings are in excellent agreement with experimental expectations and provide valuable insight into the electronic complementarity driving iron-indigo interactions. In addition, the ESP map of sodium dithionite reveals pronounced blue regions around the sodium atoms and the S-S bond, indicating areas of positive electrostatic potential, while red regions near the $-SO_2$ groups reflect high electron density. These nucleophilic zones make sodium dithionite an effective reducing agent, capable of donating electrons to electron-deficient (electrophilic) regions of indigo, thereby facilitating its reduction.

Reduction Mechanisms and Complexation Energies of [Iron(II) Salts -Indigo] Dimers

Visualization of complexation sites

The visualization of non-covalent interactions (NCIs) between indigo and iron(II) salts was utilized to identify complexation sites and gain deeper insights into the reactivity of the complexes. The NCI plots of indigo-iron(II) gluconate, indigo-iron(II) lactate, and indigo-iron(II) fumarate are presented in Figure 3. Based on this figure, it can be noted that in both Indigo-iron(II) fumarate and indigo-iron(II) gluconate complexes, the interaction primarily occurs between the oxygen of the carbonyl group in indigo and the iron(II) ion. Additionally, a hydrogen bond, represented by the blue isosurface, is observed between the N-H group of indigo and the oxygen atoms of iron(II) fumarate and iron(II) gluconate. In the indigo-iron(II) lactate complex, the carbon of the carbonyl (C=O) group in indigo appears to play a key role in the interaction with Fe(II), rather than the oxygen. Additionally, a coordination interaction is observed between the nitrogen of indigo and the Fe(II) ion.

To better understand the interaction sites between iron(II) salts and indigo, indigo Fukui indices used to identify nucleophilic attack sites were calculated. The nucleophilic sites correspond to regions where electron density increases upon electron addition, providing insight into potential interaction points within the complex.

The Fukui indices of the indigo molecule have been determined and presented in Table 2. The Fukui function f+ Measures a site's susceptibility to nucleophilic attack, indicating where an electron-rich species would most likely donate electrons. The atoms most reactive toward electrophilic attack have been identified by ranking the f+ values in descending order. According to the data, the following trend is observed: f+(O1, O2) = 0.1 > f+(C9, C11) = 0.08 > f+(C18, C20) = 0.07 > f+(C5, C8) = 0.04. These results show that the most nucleophilic sites in the indigo molecule are O1, O2, C9, C11, C18, and C20.

These atoms are the most favorable for electrophilic attack, suggesting their potential involvement in coordination with iron(II) centers. Figure 4 further visualizes the f+ indices for each atom in the indigo molecule, calculated using the B3LYP/6-311G (d,p) level of theory combined with LANL2DZ for iron(II). The corresponding molecular structure highlights the reactive centers identified by the Fukui analysis. The high f+ values at the carbonyl oxygens (O1 and O2) support their coordination with iron(II) in the indigo-iron(II) fumarate and indigo-iron(II) gluconate complexes. Similarly, the elevated f+ values at the adjacent carbon atoms (C9 and C11) are consistent with their interaction with iron(II) in the Indigo-iron(II) lactate complex.

Evaluation of the interaction energy between indigo and the reducing agents

In this section, the reducing capacity of the studied iron(II) salts was determined through the complexation energies between indigo and the different iron(II) salts using the DFT, as mentioned by the following equation:

$$E(complexation) = E(dimer) - [E(indigo) + E(reducing\ agent)] \quad (7)$$

The interaction energy values, calculated using Eq. (7), were corrected using the counterpoise method to account for the basis set superposition error (BSSE). This correction improves the accuracy of the calculated interaction energy, ensuring it better reflects the true physical value, particularly in systems dominated by weak interactions such as hydrogen bonding and *Van der Waals* forces.

The complexation energy calculations presented in Table 3 indicate that the [indigo-iron(II)-gluconate] complex exhibits the highest complexation energy (-1078 kJ·mol^{-1}), signifying greater stability. This suggests stronger intermolecular forces, including charge transfer between Fe(II) and indigo, hydrogen bonding, and electrostatic and *van der Waals* interactions.

Following this, the [indigo-iron(II)-lactate] complex with an interaction energy of (-996 kJ·mol^{-1}) demonstrates comparatively lower stability. Meanwhile, the [indigo-iron(II)-fumarate] complex has the lowest interaction energy (-844 kJ·mol^{-1}), indicating the weakest stability. As a result, Fe(II) in this complex is more subjected to oxidation, making it the least effective reducing agent for indigo. These interaction energy calculations align with experimental observations, confirming that iron(II) gluconate enhances indigo reduction by stabilizing Fe(II) in its reduced state.

Thermodynamic properties of the (indigo-reducing agents) complexes

To investigate the thermodynamic properties of the reduction reactions, thermodynamic calculations were performed using the DFT approach at 298.15 K. To assess the overall stability of the (indigo-iron(II) salts) complexes, the thermodynamic parameters: Gibbs free energy (ΔG°), entropy (ΔS°), and enthalpy (ΔH°) of formation were determined using the following equations and presented in Table 4.

$$\Delta G° = \Delta G°_{complex} - (\Delta G°_{indigo} + \Delta G°_{reducing\ agent}) \quad (8)$$

$$\Delta H° = \Delta H°_{complex} - (\Delta H°_{indigo} + \Delta H°_{reducing\ agent}) \quad (9)$$

$$\Delta S° = \Delta S°_{complex} - (\Delta S°_{indigo} + \Delta S°_{reducing\ agent}) \quad (10)$$

.

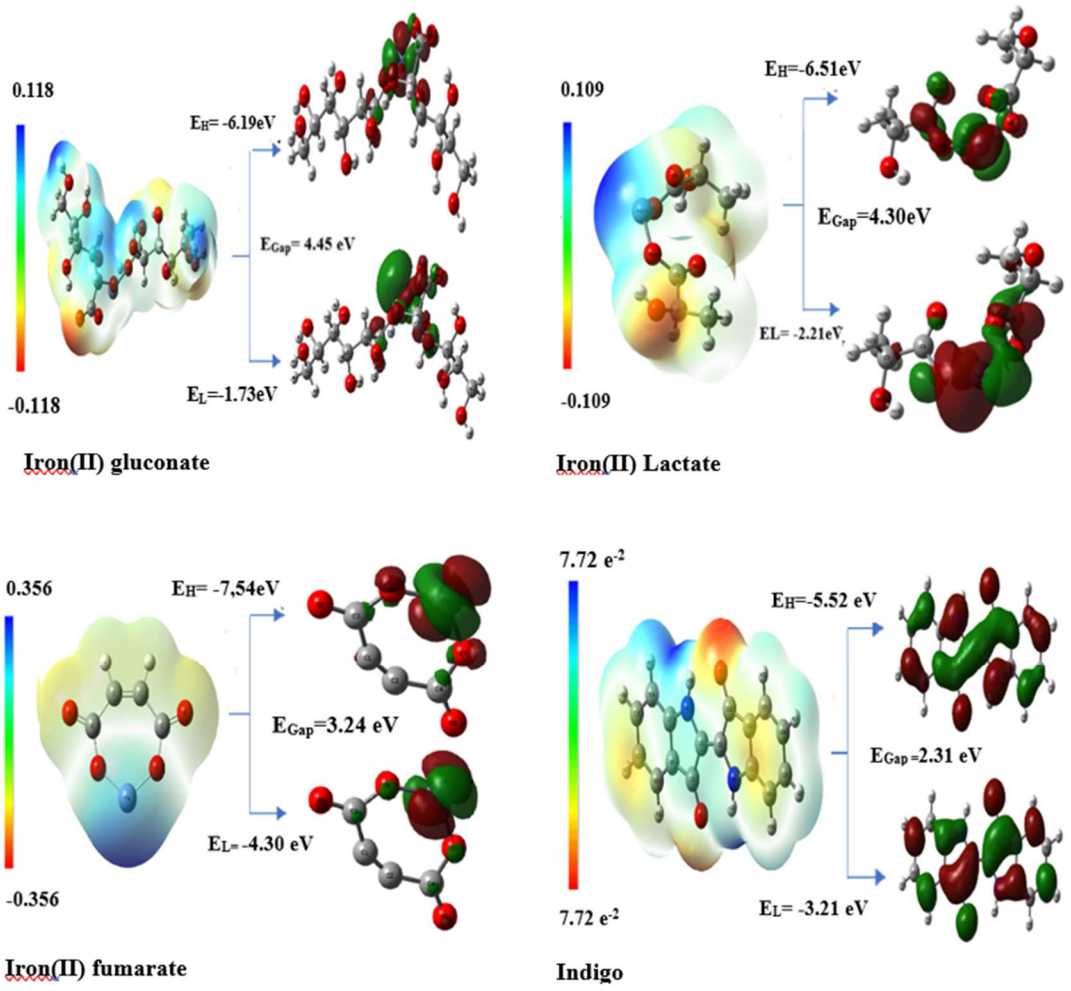

Fig 2. Electrostatic potential (ESP) and HOMO/LUMO orbital distributions with energy levels for indigo and the reducing agents, showing regions of electron density and potential reactivity.

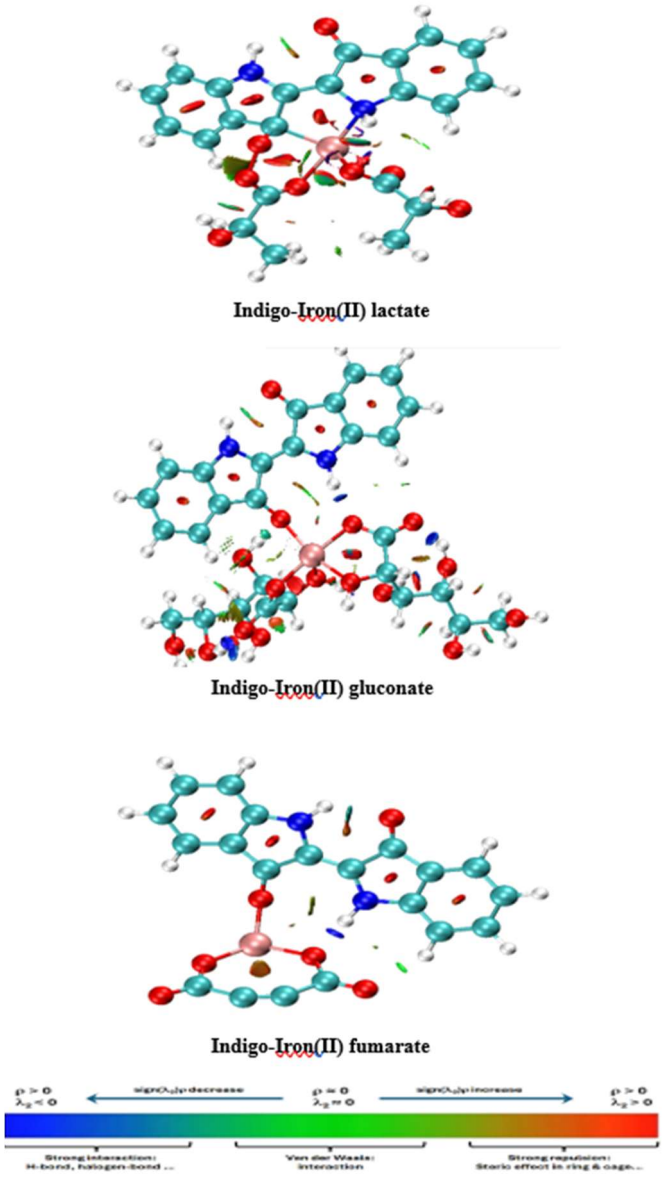

Fig 3. NCI plots of indigo-iron(II) gluconate, indigo-iron(II) lactate, and indigo-iron(II) fumarate complexes.

Gibbs free energy (ΔG) is a key indicator of reaction feasibility, with lower values indicating a more thermodynamically favorable reaction. According to Gaussian calculations, the positive ΔG values suggest that complex formation in the studied state is not spontaneous and requires external energy input. This finding supports the experimental condition of a reduction temperature of 75 °C.

Furthermore, these positive values can be attributed to the presence of a polar solvent such as water, which stabilizes ions in solution and alters the reaction dynamics. Among the investigated iron(II) salts, the indigo-iron(II) gluconate complex exhibits the lowest Gibbs free energy, indicating that it is the most thermodynamically stable complex. Additionally, this complex has the lowest enthalpy ($\Delta H° = 1338$ kJ·mol^{-1}), suggesting that its formation requires less energy input compared to the other complexes. Moreover, all complexes exhibit negative entropy values ($\Delta S° < 0$), implying increased structural order upon complexation.

Mulliken Charge Analysis

To investigate the reduction of indigo by ferrous salts, Mulliken charges of the reducing agents and indigo before and after complex formation were calculated. Figures S1 and S2 (Supplementary Materials) illustrate the Mulliken charge distribution in the individual iron(II) salts, indigo, and their respective complexes. The initial charge on Fe(II) in iron(II) gluconate, lactate, and fumarate was 0.887, 0.999, and 2.663, respectively. After complexation with indigo, these values decreased to 0.603, 0.357, and 0.776, respectively, suggesting partial electron transfer from Fe^{2+} to indigo.

Table 4. Mulliken charges of indigo at B3LYP/6-311G(d,p) with LANL2DZ for iron(II).

	Indigo		
	$f^{-}\cdot10^2$	$f^{+}\cdot10^2$	$f^{0}\cdot10^2$
O1	7.45	10.39	8.92
O2	7.45	10.39	8.92
N3	11.01	0. 15	5.58
N4	11.01	0. 15	5.58
C5	3.62	4.92	4.27
C6	2.27	-0.98	0.65
C7	-2.35	2.28	0.04
C8	3.62	4.92	4.27
C9	0.83	8.51	4.67
C10	2.27	-0.98	0.65
C11	0.83	8.51	4.67
C12	-2.35	2.28	0.04
C13	2.48	4.62	3.55
C14	5.43	0.93	3.18
C15	2.48	4.62	3.55
C16	5.43	0.93	3.18
C17	6.97	2.24	4.61
C18	1.86	7.04	4.45
C19	6.97	2.24	4.61
C20	1.86	7.04	4.45

Table 5. Complexation energies for (indigo-iron(II) salts) dimers.

Dimers	Complexation Energy (corrected) (kJ·mol^{-1})
Indigo-iron(II) gluconate	- 1078
Indigo-iron(II) lactate	- 996
Indigo-iron(II) fumarate	- 844

Concurrently, the charge on the oxygen of the indigo carbonyl group (C=O) shifted from -0.344 to -0.477 and -0.527 for iron(II) gluconate and iron(II) fumarate complexes, respectively, supporting increased electron density on indigo and its reduction.

For indigo-iron(II) lactate complex, upon complexation, the charge on the carbonyl carbon decreased from +0.272

to -0.187, while the charge on the nitrogen of indigo shifted from -0.522 to -0.606. These changes indicate an increase in electron density at the reactive sites of indigo, suggesting significant electron transfer and stabilization within the complex.

Table 4. Thermodynamic parameters of [indigo-iron(II) salts] complexes in kcal.mol-1 at B3LYP with LANL2DZ.

Complexes	$\Delta H°$ (kJ·mol $^{-1}$)	$\Delta G°$ (kJ·mol $^{-1}$)	$\Delta S°$ (kJ mol^{-1}·K^{-1})
Indigo-iron(II) gluconate	1338	1417	-0.159
Indigo-iron(II) lactate	1612	1925	-0.347
Indigo-iron(II) fumarate	4489	4546	-0.184

Although the indigo-fumarate complex exhibited the highest theoretical charge transfer from Fe(II), experimental findings indicate that iron(II) gluconate achieves superior reduction efficiency. This divergence may be attributed to differences in solubility, complex stability, and electron transfer kinetics.

CONCLUSIONS

DFT was used to predict the reducing capacity of iron(II) gluconate, iron(II) lactate, and iron(II) fumarate, as possible alternatives to sodium dithionite in indigo dyeing processes. Experimental results revealed that iron(II) gluconate demonstrated superior reducing efficiency and color strength in dyeing applications. The chemical descriptors calculations using DFT indicated that iron(II) gluconate has a stronger electron-donating capability and higher nucleophilicity, which may contribute to its superior performance in indigo reduction. For the complexes studied, all complexation reactions were found to be thermodynamically unfeasible at 25 °C and require an external energy input. Mulliken charge analysis showed the possibility of iron(II) salts in the indigo charge transfer.

Beyond complexation energy calculations, additional evidence confirmed that iron(II) gluconate promotes indigo reduction by stabilizing Fe(II) in its reduced form.

As a result of the above outcomes, it can be stated that the combination of theoretical and experimental studies is very efficient in evaluating the reducing power of ferrous salts.

Acknowledgments

The authors thank the Tunisian Higher Education and Scientific Research Ministry for the financial support. The authors would like to thank Dr. Aïcha Ayeb for her assistance in conducting ESP (Electrostatic Potential) interpretations.

REFERENCES

[1] M. Abdelileh, A.P. Manian, D. Rhomberg, M. Ben Ticha, N. Meksi, N. Aguiló-Aguayo, T. Bechtold, J. Cleaner Prod. 266 (2020) 121753. https://doi.org/10.1016/j.jclepro.2020.121753.

[2] M. Ben Ticha, N. Meksi, N. Drira, M. Kechida, M.F.Mhenni, Chem. Ind. Chem. Eng. Q. 20 (2014) 463-470. https://doi.org/10.2298/CICEQ130507028B.

[3] M. Božič, V. Kokol, Dyes Pigm. 76 (2008) 299-309. https://doi.org/10.1016/j.dyepig.2006.05.041.

[4] N. Meksi, M. Kechida, M.F. Mhenni, Chem. Eng. J. 131 (2007) 187-193. https://doi.org/10.1016/j.cej.2007.01.001.

[5] N. Meksi, M. Ben Ticha, M. Kechida, M.F. Mhenni, Chem. Res. 49 (2010) 12333-12338. https://doi.org/10.1021/ie100974.

[6] N. Meksi, M. BenTicha, M. Kechida, M.F. Mhenni, J. Cleaner Prod. 24 (2012) 149-158. https://doi.org/10.1016/j.jclepro.2011.11.062.

[7] J.N. Chakraborty, R.B. Chavan, J. Fibre. Text. 29 (2004) 100-109. https://nopr.niscpr.res.in/handle/123456789/22596.

[8] R.B. Chavan, J.N. Chakraborty, Color. Technol. 117 (2001) 88-94. https://doi.org/10.1111/j.1478-4408.2001.tb00340.x.

[9] V.C. Mudnoor, J.N. Chakraborty, J. Fibre. Text. Res. 45 (2019) 109. http://nopr.niscpr.res.in/handle/123456789/54131

[10] P. Mazumdar, J.N. Chakraborty, Tekstile 62 (2019) 187-199. https://doi.org/10.14502/Tekstilec2019.62.

[11] C. Li, R. Requist, E.K.U. Gross, J. Chem. Phys. 148 (2018) 084110. https://doi.org/10.1063/1.5011663.

[12] A. Hashemi, P. Peljo, K. Laasonen, J. Phys. Chem. C 127 (2023) 3398-3407. https://doi.org/10.1021/acs.jpcc.2c06537.

[13] N. Naeem, T. Tahir, M. Ans, A. Rasool, R. Aqil Shehzad, J. Iqbal, Comput. Theor. Chem. 1204 (2021) 113416. https://doi.org/10.1016/j.comptc.2021.113416.

[14] J.H. Xin, C.L. Chong, T. Tu, Color. Technol. 116 (2000) 260-265. https://doi.org/10.1111/j.1478-4408.2000.tb00044.x.

[15] P. Kubelka, F. Munk, Zh. Tekh. Fiz. 12 (1931) 593-601. https://www.graphics.cornell.edu/~westin/pubs/kubelka.pdf.

[16] S. Grimme, S. Ehrlich, L. Goerigk, J. Comput. Chem. 32 (2011) 1456-1465. https://doi.org/10.1002/jcc.21759.

[17] A. Abkari, I. Chaabane, K. Guidara, Physica E Low Dimens. Syst. Nanostruct. 81 (2016) 136-144. https://doi.org/10.1016/j.physe.2016.03.010.

[18] J. Zhang, T. Lu, Phys. Chem. Chem. Phys. 23(2021) 20323. https://doi.org/10.1039/D1CP02805G.

[19] S. Tsuzuki, T. Uchimaru, Phys. Chem. Chem. Phys. 22 (2020) 22508-22519. https://doi.org/10.1039/D0CP03679J.

[20] Z.A. Guo, J.Y. Xian, L.R. Rong, H. Qin, Z. Jie, Monatsh Chem. 150 (2019) 1355-1364. https://doi.org/10.1007/s00706-019-02419-1.

[21] T. Koopmans, Physica 1 (1933) 104-113. https://doi.org/10.1016/S0031-8914(34)90011-2.

[22] P. Senet, Chem. Phys. Lett. 275 (1997) 527-532. https://doi.org/10.1016/S0009-2614(97)00799-9.

[23] R.G. Parr, L.V. Szentpály, S. Liu, J. Am. Chem. Soc. 121 (1999) 1922-1924.

https://doi.org/10.1021/ja983494x.
[24] P.K. Chattaraj, B. Maiti, U. Sarkar, J. Phys. Chem. 25 (2003) 4973-4975. https://pubs.acs.org/doi/full/10.1021/jp034707u.
[25] G. Gece, S. Bilgic, Corros. Sci. 51 (2009) 1876-1878. https://doi.org/10.1016/j.corsci.2009.04.003.
[26] G. Gece, Corros. Sci. 50 (2008) 2981-2992. https://doi.org/10.1016/j.corsci.2008.08.043.
[27] S. Manzetti, T. Lu, J. Phys. Org. Chem. 26 (2013) 473-483. https://doi.org/10.1002/poc.3111.
[28] T. Lu, F. Chen, J. Mol. Model. 19 (2013) 5387-5395. https://doi.org/10.1007/s00894-013-2034-2.
[29] T. Lu, S. Manzetti, Struct. Chem. 25 (2014) 1521-1533. https://doi.org/10.1007/s11224-014-0430-6.

MAHA ABDELILEH[1]

MANEL BEN TICHA[2]

NIZAR MEKSI[1,3]

HATEM DHAOUADI[1]

[1]University of Monastir, Faculty of Sciences of Monastir, Research Laboratory of Environmental Chemistry and Clean Processes, Tunisia.

[2]Department of Early Childhood, University College of Turabah, Taif University, Saudi Arabia

[3]University of Monastir, National Engineering School of Monastir, Department of Textile, Tunisia

NAUČNI RAD

PRIMENA TEORIJE FUNKCIONALA GUSTINE ZA PREDVIĐANJE REDUKCIJIONOG POTENCIJALA U PROCESU BOJENJA INDIGOM

U ovom radu je korišćena teorija funkcionalne gustine za kvantifikaciju svojstava donora i akceptora elektrona i polarizabilnosti organskih soli gvožđa(II) kao redukcionih agenasa u procesima bojenja indigom. Istražen je potencijal nekih soli gvožđa(II) kao ekološki prihvatljive alternative ekološki štetnom natrijum-ditionitu u procesu bojenja indigom. Komparativnom analizom je procenjen redoks potencijal redukovanog indiga i jačina boje obojenih tkanina. Eksperimentalni rezultati identifikovali su gvožđe(II)-glukonat kao najefikasniji, koji daje superiorni intenzitet boje. Teorijski proračuni korišćenjem B3LYP/LANL2DZ potvrdili su superiornu sposobnost gvožđe(II)-glukonata kao donora elektrona u poređenju sa drugim solima gvožđa(II). Sposobnost redukcije indiga sa solima gvožđa(II) procenjena je na osnovu energija kompleksacije. Teorijska termodinamička studija otkriva da je kompleks indigo-gvožđe(II)-glukonat termodinamički najstabilniji, tako da zahteva manje ulaganja energije za njegovo formiranje u poređenju sa drugim kompleksima. Donacije elektrona od soli gvožđa(II) do indiga u proučavanim kompleksima otkrivene su Mulikenovom analizom naelektrisanja. Ovi nalazi ističu efikasnost pristupa zasnovanih na teoriji funkcionalne gustine u preciznom predviđanju redukcionog kapaciteta soli gvožđa(II) i njihovu pogodnost kao ekološki prihvatljivih alternativa u primenama bojenja indigom.

Ključne reči: Bojenje indigom; soli gvožđa(II); proračuni na bazi teorije funkcionalne gustine; eksperimentalni rezultati, energija kompleksacije.

CI&CEQ
Chemical Industry & Chemical Engineering Quarterly

Available online at
Association of the Chemical Engineers of Serbia AChE
www.ache.org.rs/CICEQ

Chem. Ind. Chem. Eng. Q. 32 (2) 163–173 (2026) CI&CEQ

SAKTHI RAJAN CHANDRAMURTHY[1]
SILAMBARASAN RAGUNATHAN[2]
RAMESH KUMAR AYYAKKANNU[3]
ANBARASAN BALUCHAMY[4]

[1]SBM College of Engineering & Technology, Dindigul, Tamil Nadu, India

[2]Annamalai Polytechnic College, Chettinad, Tamil Nadu, India

[3]Sona College of Technology, Salem, Tamil Nadu, India

[4]PSNA College of Engineering & Technology, Dindigul, Tamil Nadu, India

SCIENTIFIC PAPER

UDC 662.756.3:582.521.11:621.436.2

COMBUSTION, PERFORMANCE, AND EMISSION CHARACTERISTICS OF A CI ENGINE USING *BORASSUS FLABELLIFER* BIODIESEL BLENDS

Highlights

- Biodiesel is derived from *Borassus flabellifer*.
- Five biodiesel blends (B20, B40, B60, B80, and B100) are examined in a diesel engine.
- HC, CO, and smoke emissions were found to be lower, while NO_x emissions were observed to be higher.
- Performance of the biodiesel blends was comparable to that of the diesel fuel.

Abstract

Borassus flabellifer methyl esters (BFMEs) have a few attractive characteristics that make them a potential rival to diesel and other alternative fuels. This study presents the first comprehensive analysis of its performance, combustion, and emission characteristics in a diesel engine. In addition to a high calorific value, a high cetane number, and the availability of oxygen, constituting 10% of its total weight, it is also readily available. Experimental testing of BFMEs was conducted on a single-cylinder compression ignition (CI) engine in this stage. BFMEs were blended with diesel at various concentrations (20%, 40%, 60%, 80% and 100%). Blends of BFMEs were experimentally examined for their combustion properties, emissions, and performance. The CI engine was set to steady-state operation so that it would reach the optimum temperature for the conditions in which it was operating. Initially, it was found that neat BFMEs had the lowest thermal efficiency, while BFME20, BFME40, BFME60, and BFME80 all had a higher brake thermal efficiency (BTE) than BFME100 at rated load conditions (by 5.1%, 2.8%, 2.0%, and 1.4%, respectively). Compared to other blends, BFME20 and BFME40 have better fuel efficiency. Fuel efficiency was improved by a reasonable amount, and BFME20's consumption was reduced by 5.1% compared to BFME100. Compared to diesel, hydrocarbons, CO, and smoke emissions from BFME20 were reduced by 9.9%, 5.8%, and 3.71%, respectively. These results underscore the potential of low-ratio BFME blends as cleaner and more efficient biodiesel alternatives, highlighting BFME's practical applicability in existing diesel engines without major modifications.

Keywords: Biodiesel, Borassus flabellifer, Combustion, Performance and emission characteristics.

INTRODUCTION

Researchers are constantly investigating potential alternatives to the existing reliance on fossil fuels, which serve as the dominant energy source for industrial purposes. Nowadays, there is a significant focus on the study of combustion processes using alternative fuels, especially for diesel fuel, to bring about transformative changes in the transportation industry [1]. Owing to their various compositions and the lack of experimental response data in the literature, predicting the combustion behavior of these alternative fuels is difficult [2]. The current endeavor is made much more difficult by the presence of this obstacle. The reduction of exhaust emissions is the primary emphasis of research and development for alternative diesel fuels, which is in line with the goals of protecting the environment and saving energy [3]. Synthetic fuels, dimethyl ether, biodiesel, diethyl ether (DEE), methane, alcohols, and hydrogen are important alternatives to conventional fuels [4]. Decisions regarding future fuels are constrained by variables including fuel availability, production feasibility, and transportation logistics. The choice is

Correspondence: Sakthi Rajan C, SBM College of Engineering & Technology, Dindigul, Tamil Nadu, India - 624 005.
Email: csrajann@gmail.com
Paper received: 26 February, 2025
Paper revised: 17 June, 2025
Paper accepted: 27 June, 2025

https://doi.org/10.2298/CICEQ250226019C

primarily led by energy efficiency and emissions analyses [5] carried out to evaluate the engine characteristics of different alternative fuels (rice bran oil, mahua oil, linseed oil) in a single-cylinder, 4-stroke diesel engine. This study aimed to evaluate these options in comparison to conventional mineral diesel. As a result of their high viscosity, low volatility, and polyunsaturation, these oils blended with diesel revealed operational and durability concerns compared to plain vegetable oils. During blending with linseed oil methyl ester, the severity of these problems reduced. Economic analysis showed that vegetable oil derivatives could replace mineral diesel at a lower cost, eliminating fossil fuel dependence. The engine characteristics of a diesel engine running on poon oil in its purest form as well as in a variety of blends with diesel. Poon oil was blended with diesel to solve issues associated with carbon deposits and poor atomization, which come with vegetable oils [6]. Lower viscosity, enhanced volatility, enhanced combustion properties, less carbon deposits, and decreased nitrogen oxide (NO_x) emissions were among the favorable outcomes. The study revealed that combining poon oil with diesel could improve diesel engine performance and emissions while decreasing brake thermal efficiency (BTE). The experiment test was conducted on a single-cylinder, 4-stroke, variable compression ratio (VCR) multi-fuel engine was powered by waste cooking oil methyl ester and a variety of blends with regular diesel [7]. While comparing the biodiesel blends with diesel, it was found that biodiesel blends resulted in significant improvements in performance characteristics. These benefits included an increase in BTE as well as decreased emissions of hydrocarbons (HC), CO, and CO_2. However, there was a surge in NO_x emissions. An investigation of the karanja oil blends (20–50%) on emissions and performance in a DI-CI engine showed that the addition of karanja oil has resulted in improved combustion pressure (CP) and heat release rate (HRR) and decreased emissions of HC, CO, and smoke [8]. An exhaustive study on the performance and tailpipe emissions of a HINO H07C DDF engine powered by various fuels, including biodiesel. Compared to diesel, biodiesel showed better levels of torque and horsepower, indicating that it can serve as an ecologically aware alternative for heavy transportation fleets. As a result, CO_2 and NO_x emissions increased, which constituted a trade-off [9]. The combustion and thermal efficiency of a diesel engine fueled with diesel and linseed oil. The study found that the quantity of linseed oil had a non-monotonous effect on engine performance, with the best combustion characteristics obtained when using a blend containing 20% of linseed oil [10]. The efficiency and emissions of a single-cylinder, 4-stroke diesel engine powered by biodiesel generated from Euglena sanguinea algae. The findings demonstrated that emissions of HC and CO substantially decreased up to the ES30 blend ratio; however, emissions of NO_x were slightly increased [11]. The effectiveness and characteristics of pollutants in biodiesel sourced from rubber seed oil. The results demonstrated that the B10 blend displayed the most favorable brake-specific fuel consumption (BSFC) and BTE. A significant concern about biodiesel blends is the slight rise in NO_x emissions [12]. The effect of karanja biodiesel on the engine performance of a compression ignition engine has exhibited a slight decrease in BTE and an increase in BSFC. Additionally, there was a reduction in HC and CO emissions, alongside a slight increase in NO_x emissions [13]. The effects of neem biodiesel blended with diesel on the efficiency and exhaust emissions of a VCR engine. The study revealed that blends of biodiesel made primarily from neem oil, especially those with a higher compression ratio, may offer an eco-friendly substitute for regular diesel fuel while preserving or enhancing emissions and engine performance [14]. Compared to diesel, this technique reduces emissions of CO by 14% and NO_x by 3%. Emission data may be continuously and instantly monitored with the use of an Internet of Things emission monitoring kit [15]. The utilization of kapok oil methyl esters (KOMEs) as a biodiesel by blending it with conventional diesel fuel at volumetric ratios of 10%, 20%, and 30%, resulting in KOME10, KOME20, and KOME30 blends, respectively. The combustion analysis revealed that, during stationary engine operation, both the peak cylinder pressure (Pmax) and the maximum net heat release rate (HRRmax) were lower than those of pure diesel. In a common rail direct injection (CRDI) system, the Pmax increased by 13–15% and HRRmax by 16–32% compared to diesel. Examination of engine emissions revealed a reduction in carbon dioxide (CO_2), unburned hydrocarbons (UBHCs), and smoke concentrations in all KOME blends. Nitric oxide (NO) emissions showed a slight increase, rising around 0.7–1.5% in the stationary mode and 1.3–8% in the CRDI mode relative to diesel. The results suggest that KOME blends could be a viable alternative fuel for non-road direct injection diesel engine applications [16]. The performance of a 5–25% polanga biodiesel blend study found the B10 performance equivalent to diesel fuel and reduced emissions, suggesting that polanga biodiesel could be a promising future fuel with a focus on balancing the emissions and performance in the diesel engine [17]. There have been numerous studies conducted on plant-based oils; however, this particular study is among the first to methodically investigate the combustion, emission, and performance properties of BFME in a CI engine by utilizing a variety of blend ratios. Comparison study of a single-cylinder diesel engine operating at a constant speed using different fuel blends are displayed in Table 1. The upward direction represents an increase, while the downward direction represents a loss.

This study compares the performance of an engine with different biodiesel blends of *Borassus flabellifer* methyl esters (BFMEs) using a consistent experimental setup. *B. flabellifer* oil was used for the transesterification process of producing biodiesel. Each blend was compared with diesel fuel by using it in a diesel engine and obtaining engine performance values. All data were then compared graphically with each other and with diesel fuel to determine the most suitable blend.

Table 1. Comparison study of a single-cylinder diesel engine operating at a constant speed using different fuel blends.

Fuel type	Efficiency		Emission Characteristics				Reference
	BSFC	BTE	CO	NO_x	HC	Smoke	
Waste sunflower & kohlrabi grape seed oil	↓	↑	↓	↑	↓	↓	[18]
Poppy and Canola Oils	↓	↑	↓	↑	↓	↓	[19]
Waste sunflower and cotton oil	↓	↑	↓	↑	↓	↓	[20]
Kapok oil	↓	↑	↓	↑	↓	↓	[21]
Coconut waste cooking oil	↓	↑	↓	↓	↓	↓	[22]
Rice bran oil	↓	↑	↓	↓	↓	↓	[23]
Rapeseed oil	↑	↑	↓	↑	↓	↓	[24]
Juliflora seed oil	↓	↑	↓	↑	↓	↑	[25]
Borassus flabellifer oil	↓	↑	↓	↑	↓	↓	Present study

MATERIALS AND METHODS

B. flabellifer Biodiesel

The oil extracted from *B. flabellifer* was purchased in a local market in the Indian state of Tamil Nadu. From a chemical distributor, anhydrous methanol, acetic acid, and potassium hydroxide were obtained. The quality of the chemicals used in this process was suitable for analytical usage. The transesterification process (Figure 1) was carried out using a conical flask that was fitted with a thermometer, a magnetic stirrer, and a reflux condenser. *B. flabellifer* oil was added to the flask at first, and it was preheated to 65 °C. Methanol was used to dissolve potassium hydroxide, which was used as a catalyst. The solution obtained was then added to the shaking flask, and a 2h timer was used to monitor the reaction. After that, the mixture was allowed to sit in a separating funnel so that the glycerol layer was able to be extracted. After being rinsed twice with warm water containing 5% acetic acid, methyl esters were finally washed with water. Remaining methanol and water were removed from biodiesel using a rotating evaporator heated to 80 °C in a vacuum. The methyl esters of *B. flabellifer* oil were then dried at 100 °C. The properties of BFMEs are shown in Table 2. The production of the total cost of *Borassus* oil is Rs 36 per litre, which is considerably less than the cost of diesel, Rs 70 per litre. It is valuable to note that the cost will reduce with a rise in mass production and plant facilities.

Properties of Biodiesel

Following the production of the required amount of methyl esters of the oil, the required characteristics of the esters were determined using IS test techniques (IS: 1448). The sample was prepared and tested for physicochemical properties in the ITA lab, Chennai. The experimentation was presented based on various biofuel and basic properties, inclusive of density, calorific value, and cetane number, etc. The properties of all the fuels are tabulated by testing in a local chemical analysis laboratory, as shown in Table 2.

FTIR Analysis

Fourier transform infrared (FTIR) spectroscopy is effective and versatile in evaluating biodiesel quality [26,27]. Figure 2 illustrates that the FTIR spectra of both the raw oil and the produced biodiesel have notable similarities, indicating that the chemical structure and functional groups remained mostly unchanged during the process. Microwave irradiation for localized heating did not elicit any detrimental side reactions. The conversion of triacylglycerol molecules into fatty acid methyl esters and glycerol was successfully achieved. The FTIR spectra display distinct absorption peaks, notably the carbonyl (C=O) stretching at 1744 cm^{-1} and the C-O stretching at 1163 cm^{-1}, consistent with results from prior studies [28], thus confirming the retention of these functional groups in the biodiesel product. The spectra suggest stretching vibrations associated with CH, CH_2, and CH_3 groups at 3003, 2854, and 2922 cm^{-1}, respectively. Bending vibrations (ρCH_2) for these groups are seen at 1375, 1163, and 723 cm^{-1}. The spectral features confirm the structural integrity of the biodiesel and validate the effectiveness of FTIR spectroscopy in evaluating its content and quality.

Test Engine

A four-stroke, water-cooled, vertically mounted, single-cylinder diesel engine with DI was part of the experimental setup. An eddy current dynamometer was used in conjunction with this engine, which had a fixed compression ratio of 16.5 and operated constantly at 1500 rpm. Figure 3 shows the test engine for the experimental setup, and the specifications of the engine are mentioned in Table 3. The accuracy and uncertainty in the measurement of the engine and uncertainty are shown in Table 4. This engine type was selected due to its importance as a primary power source in a variety of Indian industries, including agriculture, construction, industry, and energy generation. The experimental setup includes all the necessary sensors for gauging variables, including air/fuel ratio, cylinder pressure (CP), crank angle (CA), temperature, and load. The engine fuel that was used for testing consisted of a number of different fuel mixes with different concentrations, including B20, B40, B60, B80, and B100. The dependability of the data, as well as its reproducibility, was enhanced by taking the average of the outcomes of each experiment, which was carried out three times. The accuracy of the experiments was checked using an uncertainty analysis that was carried out. To estimate the percentage uncertainties of essential parameters, such as braking thermal efficiency and load, a comparison was made between the percentage uncertainties of the measurement devices and those stated in Table 5. The experimental setup includes all the necessary sensors for gauging variables, including air/fuel ratio, CP, CA, tempera-ture, and load. A data acquisition system connects these instruments to a computer for real-time data collection and analysis.

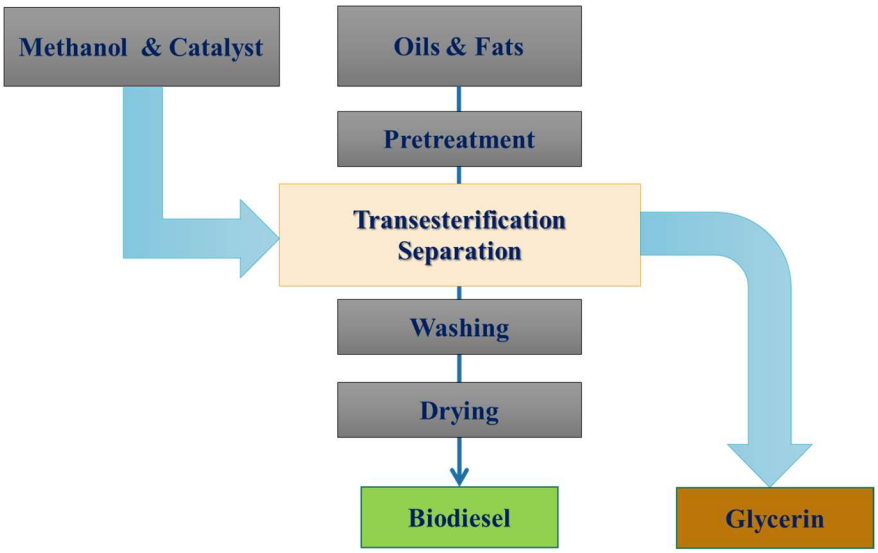

Fig. 1. Transesterification process.

Table 2. Properties of *Borassus flabellifer* biodiesel blends.

Fuel Blends	Diesel	BFME	BFME 20	BFME 40	BFME 60	BFME 80	Test Standard
Viscosity at 30 °C (mm^2/s)	3.3	4.5	3.63	3.82	4.18	4.31	ASTM D 445-04e
Energy content (kJ/kg)	43300	40250	42153	41895	41350	40860	ASTM D5865
Cetane no.	54	57	55	56	56	57	ASTM D 613-05
Density (kg/m^3)	835	870	849	852	860	866	ASTM D7371-12
Flash point (°C)	50	128	69	86	105	122	EN ISO 2719

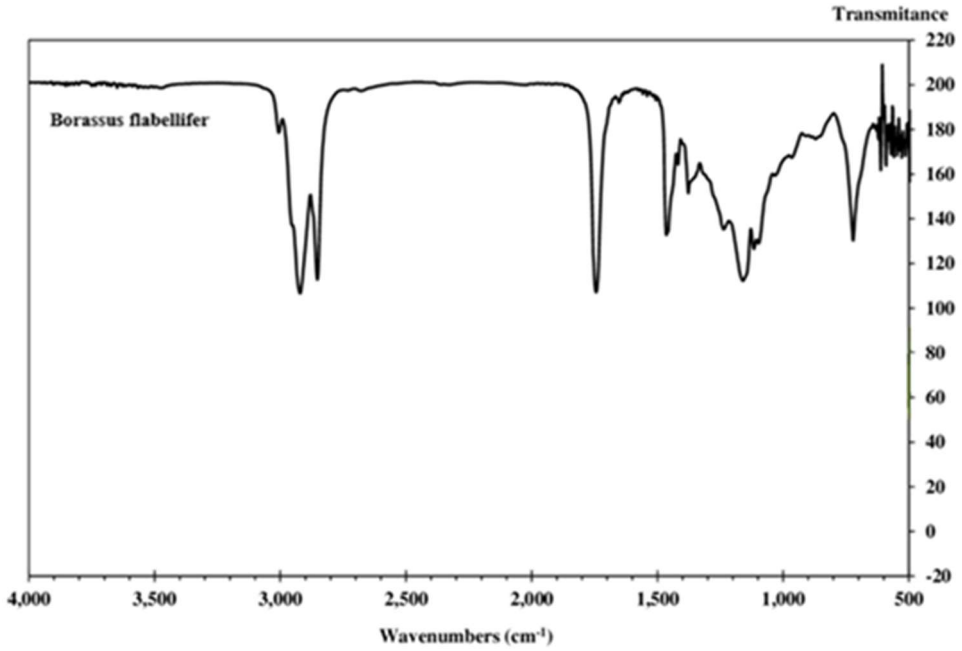

Fig. 2. Borassus flabellifer oil FTIR spectra.

Fig. 3. Experimental setup.

Table 3. Specification of the engine.

Details	Data
Manufacturing	Kirloskar
Model	TV1
Type of engine	Naturally aspirated diesel engine
Max. Brake power at rated speed	5.1 kW at a rated constant speed
Bore/stroke	88/110 mm
Engine CR	17.1:1
Injection mode and timing	Direct and 23° before TDC
Type of lubrication	Forced feed system
Oil tank capacity	6 liters

Table 4. Accuracy and uncertainty of the measurements.

Measurements	Accuracy	Uncertainty (%)
Temperatures	±1 ˚C	-
Engine speed	± rpm	-
Time	±0.5%	-
Power	±1%	1.5
SFC	±2%	1.4
CA encoder	±0.5˚ CA	1.5
CO	±0.02%	±1
HC	±10 ppm	±1
CO_2	±0.5%	±2
NO_x	±15 ppm	±2

RESULTS AND DISCUSSION

Experimental analysis of CO, HC, NO_x, and smoke opacity was conducted, along with the performance characteristics of BTE and brake specific energy consumption (BSEC), for both BFME blends and diesel. For combustion analysis, the CP and HRR were evaluated.

Performance Characteristics

Various blends of *B. flabellifer* and diesel at varying peak CP are shown in Figure 4(a), along with the corresponding BTE in relation to brake power (BP). The graph shows that the raw *B. flabellifer* biodiesel has a lower BTE than diesel because of its higher viscosity and lower heat content. When compared to diesel, BFMEs have a higher viscosity and a lower heating value, leading to a lower BTE of 10.9% at full load. Therefore, *B. flabellifer* fuel was combined with diesel at varying concentrations (BFME20, BFME40, BFME60, BFME80, and BFME), increasing its viscosity and calorific value. When the diesel concentration in biofuel is raised, the viscosity gradually decreases, and the heating value steadily improves in comparison to BFME. Compared to BFMEs at full load conditions, BFME20, BFME40, BFME60, and BFME80 each showed a 5.1%, 2.8%, 2.0%, and 1.4% increase in BTE, respectively. Higher oxygen concentration, together with improved viscosity and heating value, could contribute to these findings regarding the complete combustion of *B. flabellifer* blends. These results align with those of a previous study [29]. According to the results, BFME20 and

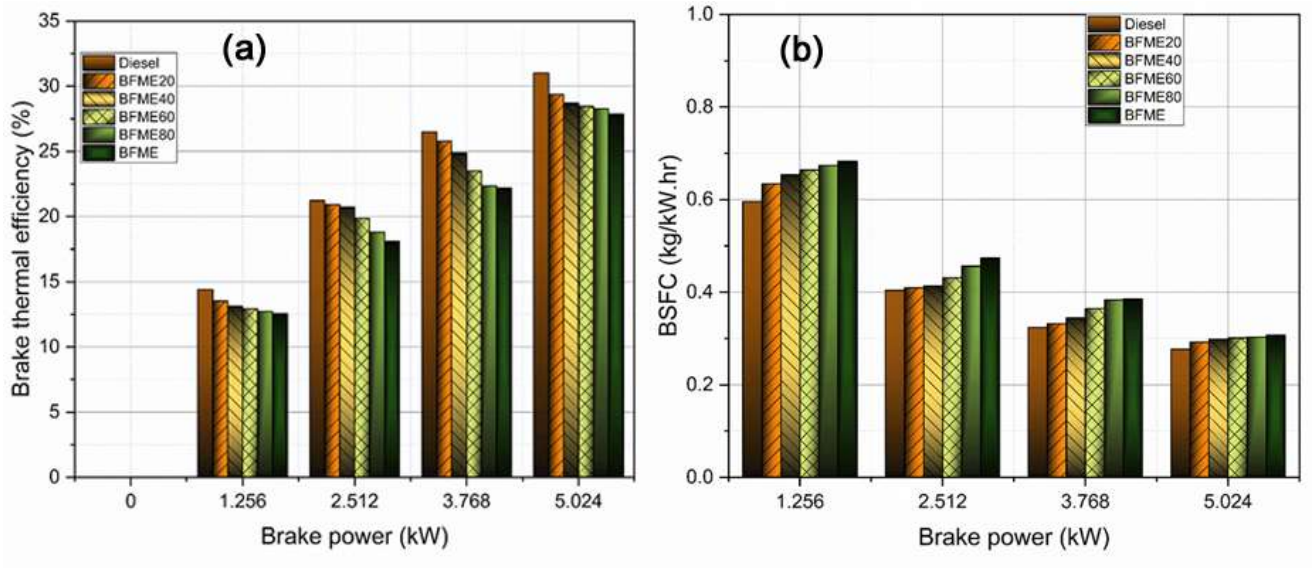

Fig. 4. Variation of engine parameters at different BPs for various blends: (a) brake thermal efficiency and (b) brake specific fuel consumption.

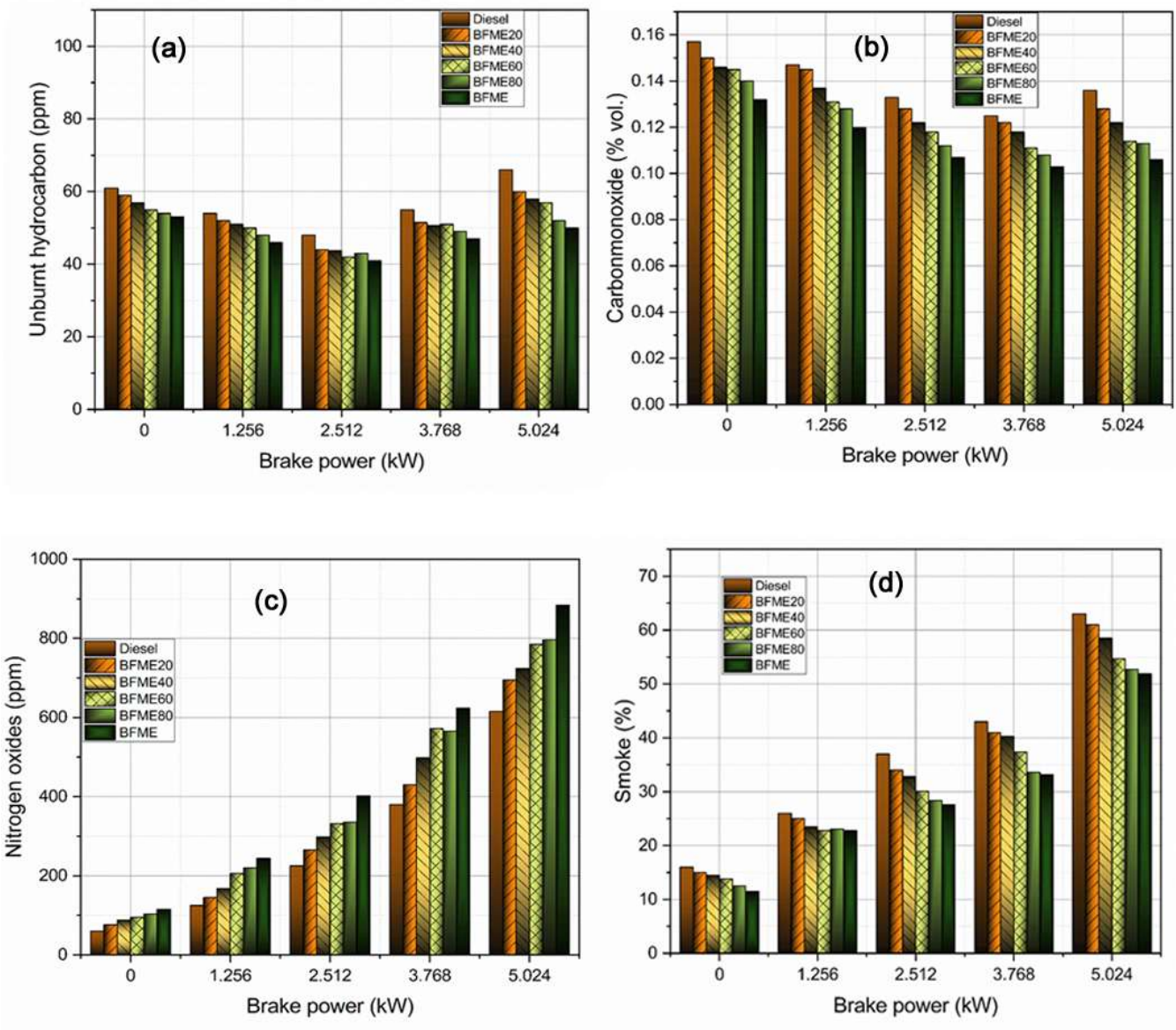

Fig. 5. Variation of engine parameters at different BPs for various blends: (a) HC, (b) CO, (c) NO_x, and (d) smoke.

BFME40 are superior to other blends in terms of performance. Owing to concerns regarding diesel substitution, further research was conducted on BFME20. All things considered, BFME20 was found to be the best blend, so it can be used for future experiments.

Variation in BSFC relative to BP at a steady state for various blends of *Borassus* biodiesel and diesel is shown in Figure 4(b). Use of raw *Borassus* biodiesel, as seen in the graph, increases fuel usage. Compared to diesel, BFMEs have a lower heating value. It is also clear from the results of BTE, which are a reflection of the amount of energy used. As a result of its high viscosity and low calorific value, BFMEs may not be atomized or evaporated efficiently, leading to this effect. From B100, *Borassus* biodiesel shows a gradual BSFC enhancement when the diesel concentration is increased. Improved BSFC values were measured for BFME20 (0.291 kg/kWh), BFME40 (0.298 kg/kWh), BFME60 (0.304 kg/kWh), and BFME80 (0.303 kg/kWh) at full load. Enhanced combustion in lower BFME blends is responsible for the reduced fuel required for the engine. It has been shown that fuel efficiency improves when the heating value of the fuel is increased. According to researchers, these explanations are reliable [30]. Because of a lack of calorific value, the BSFC of diesel blends with lower concentrations of BFMEs was better than those with greater concentrations of BFMEs. Overall, it was found that the BFME20 blend performed similarly to diesel fuel.

Emission Characteristics

The impact of HC formation on *B.* biodiesel-diesel blends and diesel fuel is shown in Figure 5(a). Compared to diesel fuel, the graph demonstrates significantly lower HC emissions for BFMEs. This could be because of the low levels of hydrogen and carbon present, in addition to the abundance of oxygen. HC emission for BFMEs is recorded at 50 ppm, which is 24.2% lower than diesel fuel. As a result of the beneficial effect of the integrated O_2, the CO emission profile was also observed in the HC emission. For all the test fuels, HC emission formation tended to rise with increasing engine load because a greater proportion of A/F mixture was admitted to the combustion zone under higher loads. Maximum engine load causes increased HC emissions from all test fuels because of the shorter combustion time required to maintain a constant engine speed. Diesel, BFME20, BFME40, BFME60, BFME80, and BFME all had HC emission results of 66, 58, 52, and 50 ppm at a peak load, respectively. Because of the enhanced combustion and increased oxygen content in biodiesel blends, HC emissions are reduced. As the concentration of *Borassus* in diesel is lowered from BFME80 to BFME20, the HC emission increases steadily due to the absence of O_2 content in lower blends. Although BFME80 had lower HC emissions than BFME20, the BFME20 blend was the best option due to its higher combustion efficiency and lower emission rate.

The CO emission variance for various BP, including *Borassus* biodiesel-diesel blends, and diesel fuel under standard conditions, is depicted in Figure 5(b). Based on the analysis recorded in the graph, raw *Borassus* biodiesel has a lower CO content than diesel. There is a significant concentration of internal O_2 in BFMEs, which may justify this production. In comparison to diesel, the generation of CO emissions is reduced by 21.9% for BFMEs at full load. *Borassus*'s ability to convert CO_2 to CO more efficiently is evidenced by the presence of built-in O_2 atoms. *Borassus*'s abundant supply of oxygen molecules also speeds up the combustion process, resulting in more efficient burning and fewer emissions. Comparable results are available [31]. As the *Borassus* concentration in diesel was lowered from BFME80 to BFME20, the CO emission rose progressively due to the decreasing O_2 level in the blend. Engine running on BFME20, BFME40, BFME60, BFME80, and BFME had CO emissions of 0.128%, 0.122%, 0.114%, 0.113%, and 0.106% vol., respectively. Compared to diesel, the CO emission was reduced by 17.1% for BFME20, 13.1% for BFME40, 7% for BFME60, and 6.1% for BFME80. The graph shows that the CO emission decreases for all the considered fuels as the load percentage rises from 20% to 70%. In contrast, at peak load situations, CO generation increased dramatically for all test fuels due to shorter residential combustion times and higher fuel consumption to maintain a steady-state condition [32]. Overall, the *Borassus* fuel blend had less carbon monoxide than diesel, and the BFME20 was chosen as the best blend because of its improved combustion and reduced emission formation.

Results of NO_x emission testing under varying loads for *Borassus* biodiesel-diesel blends and diesel fuel are shown in Figure 5(c). Because the presence of O_2 in it caused the cylinder temperature to increase, the NO_x emission for all Borassus blends was higher than diesel. In all, the engine's NO_x emissions were 695, 724, 785, and 796 ppm when it was run on blends of BFME20, BFME40, BFME60, and BFME80. Compared to BFME, the NO_x levels dropped by 22.0% for BFME40, 12.6% for BFME60, and 11.05% for BFME80. Also, compared to diesel, NO_x emissions from CI engines running on BFME20, BFME40, BFME60, BFME80, and BFME were 13%, 17%, 27%, 29%, and 43% higher, respectively. Complete combustion caused by the presence of O_2 in *Borassus* biodiesel likely accounts for the higher peak combustion temperature observed. The greater combustion temperature of *Borassus* biodiesel may potentially contribute to these results. The graph demonstrates that NO_x emissions rise sharply with increasing load and *Borassus* biodiesel content. Reasons for this improvement in in-cylinder temperature may include a rise in the concentration of *Borassus* fuel, which increased the availability of heat in combustion from the previous cycle, and the presence of more O_2 molecules [33]. In addition, the peak in the cylinder temperature caused by the biodiesel's greater ignition delay resulted in higher NO_x emissions.

Smoke emissions from diesel and various Borassus biodiesel blends are presented in Figure 5(d). The graph shows that when *Borassus* fuel is blended with diesel, smoke emissions decrease. In the case of BFME, the resultant smoke emission is approximately 48.9% at maximum load. Incomplete combustion due to a rich or low mixture is typically responsible for the release of smoke during combustion. Owing to the abundance of oxygen

molecules, which improve combustion, the issue was addressed. It has been found that increasing the *Borassus* concentration in diesel fuel exerts a negative effect on smoke emissions. When operating on BFME20, BFME40, BFME60 and BFME80, the engine's smoke emissions were 61.7%, 58.5%, 54.8%, and 52.7%, respectively. Smoke levels rose by 16.4% for BFME40, 10.2% for BFME60, and 7.2% for BFME80 compared to BFME. Smoke emissions from CI engines operating on BFME20, BFME40, BFME60, BFME80, and BFME were 3%, 1%, 13%, 16%, and 22% lower, respectively, compared to diesel. When the A/F ratio allowed into the combustion zone, or the amount of charge mixture present in the crevice volume, increases with engine load, smoke pollution generation also increases for all test fuels. Lower smoke emission was observed for blend concentrations of *Borassus* with diesel up to 80%, after which smoke emission marginally increased due to the larger droplet size of BFME resulting from higher viscosity. Owing to the presence of oxygen in biodiesel, which may have improved combustion, the biodiesel blends produce less smoke than diesel [34].

During the maximum load condition of a diesel engine, the HRR varies in relation to the CA, as shown in Figure 6(b). This study examined the effectiveness of HRR using various diesel and *Borassus* fuel blends. In the graph, diesel fuel was observed to have a greater HRR than the other fuels used in the experiment. The increased energy content and reduced viciousness of diesel fuel may be responsible for these outcomes. This is because the BFME blend has a lower heat content and a higher viscosity than other blends, hence the HRR is lower. HRR values of 67.9, 66.9, 62.8, 62.5, and 57.5 J/CA were achieved by the engine operating on BFME20, BFME40, BFME60, and BFME80, respectively. There was a 2.3% decrease in HRR generation for BFME20, 3.8% for BFME40, 9.7% for BFME60, and 10.2% for BFME80 compared to diesel. It may be because *Borassus* and its blends have a higher viscosity than diesel, which slows the rate at which they vaporize. Compared to diesel, *Borassus* blends with a higher cetane number begin their peak HRR curve and dominate the diffusion combustion phase much earlier. The results showed that when the *Borassus* concentration was diluted, the HRR output increased. The oxygen molecules in the fuel are the most important players during the combustion process, especially during the diffusion stage [34]. It's possible that the increased combustion and the existing O_2 content together produced these results.

CONCLUSION

In this study, the physical and chemical properties of *Borassus* biodiesel were evaluated. It could be used as a renewable fuel in a conventional internal combustion engine. The performance began to decrease with pure *Borassus* biodiesel, and it was closest to diesel with the BFME20 and BFME40 blends. Compared to other blends, BFME20 and BFME40 had lower energy consumption and higher thermal efficiency. In addition, compared to pure *Borassus* biodiesel, BFME20 was shown to reduce fuel consumption by 5.2% and to increase thermal efficiency by a respectable amount. Compared to diesel, HC and CO emissions from the BFME20 blend were lower. To compare, the reductions in BFME20 caused by HC, CO, and smoke were 9.9%, 5.8% and 3.1%, respectively. In the presence of sufficient oxygen and at the peak of the cycle's heat, *Borassus* blends significantly raise NO_x generation. Moreover, BFME20 had a slightly greater BTE than the other biodiesel blends. According to the parameters for higher diesel replacement and lower emissions, BFME20 was determined to be the best alternative energy source for the CI engine. As a result, it is necessary to improve its performance qualities and minimize harmful exhaust emissions before considering it as a replacement energy source.

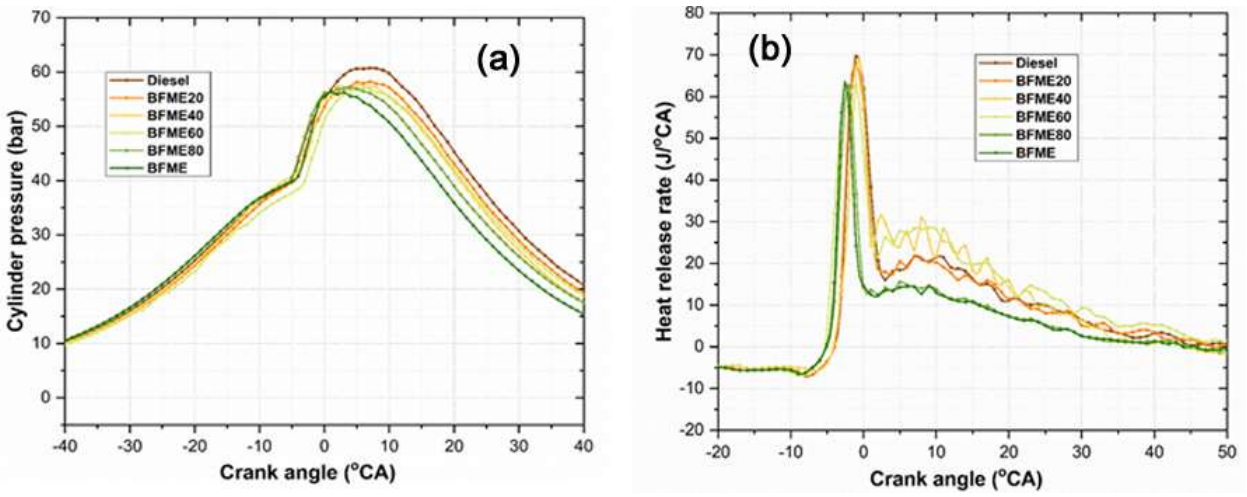

Fig. 6. Comparison of combustion characteristics for various blends of biodiesel: (a) cylinder pressure and (b) heat release rate.

NOMENCLATURE

bTDC - Before top dead center
BFME - Neat *B. flabellifer* methyl esters 100%
BFME 20 - 20% *B. flabellifer* methyl esters +80% diesel
BFME 40 - 40% *B. flabellifer* methyl esters +60% diesel
BFME 60 - 60% *B. flabellifer* methyl esters +40% diesel
BFME 80 - 80% *B. flabellifer* methyl esters +20% diesel
BP - Brake power
BSEC - Brake specific energy consumption
BSFC - Brake specific fuel consumption
BTE - Brake thermal efficiency
CA - Crank angle
CI - Compression ignition
CNG - Compressed natural gas
CP - Cylinder pressure
CRDI - Common rail direct injection
FTIR - Fourier transform infrared spectroscopy
HC – Hydrocarbon
HRR - Heat release rate
HRRmax - Maximum net heat release rate
KOME - Kapok oil methyl ester
UBHC - Unburned hydrocarbon

REFERENCES

[1] S. Ellappan, S. Rajendaran, Energy Sources, Part A 46 (2024) 4810-4824. https://doi.org/10.1080/15567036.2019.1704315.
[2] K. Selvaraj, M. Thangavel, Energy Sources, Part A 43 (2021) 145-159. https://doi.org/10.1080/15567036.2019.1623950.
[3] C. Sakthi Rajan, K. Muralidharan, J. Therm. Anal. Calorim. 147 (2022) 8901-8917. https://doi.org/10.1007/s10973-021-11127-0.
[4] A.S. Ramadhas, S. Jayaraj, C. Muraleedharan, Fuel 84 (2005) 335-340. https://doi.org/10.1016/j.fuel.2004.09.016.
[5] D. Agarwal, L. Kumar, A.K. Agarwal, Renewable Energy 33 (2008) 1147-1156. https://doi.org/10.1016/j.renene.2007.06.017.
[6] P.K. Devan, N.V. Mahalakshmi, Fuel 88 (2009) 861-867. https://doi.org/10.1016/j.fuel.2008.11.005.
[7] K. Muralidharan, D. Vasudevan, K.N. Sheeba, Energy 36 (2011) 5385-5393. https://doi.org/10.1016/j.energy.2011.06.050.
[8] A.K. Agarwal, A. Dhar, Renewable Energy 52 (2013) 283-291. https://doi.org/10.1016/j.renene.2012.10.015.
[9] R. Mohsin, Z.A. Majid, A.H. Shihnan, N.S. Nasri, Z. Sharer, Energy Convers. Manage. 88 (2014) 821-828. https://doi.org/10.1016/j.enconman.2014.09.027.
[10] B.N. Agrawal, S. Sinha, A.V. Kuzmin, V.A. Pinchuk, Therm. Sci. Eng. Prog. 14 (2019) 100404. https://doi.org/10.1016/j.tsep.2019.100404.
[11] N.H. Papu, P. Lingfa, S.K. Dash, Energy Sources, Part A 46 (2024) 12620-12632. https://doi.org/10.1080/15567036.2020.1798566.
[12] A.V.S.L. Sai Bharadwaj, N. Subramaniapillai, M.S.B. Khadhar Mohamed, A. Narayanan, Fuel 296 (2021) 120708. https://doi.org/10.1016/j.fuel.2021.120708.
[13] S. Yadav, A. Kumar, A. Chaudhary, Sci. J. Sil. Univ. Technol., Ser. Transp. 115 (2022) 249-264. https://doi.org/10.20858/sjsutst.2022.115.17.
[14] R. Rohith Renish, G. Maneesha, P. Jeyaraman, T. Niruban Projoth, Mater. Today: Proc. 62 (2022) 3689-3698. https://doi.org/10.1016/j.matpr.2022.04.427.
[15] C. Sakthi Rajan, A. Baluchamy, J. Venkatesh, S. Balamurugan, R. Karthick, Eng. Proc. 61 (2024) 7. https://doi.org/10.3390/engproc2024061007.
[16] A. Baluchamy, R. Karthick, C. Sakthi Rajan, T. Rajkumar, Multidiscip. Sci. J. 6 (2023) 2024071. https://doi.org/10.31893/multiscience.2024071.
[17] A. Kumar Paswan, S. Kesharvani, K. Gidwani Suneja, G. Dwivedi, Mater. Today: Proc. 78 (2023) 647-655. https://doi.org/10.1016/j.matpr.2022.12.069.
[18] M.M. Uyar, A.B. Demirpolat, H. Arslanoglu, Colloid Polym. Sci. 301 (2023) 557-567. http://doi.org/10.1007/s00396-023-05085-2.
[19] A.B. Demirpolat, M.M. Uyar, H. Arslanoglu, Pet. Chem. 62 (2022) 433-443. https://doi.org/10.1134/S0965544122020190.
[20] M.M. Uyar, A. Çıtlak, A.B. Demirpolat, Ind. Crops Prod. 222 (2024) 119712. https://doi.org/10.1016/j.indcrop.2024.119712.
[21] A. Baluchamy, C. Sakthi Rajan, S. Balamurugan, J. Venkatesh, 26 (2024) 1-10. https://doi.org/10.30955/gnj.005777.
[22] C. Sakthi Rajan, K. Muralidharan, B. Anbarasan, A. Ramesh Kumar, Energy Sources A: Recovery Util. Environ. Eff. 46 (2024) 7310-7322. https://doi.org/10.1080/15567036.2024.2355363.
[23] M. Chhabra, A. Sharma, G. Dwivedi, Egypt. J. Petrol. 26 (2017), 511-518. https://doi.org/10.1016/j.ejpe.2016.07.002.
[24] L.A. Raman, B. Deepanraj, S. Rajakumar, V. Sivasubramanian, Fuel. 246 (2019) 69-74. https://doi.org/10.1016/j.fuel.2019.02.106.
[25] M.A. Asokan, S. Senthur Prabu, P.K.K. Bade, V.M. Nekkanti, S.S.G. Gutta, Energy. 173 (2019) 883-892. https://doi.org/10.1016/j.energy.2019.02.075.
[26] M.E.S. Mirghani, N.A. Kabbashi, M.Z. Alam, I.Y. Qudsieh, M.F.R. Alkatib, J. Am. Oil Chem. Soc. 88 (2011) 1897-1904. https://doi.org/10.1007/s11746-011-1866-0.
[27] K.R. Bukkarapu, A. Krishnasamy, Energy Fuel. 35 (2021) 7993-8005. https://doi.org/10.1021/acs.energyfuels.0c03927.
[28] M. Tariq, S. Ali, F. Ahmad, M. Ahmad, M. Zafar, N. Khalid, M.A. Khan, Fuel Process. Technol. 92 (2011) 336-341. https://doi.org/10.1016/j.fuproc.2010.09.025.
[29] A.S. Mohammed, S.M. Atnaw, A.V. Ramaya, G. Alemayehu, J. Energy Inst. 108 (2023) 101227. https://doi.org/10.1016/j.joei.2023.101227.
[30] S. Vijayan, R. Sathyamurthy, E.M.A. Mokheimer, R.S. Kumar, Fuel Process. Technol. 248 (2023)

107842. https://doi.org/10.1016/j.fuproc.2023.107842.
[31] J. Wang, H. Sun, S. Devanesan, M.S. Alsahi, A. Anderson, F. Daniel, T.R. Praveenkumar, Fuel 352 (2023) 128946. https://doi.org/10.1016/j.fuel.2023.128946.
[32] P.K. Wong, S.H. Chen, M.A. Ghadikolaei, K.W. Ng, S.M. Yuen Lee, J.C. Xu, Z.D. Lian, M. Ren, Z. Ning, N.K. Gali, Environ. Pollut. (Oxford, U.K.) 333 (2023) 122099. https://doi.org/10.1016/j.envpol.2023.122099.
[33] P. Karin, A. Tripatara, P. Wai, B.-S. Oh, C. Charoenphonphanich, N. Chollacoop, H. Kosaka, Case Stud. Chem. Environ. Eng. 6 (2022) 100249. https://doi.org/10.1016/j.cscee.2022.100249.
[34] P. Anchupogu, R.L. Krupakaran, S. Venkateswarlu, S. Satish, S. Phaneendrareddy, S. Shohel, P. Umamaheswarrao, Mater. Today: Proc. 102 (2024) 236-240. https://doi.org/10.1016/j.matpr.2023.05.089.
[35] S. Kumar, R. Gautam, Sustain. Energy Technol. Assess. 57 (2023) 103305. https://doi.org/10.1016/j.seta.2023.103305.

SAKTHI RAJAN CHANDRAMURTHY[1]
SILAMBARASAN RAGUNATHAN[2]
RAMESH KUMAR AYYAKKANNU[3]
ANBARASAN BALUCHAMY[4]

[1]SBM College of Engineering & Technology, Dindigul, Tamil Nadu, India
[2]Annamalai Polytechnic College, Chettinad, Tamil Nadu, India
[3]Sona College of Technology, Salem, Tamil Nadu, India
[4]PSNA College of Engineering & Technology, Dindigul, Tamil Nadu, India.

NAUČNI RAD

KARAKTERISTIKE SAGREVANJA, PERFORMANSI I EMISIJE MOTORA SA KOMPRESIONIM PALJENJEM PRI KORIŠĆENJU MEŠAVINA BIODIZELA OD ULJA *BORASSUS FLABELLIFER*

Metil estri Borassus flabellifer (BFME) imaju nekoliko atraktivnih karakteristika koje ih čine potencijalnim rivalom dizelu i drugim alternativnim gorivima. Ovaj rad predstavlja prvu sveobuhvatnu analizu njegovih performansi, sagorevanja i emisija u dizel motoru. Pored visoke kalorijske vrednosti, visokog cetanskog broja i dostupnosti kiseonika, koji čini 10% njegove ukupne mase, takođe je lako dostupan. Eksperimentalno testiranje BFME je sprovedeno na jednocilindričnom motoru sa kompresionim paljenjem (CI) u ovoj fazi. BFME su mešani sa dizelom u različitim koncentracijama (20%, 40%, 60%, 80% i 100%). Mešavine BFME su eksperimentalno ispitane na njihova svojstva sagorevanja, emisije i performanse. CI motor je podešen na rad u stacionarnom stanju kako bi dostigao optimalnu temperaturu za uslove u kojima je radio. U početku je utvrđeno da čisti BFME imaju najnižu termičku efikasnost, dok su BFME20, BFME40, BFME60 i BFME80 imali veću termičku efikasnost kočenja (BTE) od BFME100 pri nominalnim uslovima opterećenja (za 5,1%, 2,8%, 2,0% i 1,4%, redom). U poređenju sa drugim mešavinama, BFME20 i BFME40 imaju bolju efikasnost goriva. Efikasnost goriva je značajno poboljšana, a potrošnja BFME20 je smanjena za 5,1% u poređenju sa BFME100. U poređenju sa dizelom, emisije ugljovodonika, CO i dima iz BFME20 su smanjene za 9,9%, 5,8% i 3,71%, redom. Ovi rezultati naglašavaju potencijal BFME mešavina sa niskim odnosom kao čistijih i efikasnijih alternativa biodizelu, ističući praktičnu primenljivost BFME u postojećim dizel motorima bez većih modifikacija.

Ključne reči: Biodizel, Borassus flabellifer, sagorevanje, performanse i karakteristike emisije.